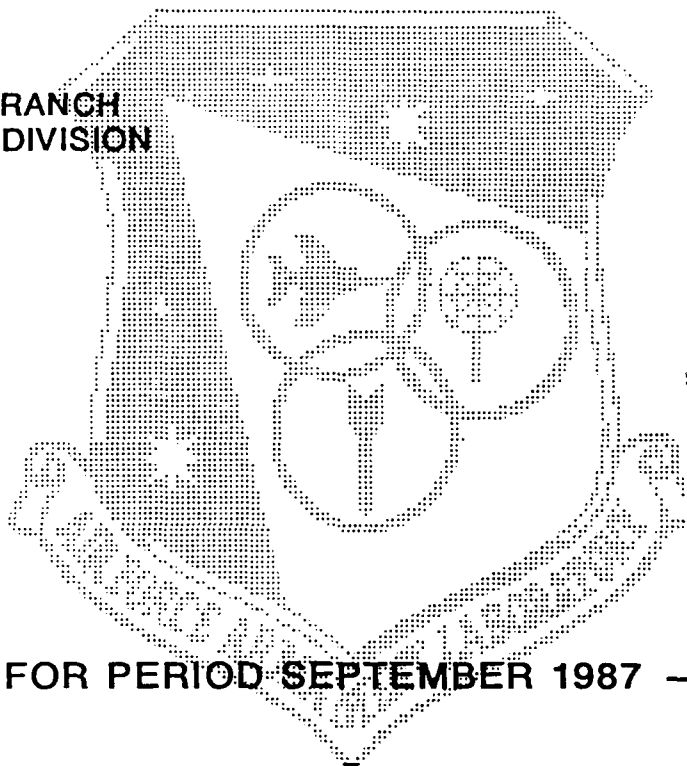


Three-Dimensional Solution-Adaptive Grid Generation on Composite Configurations

Yen Tu

AREODYNAMICS BRANCH
AEROMECHANICS DIVISION

APRIL 1990



DTIC
ELECTE
APR 26 1990
S B D

FINAL REPORT FOR PERIOD SEPTEMBER 1987 - MAY 1989

APPROVED FOR PUBLIC RELEASE; DISTRIBUTION UNLIMITED

AIR FORCE ARMAMENT LABORATORY

Air Force Systems Command ■ United States Air Force ■ Eglin Air Force Base, Florida

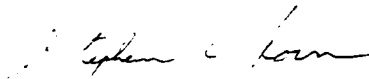
NOTICE

When Government drawings, specifications, or other data are used for any purpose other than in connection with a definitely related Government procurement operation, the United States Government thereby incurs no responsibility nor any obligation whatsoever; and the fact that the Government may have formulated, furnished, or in any way supplied the said drawings, specifications, or other data, is not to be regarded by implication or otherwise as in any manner licensing the holder or any other person or corporation, or conveying any rights or permission to manufacture, use, or sell any patented invention that may in any way be related thereto.

This report has been reviewed by the Public Affairs Office (PA) and is releasable to the National Technical Information Service (NTIS). At NTIS, it will be available to the general public, including foreign nations.

This technical report has been reviewed and is approved for publication.

FOR THE COMMANDER



STEPHEN C. KORN
Acting Chief, Aeromechanics Division

If your address has changed, if you wish to be removed from our mailing list, or if the addressee is no longer employed by your organization, please notify AFATL/FXA, Eglin AFB FL 32542-5434.

Copies of this report should not be returned unless return is required by security considerations, contractual obligations, or notice on a specific document.

REPORT DOCUMENTATION PAGE			Form Approved OMB No. 0704-0188	
Public reporting burden for this collection of information is estimated to average 1 hour per response, including the time for reviewing instructions, searching existing data sources, gathering and maintaining the data needed, and completing and reviewing the collection of information. Send comments regarding this burden estimate or any other aspect of this collection of information, including suggestions for reducing this burden, to Washington Headquarters Services, Directorate for Information Operations and Reports, 1215 Jefferson Davis Highway, Suite 1204, Arlington, VA 22202-4302, and to the Office of Management and Budget, Paperwork Reduction Project (0704-0188), Washington, DC 20503.				
1. AGENCY USE ONLY (Leave blank)	2. REPORT DATE April 1990	3. REPORT TYPE AND DATES COVERED Final September 1987 to May 1989		
4. TITLE AND SUBTITLE Three-Dimensional Solution-Adaptive Grid Generation on Composite Configuration		5. FUNDING NUMBERS 61102F-25670308		
6. AUTHOR(S) Yen Tu				
7. PERFORMING ORGANIZATION NAME(S) AND ADDRESS(ES) Aerodynamics Branch (FXA) Aeromechanics Division Air Force Armament Laboratory Eglin AFB, FL 32542-5434		8. PERFORMING ORGANIZATION REPORT NUMBER		
9. SPONSORING/MONITORING AGENCY NAME(S) AND ADDRESS(ES) Aeromechanics Division Air Force Armament Laboratory Eglin AFB, FL 32542-5434		10. SPONSORING/MONITORING AGENCY REPORT NUMBER AFATL-TR-90-17		
11. SUPPLEMENTARY NOTES This report was a thesis; therefore the AFATL format was not used. Availability of this report is specified on verso of front cover.				
12a. DISTRIBUTION/AVAILABILITY STATEMENT Approved for public release; distribution unlimited		12b. DISTRIBUTION CODE		
13. ABSTRACT (Maximum 200 words) A solution-adaptive grid generation procedure is developed and applied to three-dimensional inviscid transonic fluid flow around complex geometries using a composite block grid structure. The adaption is based upon control functions in an elliptic grid generation system. The control function is constructed in a manner such that a proper grid network can be generated as a fluid flow solution is evolving. The grid network is boundary-conforming for accurate representation of boundary conditions. The procedure implemented allows orthogonality at boundaries for more accurate computations, while smoothness is implicit in the elliptic equations. The approach allows multiple-block grid systems to be constructed to treat complex configurations as well. The solution-adaptive computational procedure has been accomplished by coupling the elliptic grid generation technique with an implicit, finite volume, upwind Euler flow solver. In simulating transonic fluid flow around a finned body of revolution and a multiple store configuration, the grid systems adapt to pressure gradients in the flow field. Results obtained show that the technique is capable of generating grid networks proper for the simulations of aerodynamics around complex configurations.)				
14. SUBJECT TERMS Grid Generation Computational Fluid Dynamics Euler Equations		15. NUMBER OF PAGES 112		
		16. PRICE CODE		
17. SECURITY CLASSIFICATION OF REPORT UNCLASSIFIED	18. SECURITY CLASSIFICATION OF THIS PAGE UNCLASSIFIED	19. SECURITY CLASSIFICATION OF ABSTRACT UNCLASSIFIED	20. LIMITATION OF ABSTRACT SAR	

PREFACE

This report describes an in-house effort performed by Yen Tu of Aerodynamics Branch (FXA), Aeromechanics Division (FX), Air Force Armament Laboratory (AFATL), Eglin Air Force Base, Florida. The work reported covers the time period of September 1987 to May 1989.

ACKNOWLEDGMENTS

I would like to express my appreciation to Dr Joe F. Thompson of Mississippi State University (MSU), my major advisor, for his guidance and Dr David Whitfield for his helpful discussions during the course of this research effort. The support I received from the Air Force Armament Laboratory has been indispensable and invaluable.



Accession For	
NTIS GRA&I	<input checked="checked" type="checkbox"/>
DTIC TAB	<input type="checkbox"/>
Unannounced	<input type="checkbox"/>
Justification	
By	
Distribution/	
Availability Codes	
Dist	Avail and/or Special
A-1	

TABLE OF CONTENTS

ACKNOWLEDGEMENTS.	ii
ABSTRACT.	iii
TABLE OF CONTENTS	v
NOMENCLATURE.	vi
LIST OF FIGURES	vii
CHAPTERS	
I. INTRODUCTION	1
II. SOLUTION-ADAPTIVE GRID GENERATION.	5
II.1 Elliptic Grid Generation	6
II.2 Truncation Error	8
II.3 Control Function Approach.	10
II.4 EAGLE Grid Code.	15
II.5 EAGLE Flow Code.	16
III. RESULTS AND DISCUSSION	18
III.1 Finned Body of Revolution	18
III.2 Multiple Store Configuration.	24
IV. CONCLUSTIONS AND RECOMMENDATIONS	27
REFERENCES.	101

NOMENCLATURE

Symbols

c	Constant
W	Weight Function
P	Control Function
\underline{r}	Position Vector
g^{ij}	Contravariant Metric Coefficients
∇	Gradient
∇^2	Laplacian
x, y, z	Cartesian Coordinates
ξ, η, ζ	Curvilinear Coordinates

Subscript

$()_{x,y,z}$	Partial Derivative with respect to x, y, z
$()_{\xi,\eta,\zeta}$	Partial Derivative with respect to ξ, η, ζ

Superscript

$()^i$	i th component or sequential index
---------	--------------------------------------

LIST OF FIGURES

FIGURE	Page
1. Physical and Computational Domain.	29
2. Overall View of Grid System.	30
3. Initial Grid of Finned Body of Revolution.	31
4. Initial Grid - Nose Section.	32
5. Initial Grid - Tail Section.	33
6. Pressure Contours with Initial Grid.	34
7. Mach Contours with Initial Grid.	35
8. Fifth Adaptive Grid with Equation (II-20)	36
9. First Adaptive Grid.	37
10. Second Adaptive Grid	38
11. Third Adaptive Grid.	39
12. Fourth Adaptive Grid	40
13. Fifth Adaptive Grid.	41
14. Adaptive Grid at Nose Section with Five Adaptations.	42
15. Adaptive Grid at the Shock - Nose Section.	43
16. Adaptive Grid at Tail Section with Five Adaptations.	44
17. Pressure Contours with Five Adaptations.	45
18. Shock with Initial Grid - Pressure Contour	46
19. Shock with Five Adaptations - Pressure Contour	47
20. Pressure Contour on the Nose Surface with Initial Grid	48
21. Pressure Contour on the Nose Surface with Five Adaptations	49
22. Mach Contours with Five Adaptations.	50
23. Shock with Initial Grid - Mach Contour	51
24. Shock with Five Adaptations - Mach Contour	52

25. Pressure Distribution Along Body, $\Phi = 0$ Deg.	53
26. Pressure Distribution Along Body, $\Phi = -30$ Deg.	54
27. Pressure Distribution Along Body, $\Phi = -60$ Deg.	55
28. Pressure Distribution Along Body, $\Phi = 180$ Deg.	56
29. Pressure Distribution Along Body, $\Phi = 150$ Deg.	57
30. Pressure Distribution Along Body, $\Phi = 120$ Deg.	58
31. Pressure Distribution Along Fin, $\Phi = +45$ Deg., Row = 1 . .	59
32. Pressure Distribution Along Fin, $\Phi = +45$ Deg., Row = 2 . .	60
33. Pressure Distribution Along Fin, $\Phi = -45$ Deg., Row = 3 . .	61
34. Pressure Distribution Along Fin, $\Phi = -45$ Deg., Row = 4 . .	62
35. Pressure Distribution Along Fin, $\Phi = -135$ Deg., Row = 1. .	63
36. Pressure Distribution Along Fin, $\Phi = -135$ Deg., Row = 2. .	64
37. Pressure Distribution Along Fin, $\Phi = +135$ Deg., Row = 3. .	65
38. Pressure Distribution Along Fin, $\Phi = +135$ Deg., Row = 4. .	66
39. Residual Convergence Histories, Blocks One thru Four	67
40. Residual Convergence Histories, Blocks Five thru Eight . . .	68
41. Perspective View of the Structure of Thirty Blocks	69
42. Perspective View of Thirty-Block Grid System	70
43. Cross Sectional View of the Structure of Thirty Blocks . . .	71
44. Multiple Store Configuration	72
45. Frontal View of Multiple Store Configuration	73
46. Cross Sectional View of Multiple Store Configuration	74
47. Initial Grid, Section A-A.	75
48. Pressure Contours with Initial Grid, Section A-A	76
49. Mach Contours with Initial Grid, Section A-A	77
50. Grid with One Adaptation, Section A-A.	78
51. Grid with Two Adaptations, Section A-A	79

52. Grid with Three Adaptations, Section A-A	80
53. Pressure Contours with Three Adaptations, Section A-A.	91
54. Mach Contour with Three Adaptations, Section A-A	82
55. Pressure Distribution Along Store 1, $\Phi = 0$ Deg	83
56. Pressure Distribution Along Store 1, $\Phi = 220$ Deg	84
57. Initial Grid, Section B-B.	85
58. Pressure Contours with Initial Grid, Section B-B	86
59. Mach Contours with Initial Grid, Section B-B	87
60. Grid with One Adaptation, Section B-B.	88
61. Grid with Two Adaptations, Section B-B	89
62. Grid with Three Adaptations, Section B-B	90
63. Pressure Contours with Three Adaptations, Section B-B.	91
64. Mach Contours with Three Adaptations, Section B-B.	92
65. Initial Grid, Section C-C.	93
66. Grid with Three Adaptations, Section C-C	94
67. Initial Grid, Section D-D.	95
68. Grid with Three Adaptations, Section D-D	96
69. Initial Grid, Section E-E.	97
70. Grid with Three Adaptations, Section E-E	98
71. Initial Grid, Section F-F.	99
72. Grid with Three Adaptations, Section F-F	100

CHAPTER I

INTRODUCTION

The first step in attempting to numerically solve a complex fluid flow problem is to generate a grid system over the domain of interest. Then numerical techniques, such as finite difference, finite volume or finite element methods are applied to solve the governing conservation laws of fluid mechanics over the domain. It has been shown that the characteristics of a grid system used have significant effect on the accuracy and convergency of problem solutions, cf. Refs. [1, 2]. The use of an improper grid system for a problem often results in divergence or renders even a convergent solution useless.

A grid system in a physical domain of interest can be constructed by first establishing coordinate points on all, or a portion of, the boundaries of the domain and then solving for the coordinates of nodal points in the domain interior with appropriate methods; e.g., complex variable methods, algebraic methods or differential methods. These nodal points, along with those on the boundaries, form grid cells. Several characteristics of a grid system are very important as they affect the accuracy and convergency of problem solutions. Clearly, it is easier to construct a rectangular coordinate grid system because it consists simply of straight lines. However, with rectangular coordinate systems, the implementation of boundary conditions on bodies with complex geometry is tedious. Interpolation between grid points or cells near boundaries is necessary. This makes the generalization of the coding of numerical solution algorithms rather difficult. On the other hand, with a curvilinear boundary-conforming grid system, one or more

of the coordinate lines in the physical domain can be made to coincide with the boundaries of the body. When the system is transformed into a computational domain with equal spacing, the computational algorithms for solving the governing conservation laws, after they are transformed onto the curvilinear coordinates, can be implemented without interpolations at boundaries, Refs. [2, 3]. This approach greatly facilitates the effort of coding solution algorithms. In addition, smoothness and orthogonality are two well-known desired characteristics, Refs. [1, 2]. Smoothness, which is equivalent to minimization of the change of spacing of grid cells, and orthogonality, which requires grid lines be perpendicular to each other, both tend to reduce errors in problem solutions. Hence these characteristics should be maintained throughout the grid system as far as is practical. This point will be discussed in Chapter II.

In certain regions of interest, the gradients of certain parameters may be very high. If grid lines in these regions are not adequate; i.e., if the spacings are too large, large truncation errors may result. This is detrimental to both the accuracy and convergency of problem solutions. A uniform refinement of the grid network throughout the entire domain would certainly reduce truncation errors. But often in practical applications, the resources of computer memory and central processing unit (CPU) time are limited and a uniform refinement of the grid system may result in adding grid lines in regions where it is not needed. These constraints render the approach expensive. A more logical and economical alternative is to cluster more grid lines in the regions where high gradients take place and hence where high resolution

is needed. In the case of simple fluid flow problems, the locations of high gradients may be estimated and a proper grid system may be constructed accordingly. However, for more complex fluid flow problems, high gradient regions are not known a priori, and the construction of a proper grid system becomes very difficult. For example, in the area where shocks occur, more grid lines are needed in order to resolve the shock location and the properties across the shock more accurately. But the locations of the shocks are not known until the solution is obtained. The ideal of solution-adaptive grid generation; i.e., generating grid networks based upon certain solution information as the solution evolves, appears very attractive to the issue here, cf. Refs. [4, 5, 6, 7].

Since Dywer, et al. Ref. [8], and Klopler and McRae, Ref. [9], presented their works in the early 1980's, many techniques for generating adaptive grids have appeared. Brackbill, et al. Ref. [6], developed a variational method for constructing an adaptive grid. Thompson and Kim, Refs. [4, 5], implemented both a variational approach based on the Euler equation for function minimization and a control function approach based on equidistribution of weight.

Kim investigated an adaptive grid around an ONERA M6 wing with the control function approach. Promising results were obtained, and the grid clustered to where the shock was located. The flow solver section of Kim's code, however, was constructed such that grid blocks must be arranged in a straight sequential manner; i.e., the front of a second block must be connected to the back of a first block, and the front of a third block must be connected to the back of the second block, and so

on. This severely limits applicability of the code. In the present work, this limitation was removed by coupling a flow solver with an arbitrarily blocking structure, Ref. [10]. Furthermore, in Ref. [4], the construction of control functions for adaptive grid generation was based upon an initial grid and gradients of a parameter of a flow field. A different construction of control functions based upon a current grid and flow gradients was used in this effort. This point will be discussed in Chapter II. A very brief review of elliptic grid generation with control functions, upon which this work is based, and the truncation errors associated with the quality of a grid system is also presented in Chapter II. In addition, a brief description of the EAGLE grid code, Ref. [16] and the EAGLE flow solver, Ref. [10], which were employed in this work to construct the solution-adaptive grid code, is given in Chapter V as well. This control function approach for solution-adaptive grid generation, with the modifications mentioned above, was tested with two complex three-dimensional blocked configurations at transonic region, namely, an eight-block finned body of revolution and a thirty-block multi-store configuration. The results are discussed in Chapter III. Concluding remarks and recommendations are contained in Chapter IV.

CHAPTER II

SOLUTION-ADAPTIVE GRID GENERATION

Numerical simulation of an aerodynamic problem typically consists of generating a grid network on the physical domain of interest and then applying a partial differential equation (PDE) flow solver over the grid to obtain solutions. Furthermore, a curvilinear grid system with some coordinate constant on each segment of the physical boundary curve or surface is usually preferred for more accurate representation of boundary conditions, Ref. [1]. This boundary-conforming grid can be generated by first specifying values on the boundaries and then determining the coordinates in the domain interior from the boundaries. Often the application of a PDE flow solver is performed in a transformed computational domain where uniform rectangular blocks are formed. For simplicity, unit increments are usually used in each direction of the computational domain. The equivalent problem in grid generation is then to determine the Cartesian coordinates (or other type coordinates) in the interior of the computational domain from specified values and/or slopes on the boundaries of the domain. This is illustrated for a two-dimensional case in Figure 1.

The determination of interior coordinates in a region can be accomplished by either of the following approaches. First, the interior coordinates can be obtained by simply interpolating values from boundaries which have been specified. The grid generated in this manner is generally referred to as an algebraic grid. On the other hand, the problem can be treated as a boundary-value problem. Hence the solution of a system of partial differential equations can be used to determine

the coordinates of interior points, Ref. [11]. If an elliptic partial differential system is used, all the values at boundaries of a domain must be specified. If a parabolic or a hyperbolic system is used, only a portion of the boundary points needs to be specified. In this study, only elliptic grid generation systems are considered.

II.1 Elliptic Grid Generation

From Refs. [12,13], if a curvilinear coordinate system, $\bar{\xi}^i$ ($i=1,2,3$), which satisfies the Laplace system $\nabla^2 \bar{\xi}^i = 0$, ($i=1,2,3$) is transformed to another coordinate system ξ^i , ($i=1,2,3$), then the new curvilinear coordinates ξ^i satisfy the inhomogeneous elliptic system

$$\nabla^2 \xi^i = p^i \quad (i = 1,2,3) \quad (\text{II-1})$$

where

$$p^i = \sum_{j=1}^3 \sum_{k=1}^3 g^{jk} p_{jk}^i \quad (\text{II-2})$$

and $g^{jk} = \nabla \xi^j \cdot \nabla \xi^k$ is the contravariant metric tensor (II-3)

Here

$$p_{jk}^i = \sum_{m=1}^3 \sum_{n=1}^3 \frac{\partial \bar{\xi}^m}{\partial \xi^j} \frac{\partial \bar{\xi}^n}{\partial \xi^k} \frac{\partial^2 \bar{\xi}^i}{\partial \bar{\xi}^m \partial \bar{\xi}^n} \quad (\text{II-4})$$

which arises due to the transformation from $\bar{\xi}^i$ to ξ^i . A grid generation equation can then be defined from equations (II-1) and (II-2):

$$\nabla^2 \xi^i = \sum_{j=1}^3 \sum_{k=1}^3 g^{jk} p_{jk}^i \quad (i=1,2,3) \quad (\text{II-5})$$

Equation (II-5) implies that a coordinate system is generated which corresponds to the application of a stretching transformation to the coordinate system generated for maximum smoothness.

Actually, P_{jk}^i is to be specified rather than obtained through a subsequent transformation. In practical applications, it is the Cartesian coordinates x_i , ($i=1,2,3$) that are to be sought in the transformed uniform field. Hence Eq. (II-5) should be rewritten with Cartesian coordinates as dependent variables. Carrying out the transformation of Eq. (II-5), Ref. [13], and setting $\nabla^2 \mathbf{r} = 0$ yields

$$\sum_{i=1}^3 \sum_{j=1}^3 g^{ij} \left(\mathbf{r}_{\xi^i \xi^j} + \sum_{k=1}^3 P_{ij}^k \mathbf{r}_{\xi^k} \right) = 0 \quad (\text{II-6})$$

where \mathbf{r} is the position vector. If one considers only one-dimensional stretching in each coordinate direction, the control function can be further simplified as

$$P_{jk}^i = \delta_j^i \delta_k^i P_i$$

where $\delta_j^i = 1$ if $i=j$ and 0 otherwise. With this simplification, Eq. (II-6) becomes

$$\sum_{i=1}^3 \sum_{j=1}^3 g^{ij} \mathbf{r}_{\xi^i \xi^j} + \sum_{k=1}^3 g^{kk} P_k \mathbf{r}_{\xi^k} = 0 \quad (\text{II-7})$$

In this work, the concept of solution-adaptive grid generation is investigated by formulating a definition of the control function P_k in Eq. (II-7) in terms of flow parameters from PDE flow solvers.

II.2 Truncation Error

As noted above, a grid system must be generated before numerical simulations of fluid flow can be performed. Since the solution is not known a priori, it is very difficult to generate a grid system optimal to the problem at hand. The accuracy of numerical simulations is significantly affected by the truncation error, which is inherently introduced into the flow solution algorithms when the derivatives in the governing fluid flow equations are represented by finite difference or finite volume approximations. Therefore when a grid network is generated, attention should be given to minimizing the truncation errors. In Refs. [1,14], Mastin has considered the following first derivative in one dimension:

$$f_x = \frac{f_\xi}{x_\xi} \quad (\text{II-8})$$

where f : solution function
 x : Cartesian coordinate
 ξ : curvilinear coordinate

With a central difference for f_ξ and x_ξ , Eq. (III-1) can be written as, with $\Delta\xi=1$,

$$f_x = \frac{f_{i+1} - f_{i-1}}{x_{i+1} - x_{i-1}} + T$$

where the truncation error T can be reduced to the following form:

$$T = -\frac{1}{2} x_{\xi\xi} f_{xx} - \frac{1}{6} x_{\xi\xi}^2 f_{xxx} \quad (\text{II-9})$$

If the point distribution of the grid system is fixed, it can be shown that the error represented by Eq. (II-9) is second order and is proportional to $1/N^2$, where N is the number of grid points, Ref. [1]. This means that the error will be quartered when the number of grid points is doubled. On the other hand, if the number of grid points is fixed, the second term in (II-9) represents a power of the spacing. The intent of a change of point distribution is then to decrease the local spacing where the local gradient of a flow parameter is large. Consequently, the spacing must increase where the local gradient is relatively small. The first term in Eq. (II-9) is proportional to the second derivative of the solution and hence is diffusive. This term also contains the term $x_{\xi\xi}$, the rate of change of the grid-line spacing. This indicates that the changes in grid spacing should be kept small, because large changes in grid-line spacing will introduce significant truncation errors. Mastin has also shown that the truncation error due to nonorthogonality is inversely proportional to the sine of the angle between two curvilinear coordinates, Ref. [14]. Therefore, in order to minimize truncation errors, it is necessary to maintain orthogonality throughout the grid networks as far as is practical. At boundaries, orthogonality becomes more important because one-sided difference approximations are often applied, and in the case of viscous flow, the thin layer turbulence modeling are logically constructed in the direction normal to the boundaries, Ref. [15]. There are two different approaches employed in this study to achieve the grid orthogonality at boundaries. In the first approach, the slope of grid lines at the boundaries is iteratively adjusted to be orthogonal while the locations of grid lines at boundaries are fixed, Ref. [14,16]. In the second

approach, the grid points at the intersections of grid lines with the first line or surface off the boundaries are fixed and then the grid lines are allowed to relocate with orthogonality at the boundaries, Refs. [4,14,16,17].

The task of generating grid networks with reduced truncation errors based upon known solution information; i.e., solution-adaptive grid generation, can be accomplished by either adding additional grid lines or clustering existing grid lines to the regions where high gradients of flow parameters in the field occur. In this work, the solution-adaptive grid generation technique is investigated with grid networks of fixed numbers of grid points, using the control function approach as indicated in Eq. (II-7).

II.3 Control Function Approach

The basic idea of solution-adaptive grids is to reduce errors by generating grids with grid cells that contain equal amounts of some positive weight function, Refs. [4,5,6,18]. In one dimension, equidistribution occurs when the spacing between grid points is inversely proportional to the weight. In differential form, assuming a transformation from a curvilinear coordinate to the Cartesian coordinate along a given curve, this can be written

$$W(x) dx = c d\xi \quad (\text{II-10})$$

where W : weight function
 c : proportional constant

In the transformed uniform space in ξ , $d\xi$ is viewed as a constant. The desired spacing is then obtained when the spacing shrinks or expands as the weight function $W(x)$ increases or decreases, respectively. Integrating Eq. (II-10) over a cell,

$$\int_{x_i}^{x_{i+1}} W(x) dx = c \int_{\xi_i}^{\xi_{i+1}} d\xi = c(\xi_{i+1} - \xi_i) \quad (\text{II-11})$$

where $\xi_{i+1} - \xi_i = \text{constant}$

Eq. (II-11) states that the total weight over each cell is kept constant. In discrete form, Eq. (II-11) becomes

$$W_{i+\frac{1}{2}} (x_{i+1} - x_i) = \text{constant} \quad (\text{II-12})$$

$$\text{where } W_{i+\frac{1}{2}} = \frac{1}{2} (W_{i+1} + W_i)$$

Here again, if the weight function is large, x_{i+1} and x_i approach each other. From Eq. (II-10), we have

$$W(x) x_{\xi} = \text{constant} \quad (\text{II-13})$$

Differentiating with respect to ξ , we get

$$x_{\xi\xi} W + x_{\xi} W_{\xi} = 0 \quad (\text{II-14})$$

Rewriting the general three-dimensional elliptic equation (II-7) in one dimension,

$$x_{\xi\xi} + P x_{\xi} = 0 \quad (\text{II-15})$$

From Eqs. (II-14) and (II-15), we obtain

$$P = - \frac{x_{\xi\xi}}{x_{\xi}} = \frac{W_{\xi}}{W} \quad (\text{II-16})$$

as the control function in terms of weight function and its derivative. Extending Eq. (II-16) to all three directions, Refs. [19,20],

$$P_i = \frac{W_{\xi^j}}{W} \quad (i=1,2,3) \quad (\text{II-17})$$

The complete generalization of (II-16) is, as given by Eiseman, Ref. [18],

$$P_i = \sum_{j=1}^3 \frac{g^{ij}}{g^{ii}} \frac{(w_i)_{\xi^j}}{w_i} \quad (i=1,2,3) \quad (\text{II-18})$$

This definition of the control functions involves the derivatives of the weight function in three directions, with each weighted by its corresponding contravariant metric tensor element g^{ij} . This provides a convenient means to specify three separate control functions. For instance, one may specify the pressure gradient as the weight function in one direction and the velocity gradient in another. Equation (II-17) is in fact the diagonal terms of Eq. (II-18). When the pressure gradient is used to define the weight function, it can be written

$$W = 1 + |\nabla p| \quad (\text{II-19})$$

The pressure gradient term in the above equation tends to concentrate more grid lines in the high pressure gradient region, while the 1 tends to produce equal spacing, Ref. [14].

When a grid system is generated using the elliptic equation (II-7), a set of control functions can be generated based upon the geometrical characteristics of the grid, Ref. [1]. If only the control

functions based upon gradients of flow parameters are used to regenerate a new grid, then the geometrical characteristics of the existing grid will be lost. In order to preserve the geometrical characteristics of the existing grid, it is logical to construct useful control functions in such a manner that the control functions defined in Eq. (II-18) be a correction factor to the previous set of control functions, i.e.,

$$P_i = (P_{\text{initial geometry}})_i + c_i(P_{wt}) \quad (i=1,2,3) \quad (\text{II-20})$$

where $P_{\text{initial geometry}}$: control function based on initial grid geometry

P_{wt} : control function based on gradient

c_i : constant

The constant c is to be specified to weight the control function based upon gradients. Referring to Eqs. (II-7) and (II-20), the elliptic system used to generate the solution-adaptive grid is then

$$\sum_{i=1}^3 \sum_{j=1}^3 g^{ij} r_{\xi^i \xi^j} + \sum_{k=1}^3 g^{kk} P_k^{(n)} r_{\xi^k} = 0 \quad (\text{II-21})$$

which is solved by the point over-relaxation method to generate new adaptive grids, Ref. [16]. The superscript (n) in Eq. (II-21) is the sequential number of grid adaptations. During the investigation, however, it was found that for a given set of weight constants; i.e., the c_i 's in Eq. (II-20), the progress of grid adaptation was relatively slow. A different construction of the control functions based upon the current grid rather than the initial grid and the flow gradients was tried. This can be formulated as follows.

$$P_i^{(1)} = (P_{\text{initial geometry}})_i^{(0)} + c_i(P_{wt})^{(0)} \quad (i=1,2,3)$$

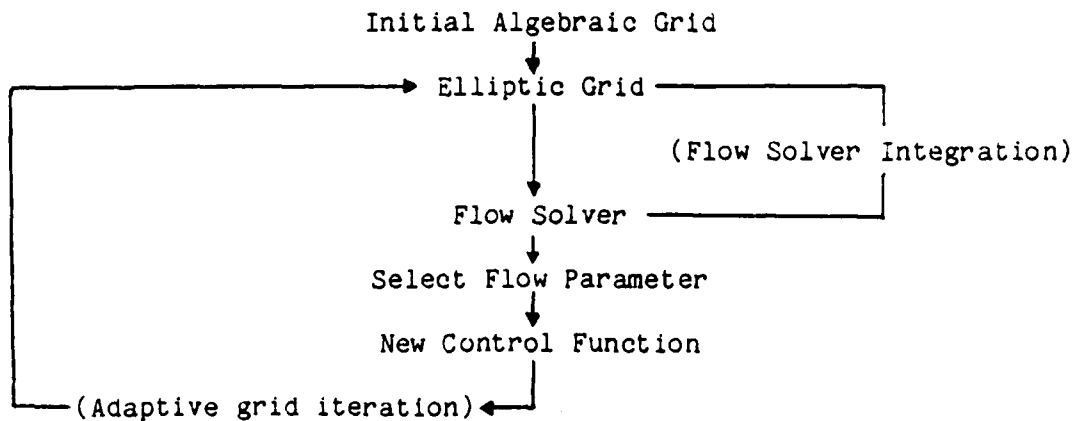
$$P_i^{(2)} = P_i^{(1)} + c_i(P_{wt})^{(1)} \quad (i=1,2,3) \quad (\text{II-22})$$

•
•
•

$$P_i^{(n)} = P_i^{(n-1)} + c_i(P_{wt})^{(n-1)} \quad (i=1,2,3)$$

where the superscripts indicate the sequential number of grid adaptations. The $P_i^{(1)}$, $P_i^{(2)}$, ... $P_i^{(n)}$ are then control functions corresponding to the 1st, 2nd, ... nth adaptive grids respectively. It was found that the progress of grid adaptation based upon Eq. (II-22) is much more efficient than that based upon Eq. (II-20). This will be demonstrated in Chapter III.

The iterative process of solution-adaptive grid generation is implemented as follows:



Since in this work the solution-adaptive grid generation code was constructed by coupling the EAGLE (Eglin Arbitrary Geometry ImpLicit Euler) grid and flow codes, Refs. [10,16], brief descriptions of the features of these codes are in order here.

II.4 EAGLE Grid Code

The EAGLE grid code, Ref. [16] is a general three-dimensional elliptic grid generation code based on the block structure with control function approach. This code allows any number of hexahedronal blocks to be used to fill an arbitrary three-dimensional physical region, with each of the hexahedronal blocks corresponding to a rectangular computational block. This composite-block structure of the code is very flexible. A block can be connected to other blocks through entire or partial sides of the corresponding blocks, or to itself, with complete continuity, with slope continuity, with only line continuity or discontinuity across the interfaces between connecting blocks. Except in the case of discontinuity, all the connecting blocks must have the same number of points on their common interfaces. In the case of complete continuity, the interface is a branch cut and a correspondence across the interface in terms of object points and image points, Ref. [1], is established by using an extra layer of points surrounding the corresponding blocks. This allows the points on the interface to be treated as all other points so that the continuity is retained. The physical location of the interfaces are thus totally unspecified, being determined by the code.

The elliptic characteristics of a mesh is achieved by using control function approach, Ref. [1]. The control function can be evaluated either from the initial algebraic grid and then smoothed, or by interpolation from the boundary point distributions. In the latter case, the arc length and curvature contributions to the control functions are evaluated and interpolated separately into the mesh from the appropriate boundaries, and the control function at each point in the mesh is then formed by combining the interpolated components. This procedure allows very general regions, with widely varying boundary curvature, to be treated.

The boundary orthogonality can be achieved by Neumann boundary conditions, Ref. [1], which allows the boundary points to relocate over a surface spline. The new locations of the boundary points are determined by Newton iteration with the grid lines normal to the surface spline. Alternatively, the boundary orthogonality can be achieved by iterative adjustment of the slope of a grid line until the grid line is normal to the surface. In the latter case, the location of the grid point on the surface, however, is fixed, Ref. [1]. The Neumann boundary approach was employed in this study to obtain both orthogonality and solution-adaptive grid.

II.5 EAGLE Flow Code

The EAGLE flow code is a three-dimensional unsteady Euler fluid flow solver capable of simulating aerodynamics around complex three-dimensional geometries with composite-blocked grid systems, Ref. [10]. The governing equations of the EAGLE flow code are the three-dimensional time-dependent Euler equations, which consist of the conservation laws of mass, momentum

and energy, and the equation of state of an ideal gas. For the advantage of boundary-conforming grids and the simplicity of performing computations in uniform space, the equations are scaled and transformed onto a three-dimensional curvilinear coordinate system. An implicit, finite volume, upwind, flux-vector of flux-difference split, approximate factorization numerical technique is then applied to solve the equations, Ref. [10]. A solution is obtained by a two-factor scheme which consists of solving a sparse block lower triangular matrix system with forward substitution followed by solving a sparse block upper triangular matrix system with backward substitution through the computational domain. Various boundary conditions, such as impermeable surface, farfield subsonic or supersonic inflow/outflow were implemented to facilitate the simulation of physical boundary conditions. The interface of a blocked grid system is treated in terms of phantom or image points, Ref. [10]. The dependent variables corresponding to a block interface are stored and made available for the adjacent block when they are needed. For steady state solution, the dependent variables at the interface are unsynchronized; i.e., the code takes whatever time level values are present when they are needed. Numerical results obtained so far has shown that for steady state solution, there appears to be no degradation in convergence or stability, Ref. [10]. In this work, the flux-difference split option of the flow code was used.

CHAPTER III

RESULTS AND DISCUSSION

The solution-adaptive grid generation technique with the control function approach as described in the previous chapter was tested with two complex three-dimensional multiple-blocked configurations at transonic flow conditions: (1) an eight-block finned body of revolution at an angle of attack of 12 degrees with a Mach number of 0.95, (2) a thirty-block multiple-store ogive-cylinder-ogive configuration at an angle of attack of zero degree with a Mach number of 0.95. The results obtained are discussed in the following sections.

III.1 Finned Body of Revolution

The structure of the grid system used for the finned body of revolution was generated by using the EAGLE surface generation code, Ref. [21] and the EAGLE grid generation code, Ref. [16] and is shown in Figures 2 through 5. Figure 2 shows the outer boundary of the grid and the location of the body within the grid, while Fig. 3 shows the grid on the surface of the body and that extended from the body toward the outer boundary. Figures 4 and 5 show the detailed view of the grid at the nose section and tail section of the body, respectively. In Fig. 5, the fins were removed for clarity. The grid consists of eight blocks: four blocks in the nose section and four blocks in the tail section, with four fins located circumferentially at angular intervals of 90 degrees. Each block was dimensioned 69x25x13. The elliptic option of the grid generation code was used to generate the initial grid with Neumann boundary conditions specified on the nose section of the

body, except for several grid lines in front of the leading edge of the fins which intersect the body at an angle of about 55 degrees and render the application of Neumann boundary conditions inappropriate there, Ref. [16]. Except for these Neumann boundary points, all the grid points on the solid surface of the body are fixed points, Ref. [16]. This can be seen in Figs. 4 and 5. This grid system is a modified version of that used in Ref. [22]. The differences are that the grid lines are uniformly distributed in the circumferential direction here, and that the orthogonality of grid lines is maintained at the surface as described above.

The aerodynamics around the body was first solved without using the solution-adaptive technique and then with the solution-adaptive technique. Comparison was then made between the two results. The pressure and Mach contours with the initial grid at an angle of attack of 12 degrees and a Mach number of 0.95 after 1000 iterations with CFL = 4.0 are shown in Figs. 6 and 7. In these figures, the fins are again removed for clarity. It is clear that there is a matrix of shocks around the body. A strong shock occurs at the leeward side of the nose section and its strength decreases in the circumferential direction toward the windward side. There is a lambda shape shock at about the middle of the upper tail section. There also are shocks around the base of the body. The glitch line starting from the junction between the nose and tail section toward the outer field with an angle of about 55 degrees is due to the deficiency of the plot routine used. Similar glitch lines present in almost all the contour plots reported in this work and are due to the deficiency of the plot

routine used. The solution-adaptive grids based upon Eq. (II-20) in Chapter II, using pressure gradients as weight functions, at the same flow conditions; i.e., $Mach = 0.95$, $\alpha = 12$ deg. were obtained at 200, 300, 400, 500, and 600 iterations of flow solutions with the concentration constant $c = 5.0$. The fifth adaptive grid, i.e., the one obtained after the 600th iteration is displayed in Fig. 8. It can be observed that only slight clustering of grid lines occur in response to the shocks in the flow field. This is not very effective.

The case was repeated at exactly the same flow conditions, except that Eq. (II-21) was employed in constructing control functions. The solution-adaptive grids as before, were obtained with the concentration constant $c = 5.0$ at 200, 300, 400, 500, and 600 iterations and are displayed in Figs. 9 thru 13, respectively. When compared with Fig. 6 or Fig. 7, it is clear that the grid lines are gradually clustering around areas where shocks occur in the flow field. Figure 14 shows the detail of the adaptive grid at the nose section with five adaptations. The grid lines cluster more closely on the leeward side of the body and then gradually relax the clustering effect in the circumferential direction toward the windward side of the body. This is exactly in response to the characteristics of the shock that occurred in the flow field. Around the frontal area of the nose section, the grid lines move toward the body in response to the high pressure gradients occurring around the area. This can be observed in Fig. 13 or Fig. 14. Figure 15 displays a close-up of the adaptive grid at the shock. It is interesting to note that in this test case the spacing of the adaptive

grid lines at the shock is approximately one-tenth of that of the initial grid. In addition, the orthogonality of the grid lines at the solid surface is maintained where Neumann boundary conditions were applied. The details of the fifth adaptive grid at the tail section are shown in Fig. 16. Here again, the clustering of the grid lines occurs at the middle of the tail section and the base of the body, in response to the shocks there. Although from Figs. 6 and 7, there are small shocks between the lambda shock and the shock at the base, the grid lines there do not appear to cluster effectively. This is most likely due to the fact that the strengths of these shocks are weak relative to those at the middle section and the base. The flow solver calculation was carried out to 1000 iterations with the fifth adaptive grid. The corresponding pressure contours are shown in Fig. 17. Compared with Fig. 6, it can be observed that the shocks are more clearly defined with the adaptive grid. This can be more easily seen in Figs. 18 and 19, which display the shock in the leeward side of the nose section with the initial grid and with the adaptive grid respectively.

In Fig. 18, the shape of the shock is not well defined. The width of the shock is wide while in Fig. 19, the shape of the shock is much more clearly defined. The width of the shock is much more narrower. This clearly demonstrates the advantage of the adaptive grid over the non-adaptive grid that with adaptive grid the simulation of the aerodynamics is much closer to the reality. The pressure contours on the surface of the nose section with the initial grid and with the adaptive grid are shown in Figs. 20 and 21 respectively. Again, the width of the shock with the adaptive grid is narrower than with the initial

grid. As mentioned before, the apparent glitch line at the middle of the body in the axial direction in Figs. 20 and 21 is due to the deficiency of the plot routine used.

It is also observed that the shape of the lambda shock at the middle of the tail section is more clearly defined with the adaptive grid, Fig. 6. The corresponding Mach contour is shown in Fig. 22. As in the pressure contour plots, the shocks are more clearly defined with the adaptive grid. Figures 23 and 24 show the detail of the frontal shock with the initial grid and with the adaptive grid, respectively. In Fig. 24, it can be observed that the shock is much more clearly defined on both the leeward side and windward side of the body. The movement of the grid lines on the body clearly reflected the characteristics of the variation of the pressure distribution, or equivalent Mach number, on the surface of the body. Throughout all the Figures that displayed grids, it can be observed that all the transitions of grid lines at the interface of adjacent blocks are very smooth. For example, in Figure 14, which shows the adaptive grid at the nose section with five adaptations, the seventh line from the top of the body in the circumferential direction is an interface between two blocks. The adaptive grid lines there cross the boundary very smoothly.

The calculated pressure distributions at various azimuthal locations along the body with and without the adaptive grids are plotted versus experimental data in Figs. 25 thru 30, while the pressure distributions along the fins are shown in Figs. 31 thru 38. Examination of the pressure distributions shows that although the adaptive grid does yield a much clearer definition of shocks in the flow

field, the pressure distributions with the adaptive grids in general do not differ significantly from that with the initial grid in this test case. This can be attributed to the fact that although the initial grid is not sufficient to yield a good definition of shocks, it appears adequate to yield reasonably good pressure distributions. Very similar observations can be made from the pressure distributions along the fins as shown in Figs. 31 thru 38. It is interesting to observe that because the body is at an angle of attack of 12 degrees and flow expands on the upper side of the fin surfaces, the effect of the adaptive grid is more readily observable on the upper side than on the lower side of the fin surfaces, as evidenced by comparing Figs. 35 and 37 with Figs. 36 and 38.

The density residual convergence histories for blocks one thru four and blocks five thru eight are shown in Figs. 39 and 40 respectively. The grid adaptation does cause disturbances in the residual convergence histories. The disturbances, however, diminish rapidly after several cycles of flow solution integration and do not adversely affect the overall residual convergence histories. Hence, attempts to do any averaging process on the flow variables for the newly generated adaptive grid do not appear necessary for steady state solutions. The extra central process unit (CPU) time needed for five adaptations was about 3.4% over that of the non-adaptive approach in this test case.

III.2 Multiple-Store Configuration

A more complex multiple-store configuration was also used to test the solution-adaptive grid generation technique. It consists of three ogive-cylinder-ogive stores. But, due to the symmetry of the configuration, only one-half of the configuration needed to be gridded for flow solution calculations, Ref. [23]. The grid system consists of thirty blocks. Figures 41 and 42 show the perspective view and Fig. 43 shows a cross sectional view of the composite grid system. Figures 44 and 45 show a perspective and a frontal view of the stores respectively. In reference to Fig. 46, which shows a cross sectional view of the configuration, the store at the upper right hand location is referred to as store 1 and the one at the middle location is referred to as store 2. Various sections are also indicated here for later reference. The configuration was tested at an angle of attack of zero degree with a Mach number of 0.95. In the following, the results obtained are discussed in reference to the various sections indicated in Fig. 46.

Figure 47 shows the initial grid at Section A-A. The pressure and Mach contours with the initial grid at 400 iterations of the flow solver calculation are displayed in Figs. 48 and 49. It is clear that a strong shock is located at the base of store 1. Here again, the glitch lines that appear on these contour plots are due to the deficiency of the plot routine used. Then the solution-adaptive grid generation technique was applied. Adaptive grids were obtained at 80, 120, and 160 cycles of the flow solver calculations and are shown in Figs. 50, 51, and 52 respectively. It is readily observable that the grid lines cluster at both the base and the nose of the store in

response to high pressure gradients in the areas. The corresponding pressure and Mach contours obtained at 400 cycles of the flow solver calculation with the third adaptive grid are shown in Figs. 53 and 54. It can be observed that the width of the shock is narrower with the adaptive grid. Hence, the adaptive grid does improve the quality of the simulation of the flow field. The calculated pressure distribution along the store at two locations namely, $\phi = 0^\circ$ and $\phi = 220^\circ$, are displayed versus experimental data, in Figs. 55 and 56 respectively. It is observed that the pressure distribution with the adaptive grid does not significantly differ from that with the initial grid. This is attributed to the fact that the initial grid is adequate for prediction of pressure distribution in this case.

The initial grid at Section B-B (see Fig. 46) is shown in Fig. 57 while the corresponding pressure and Mach contours are shown in Figs. 58 and 59 respectively. Strong shocks occur at the base area above, between and below the stores. The solution-adaptive grids at 80, 120, and 160 cycles are displayed in Figs. 60, 61, and 62 respectively. Again, the grid lines cluster in response to the pressure gradients in the flow field. The corresponding pressure and Mach contours are shown in Figs. 63 and 64. When compared with Figs. 58 and 59, the narrowing of the width of the shocks due to the effect of the adaptive grids is readily observable.

The initial grids of Sections C-C, D-D, E-E, and F-F, (see Fig. 46) are shown in Figs. 65, 67, 69, and 71 respectively, while the corresponding adaptive grids with three adaptations are displayed in Figs. 66, 68, 70, and 72 respectively. It is evident from these figures that

the solution-adaptive technique works very well. The extra CPU time needed for the calculation of the three adaptive grid generations, in this case, was about 8% over that without grid adaptation.

CHAPTER IV

CONCLUSIONS AND RECOMMENDATIONS

In attempting to numerically simulate fluid flow around vehicles, it is necessary to first generate a grid network over the domain of interest, and then a PDE flow solver is applied with the grid to obtain solutions. An appropriate grid system, however, is difficult to generate because the flow solution in a domain is not known a priori. A solution-adaptive grid generation technique capable of generating a proper grid network based upon solution information as the problem solution evolves appears very desirable. In this study, a solution-adaptive grid generation technique based upon an elliptic system with control functions has been investigated. The control functions are first evaluated by using the geometry of the initial elliptic grid, and then are corrected by a weight function based upon pressure gradients in the field provided by the flow solution. The elliptic grid generator with updated control functions is then applied to regenerate a new grid with more grid-line clustering around high pressure gradient regions in the flow field. The computation of the flow solution continues with the newly generated adaptive grid. The grid generation and the flow solver codes have been coupled together so that solution-adaptive grids can be generated automatically without any manual manipulation. The coupled computer code has been implemented on a CRAY-2 computer system. Orthogonality may be specified in some desired regions in a grid, while smoothness is implicit in the elliptic equations. The application of the code has been demonstrated by the two test cases presented in this study, namely, an eight-block finned body

of revolution and a thirty-block multiple stores configuration. The results obtained have shown that the solution-adaptive approach does provide improved grids for the problems.

The applicability of the code can also be extended. For instance, the control function can assume the form of a combination of pressure gradient and other flow parameters, such as velocity gradient or density gradient. Furthermore, different concentration factors can be given to each individual flow parameter in different coordinate directions. For example, it is conceivably advantageous to assign more weight to pressure gradients in the streamwise direction and to velocity gradients in the direction normal to solid surface boundaries, if a thin-layer Navier-Stokes type flow solver is employed. The determination of the concentration factors and the number of adaptations, however, is still empirical. It would be worthwhile to develop an intelligent expert system which is capable of automatically determining the concentration factors and number of adaptations over a wide range of flow conditions to increase the robustness of the approach.

In conclusion, the solution-adaptive grid generation technique does provide proper grid networks for fluid flow simulations and should be an integral part of future computational fluid dynamics.

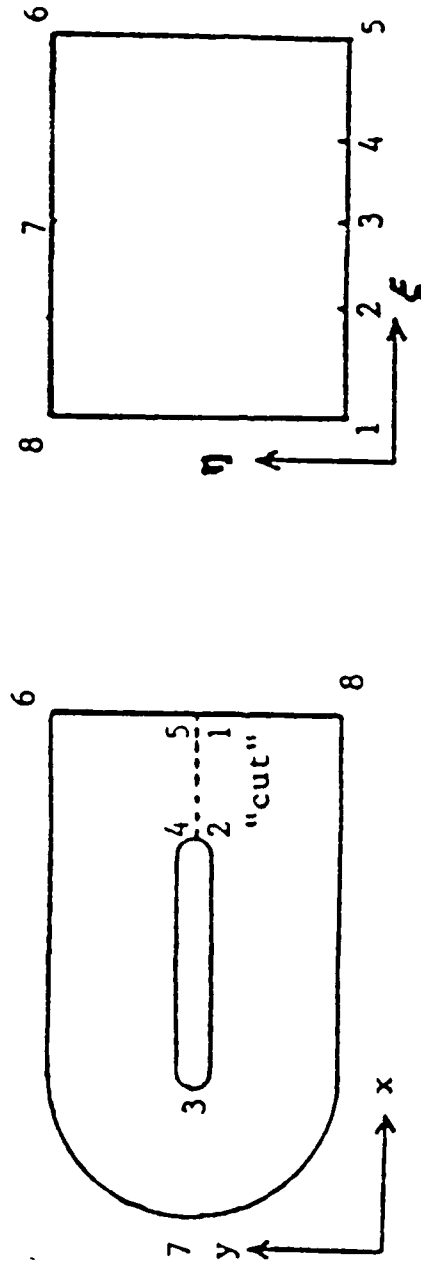


Figure 1. Physical and Computational Domain

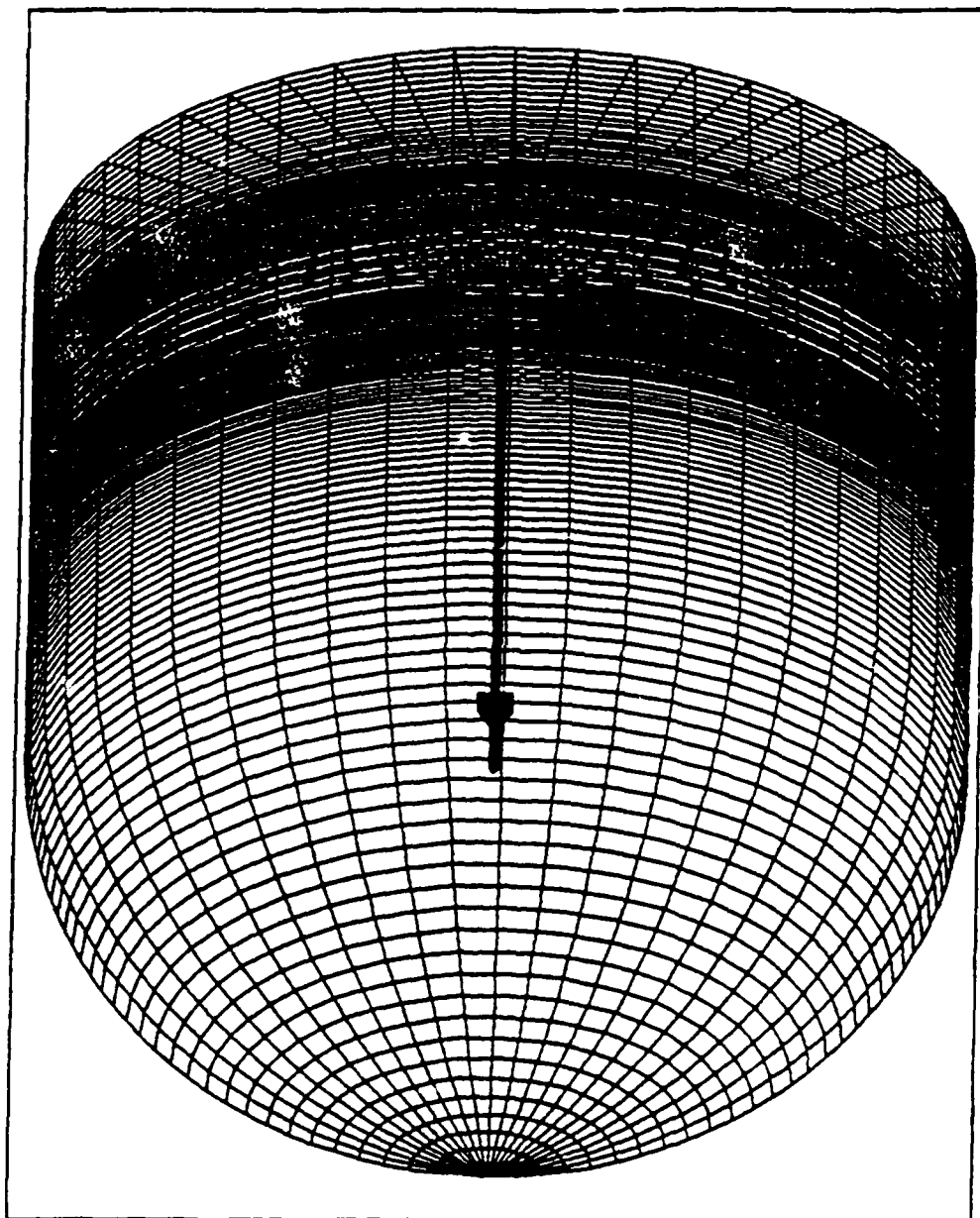


Figure 2. Overall View of Grid System

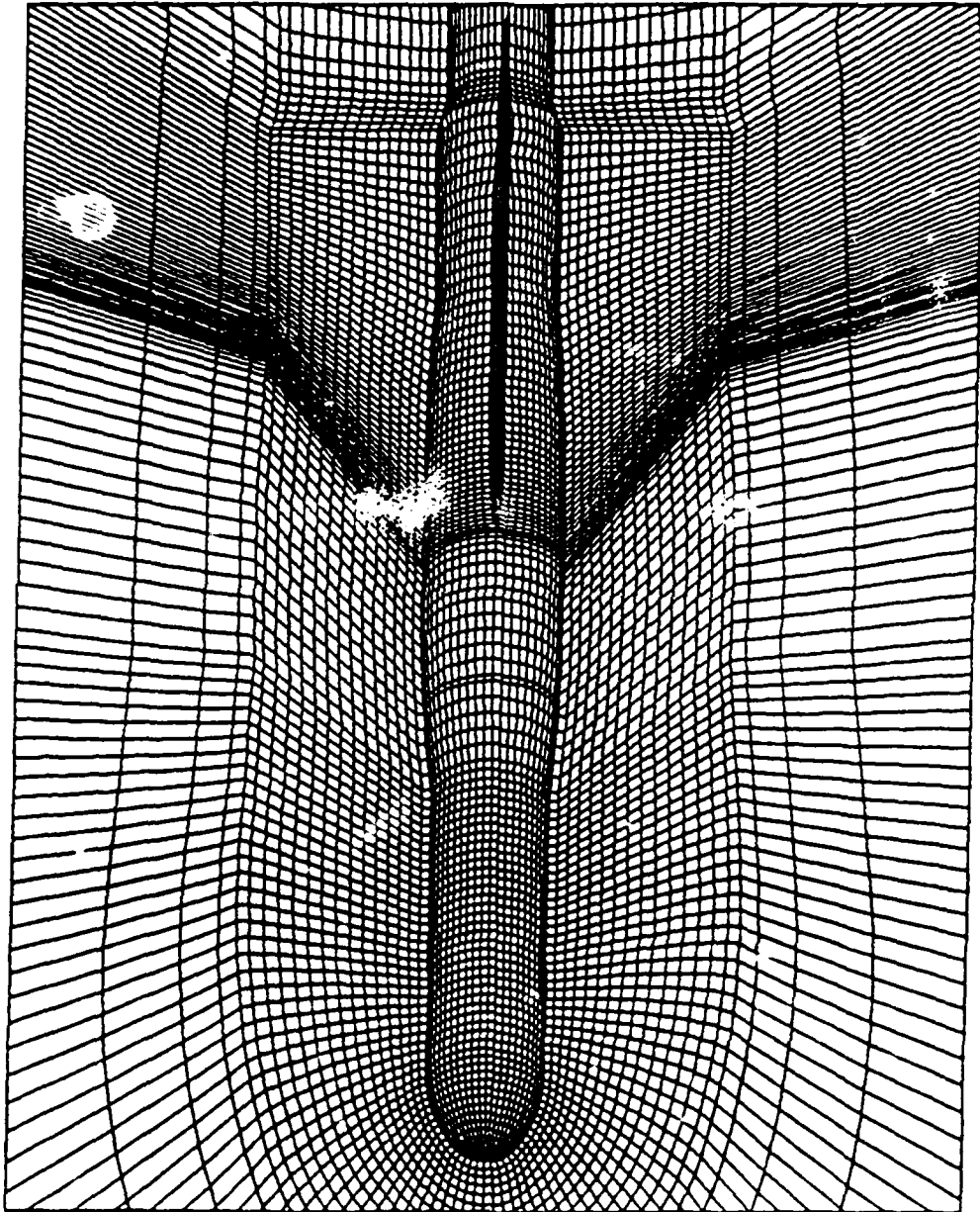


Figure 3. Initial Grid of Finned Body of Revolution

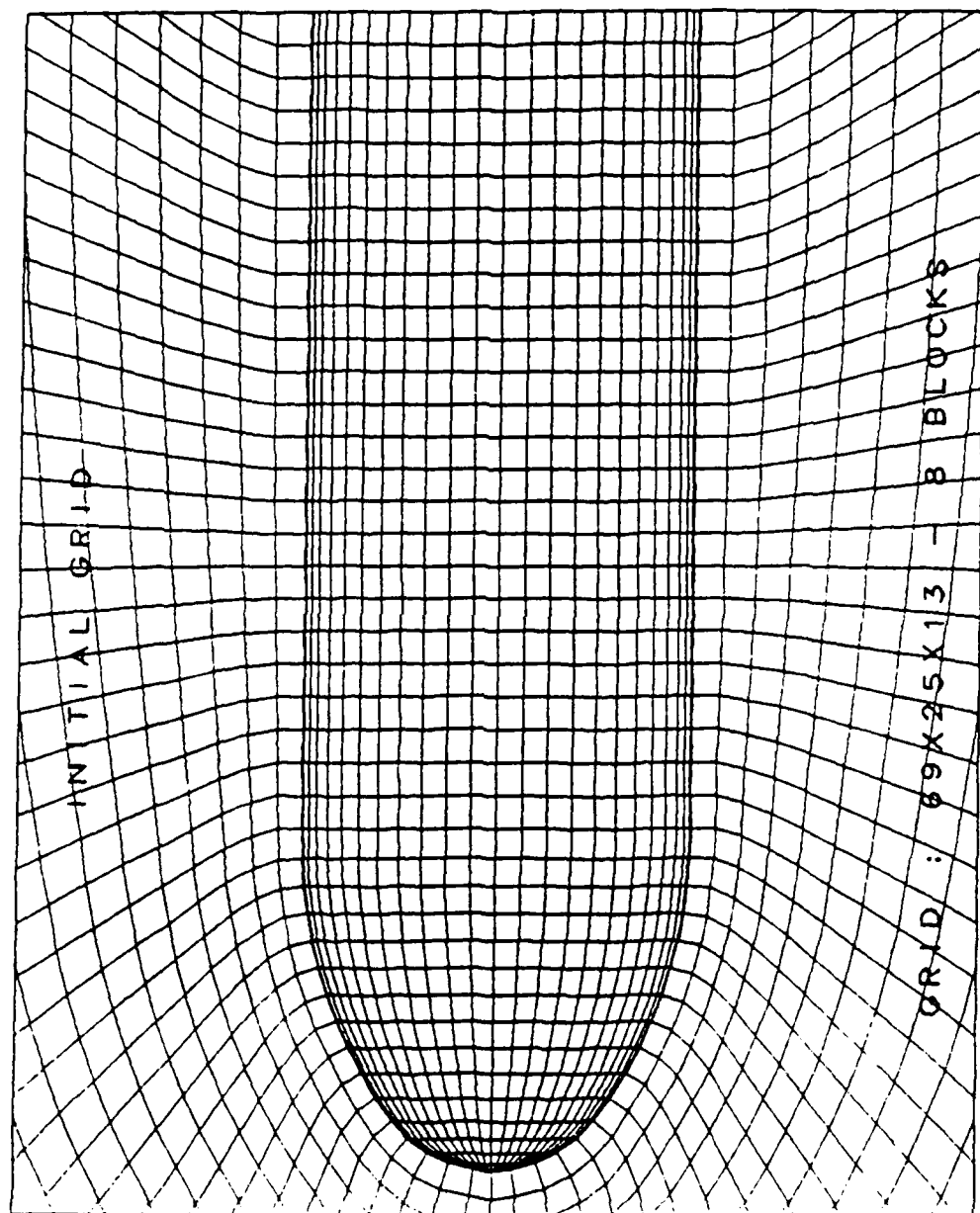


Figure 4. Initial Grid - Nose Section

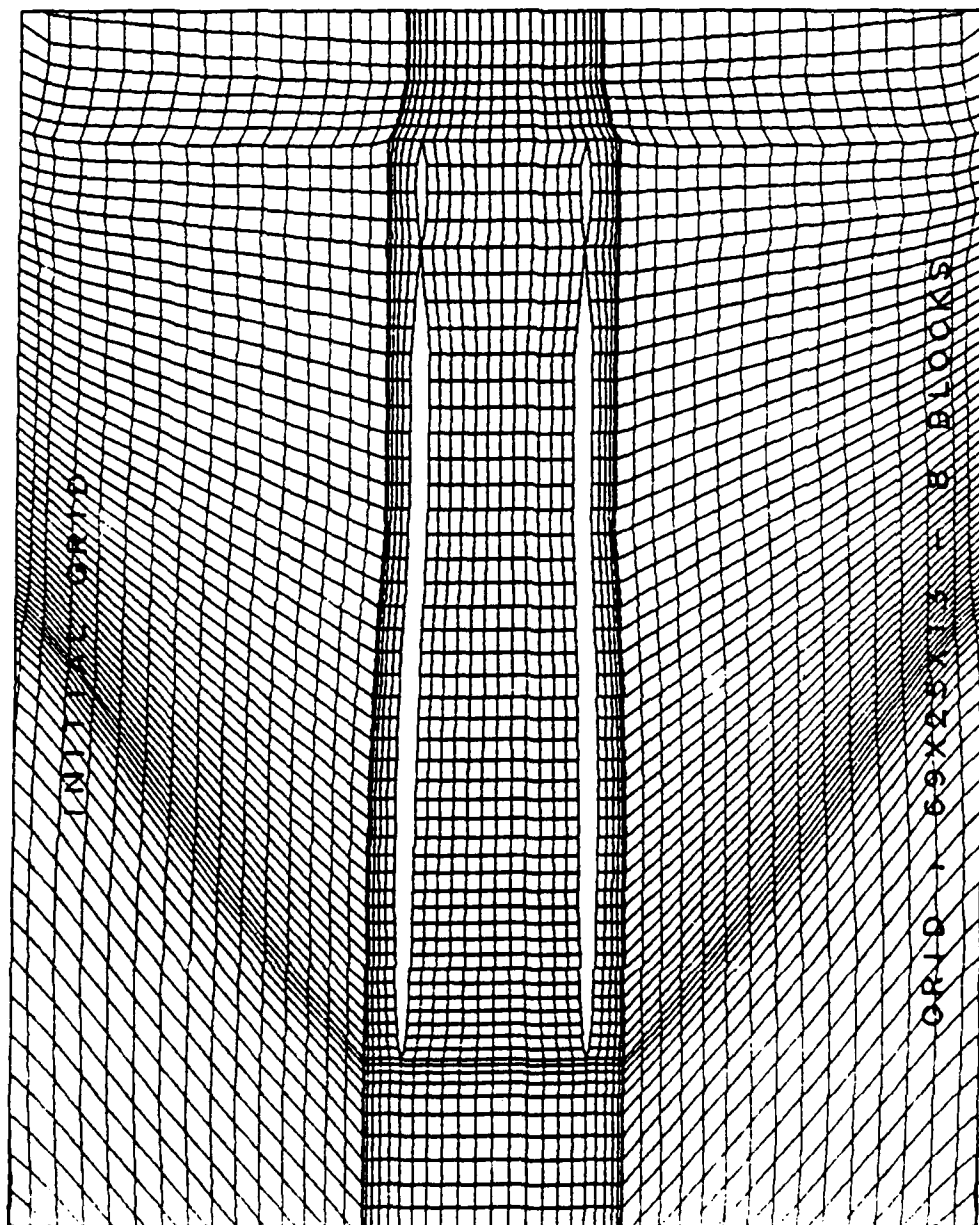


Figure 5. Initial Grid - Tail Section

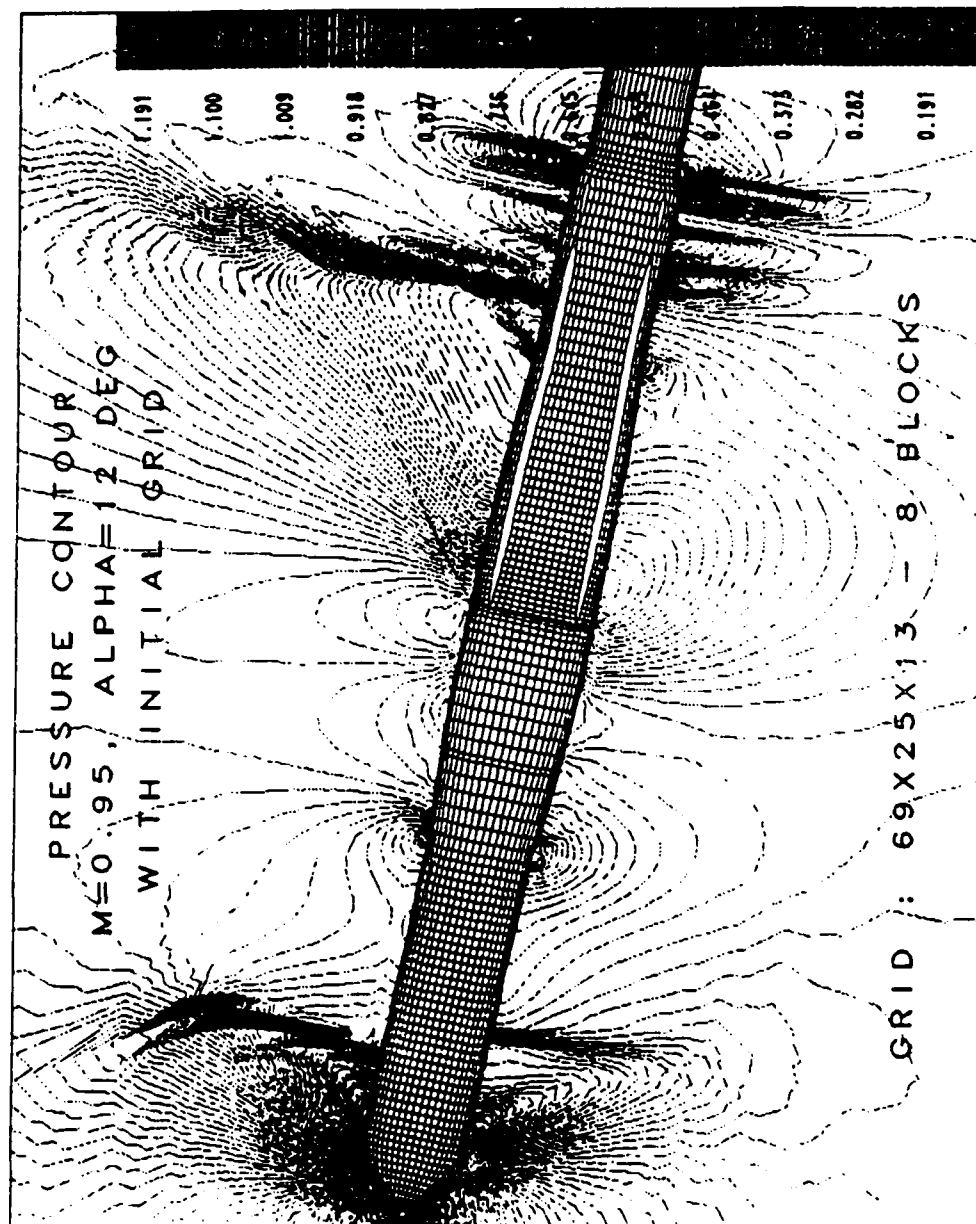


Figure 6. Pressure Contours with Initial Grid

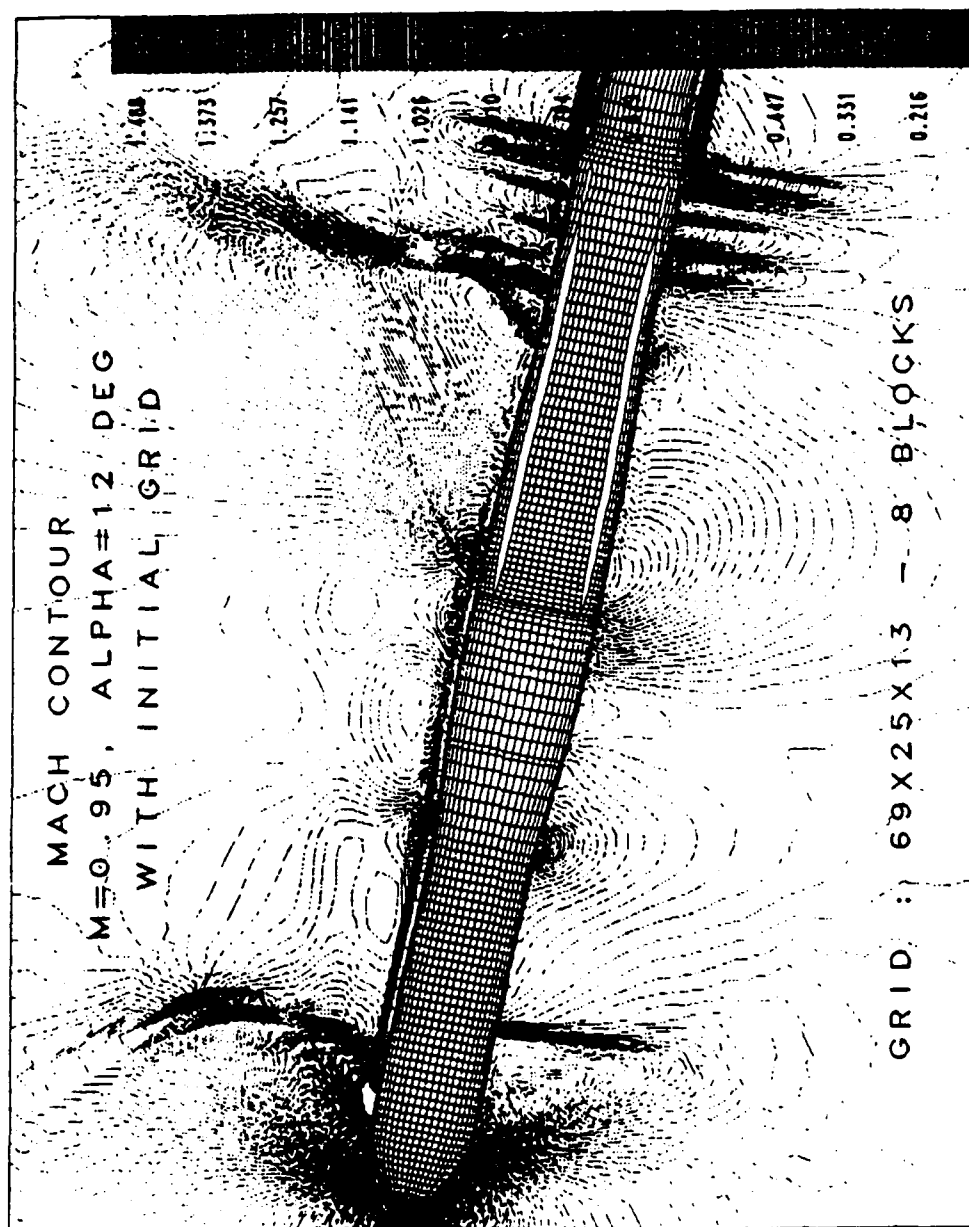


Figure 7. Mach Contours with Initial Grid

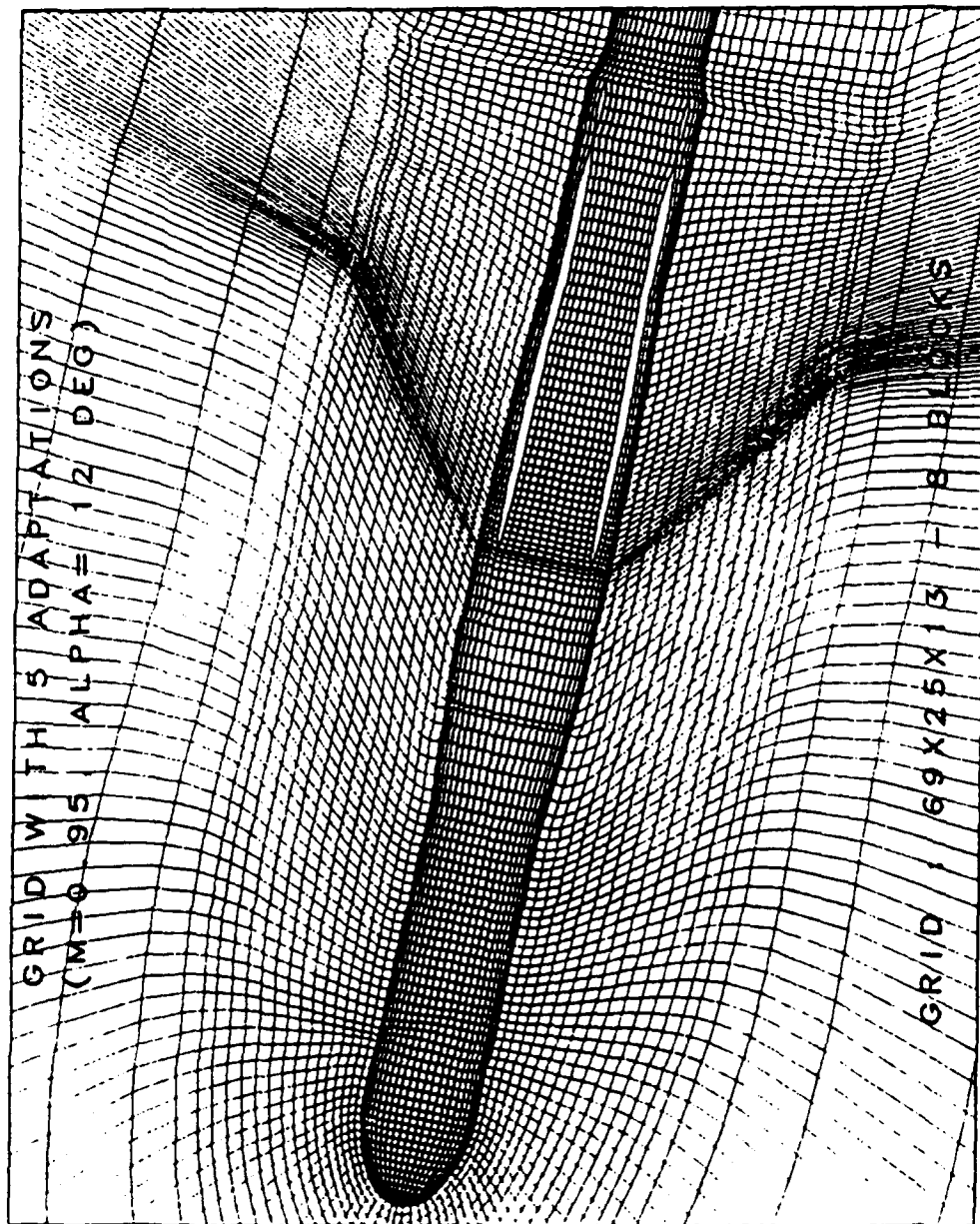


Figure 8. Fifth Adaptive Grid with Equation (II-20)

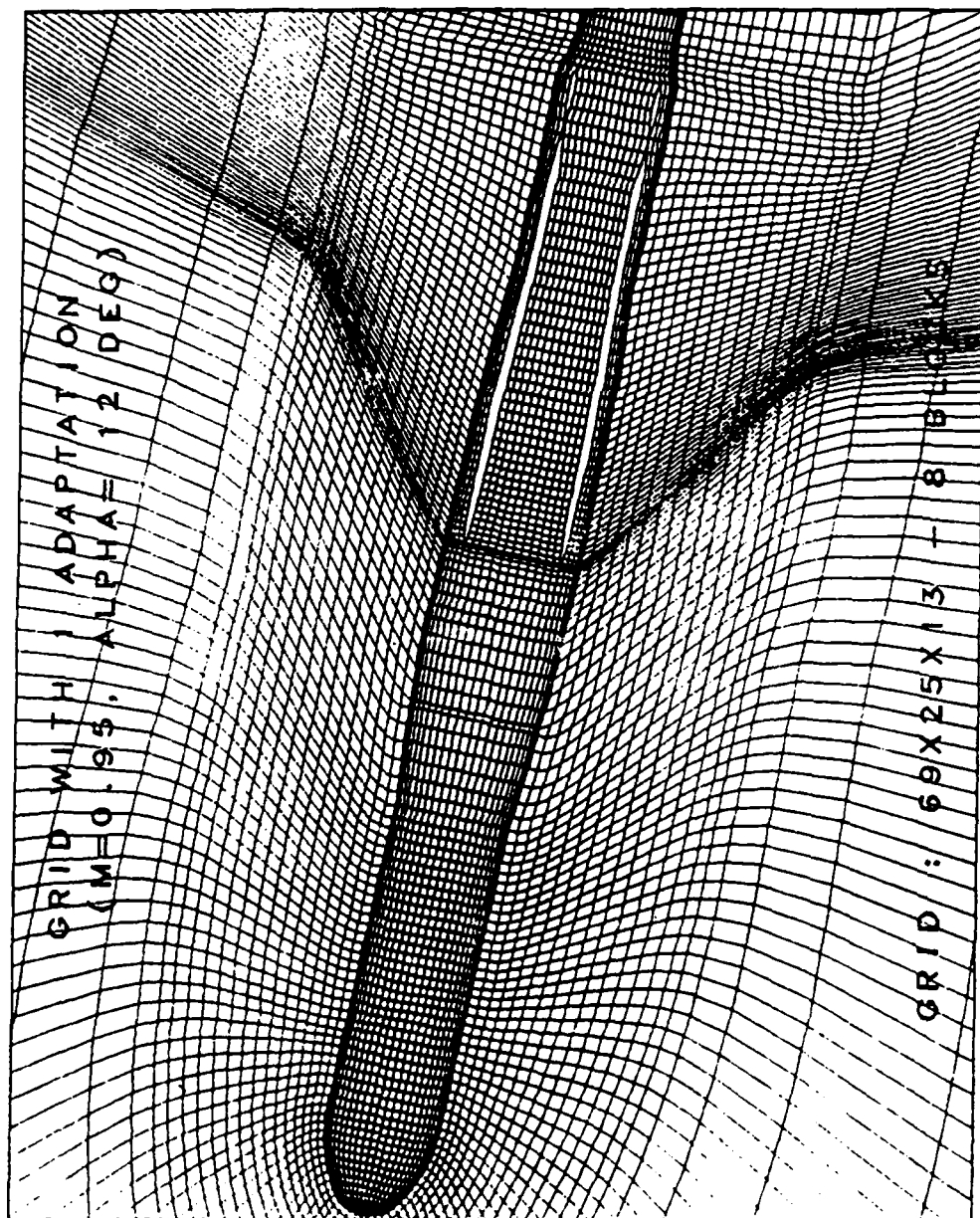


Figure 9. First Adaptive Grid

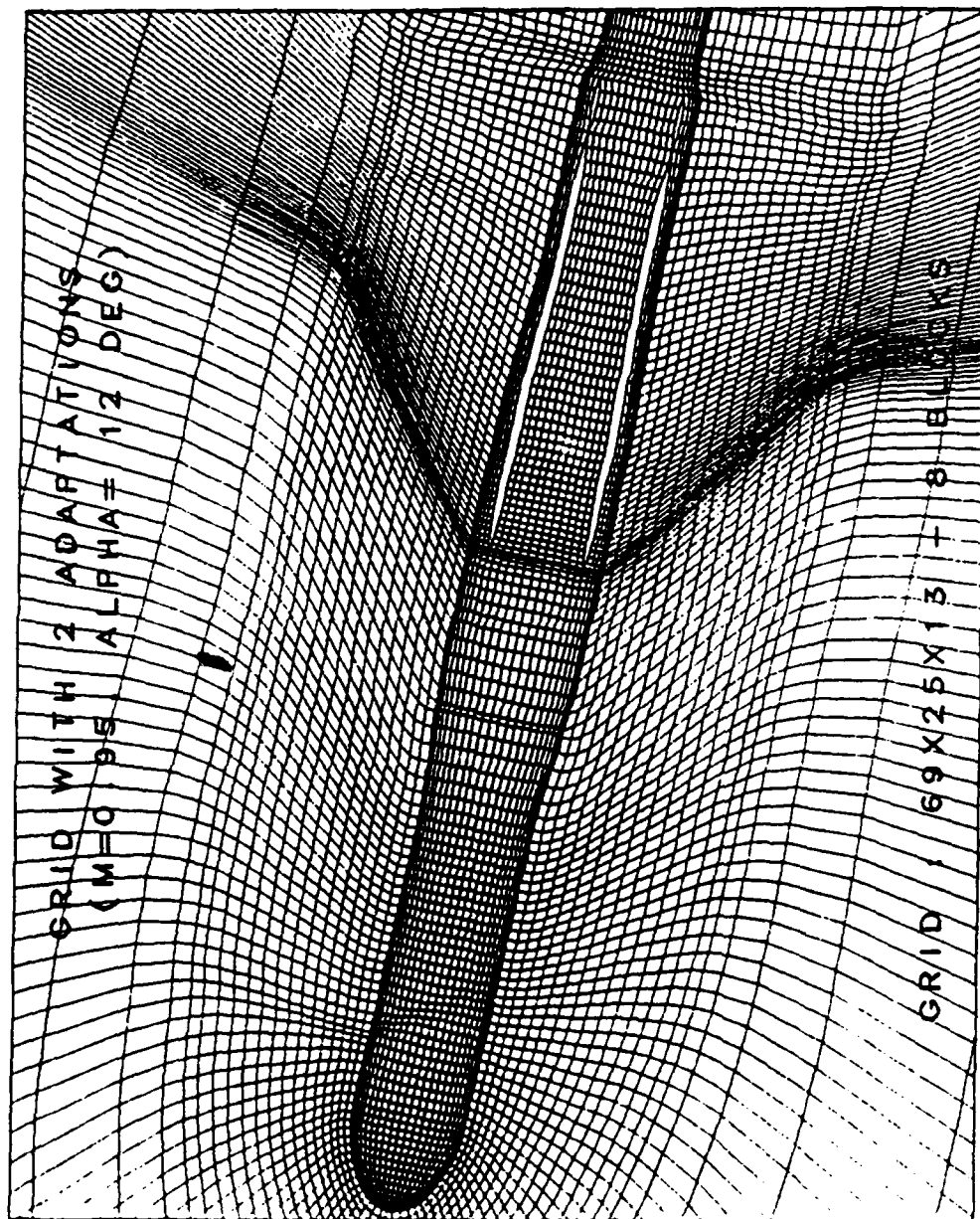


Figure 10. Second Adaptive Grid

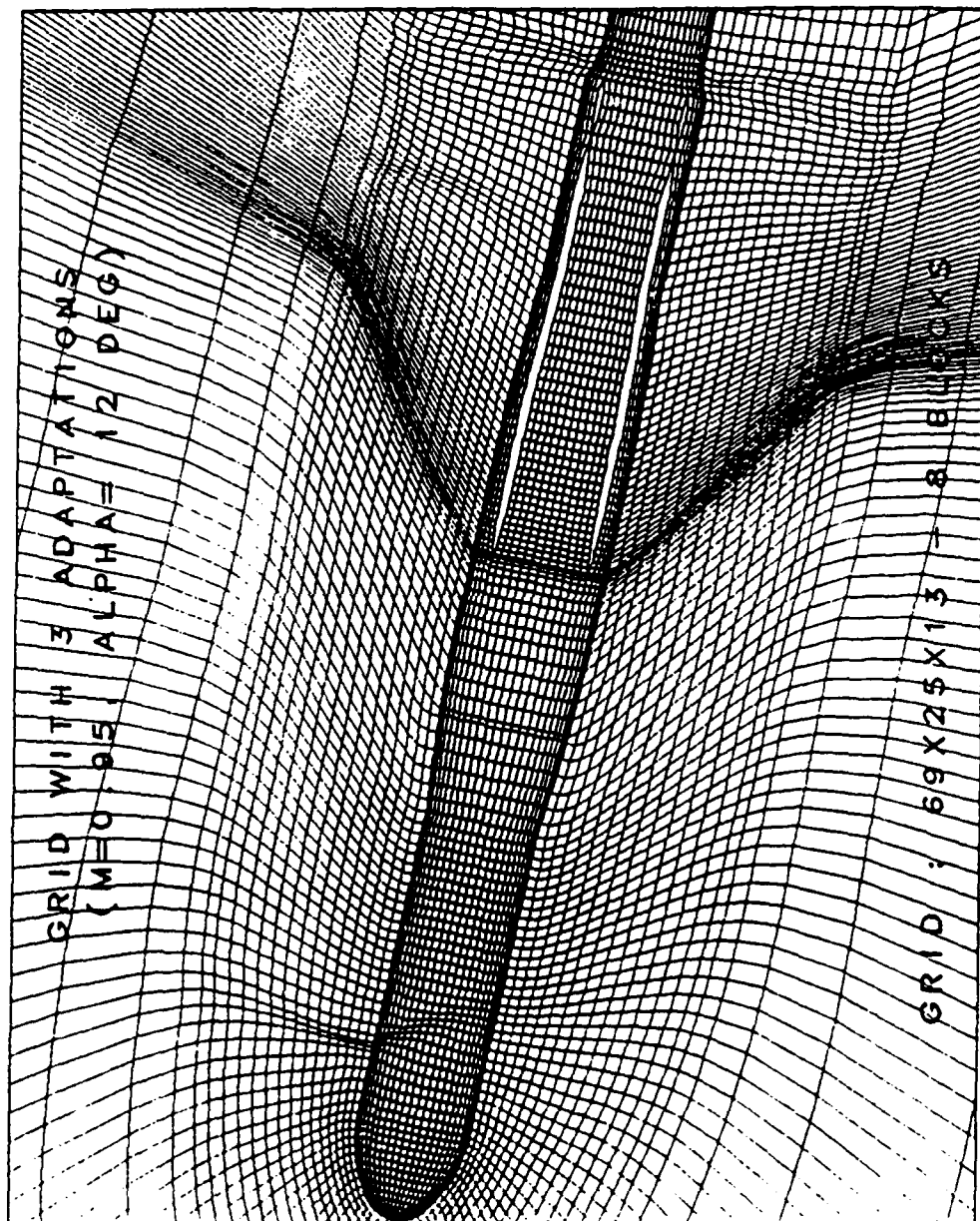


Figure 11. Third Adaptive Grid

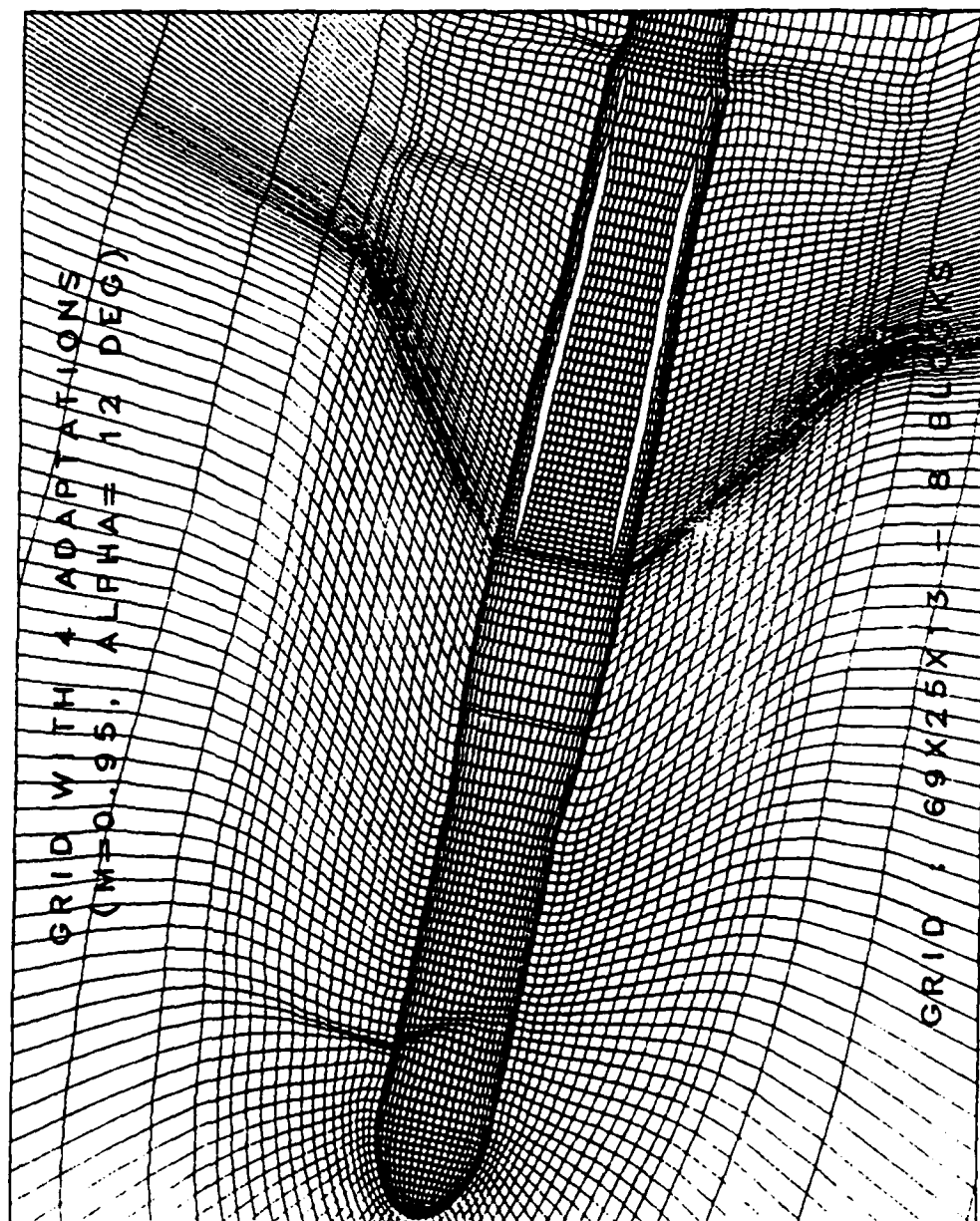


Figure 12. Fourth Adaptive Grid

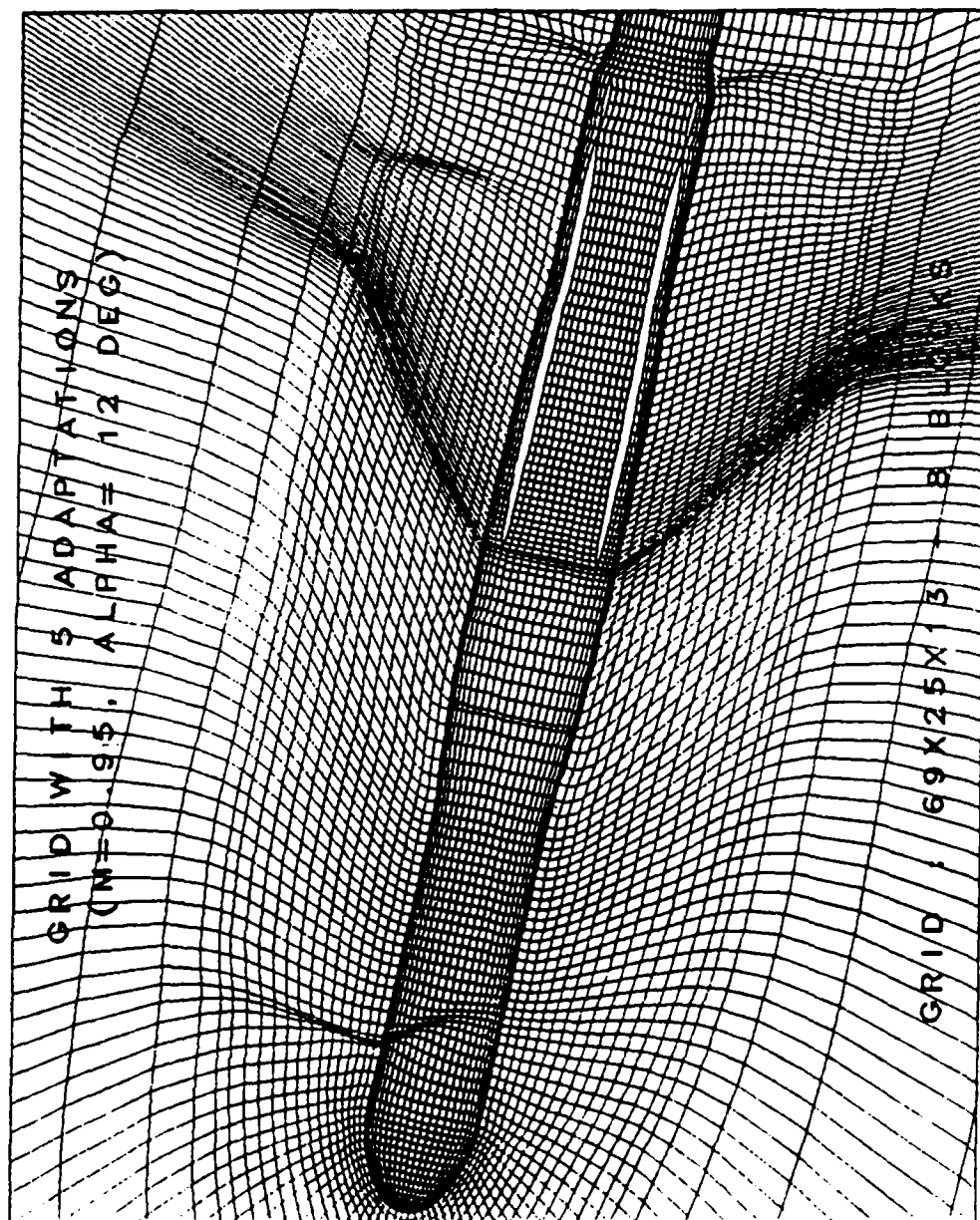


Figure 13. Fifth Adaptive Grid

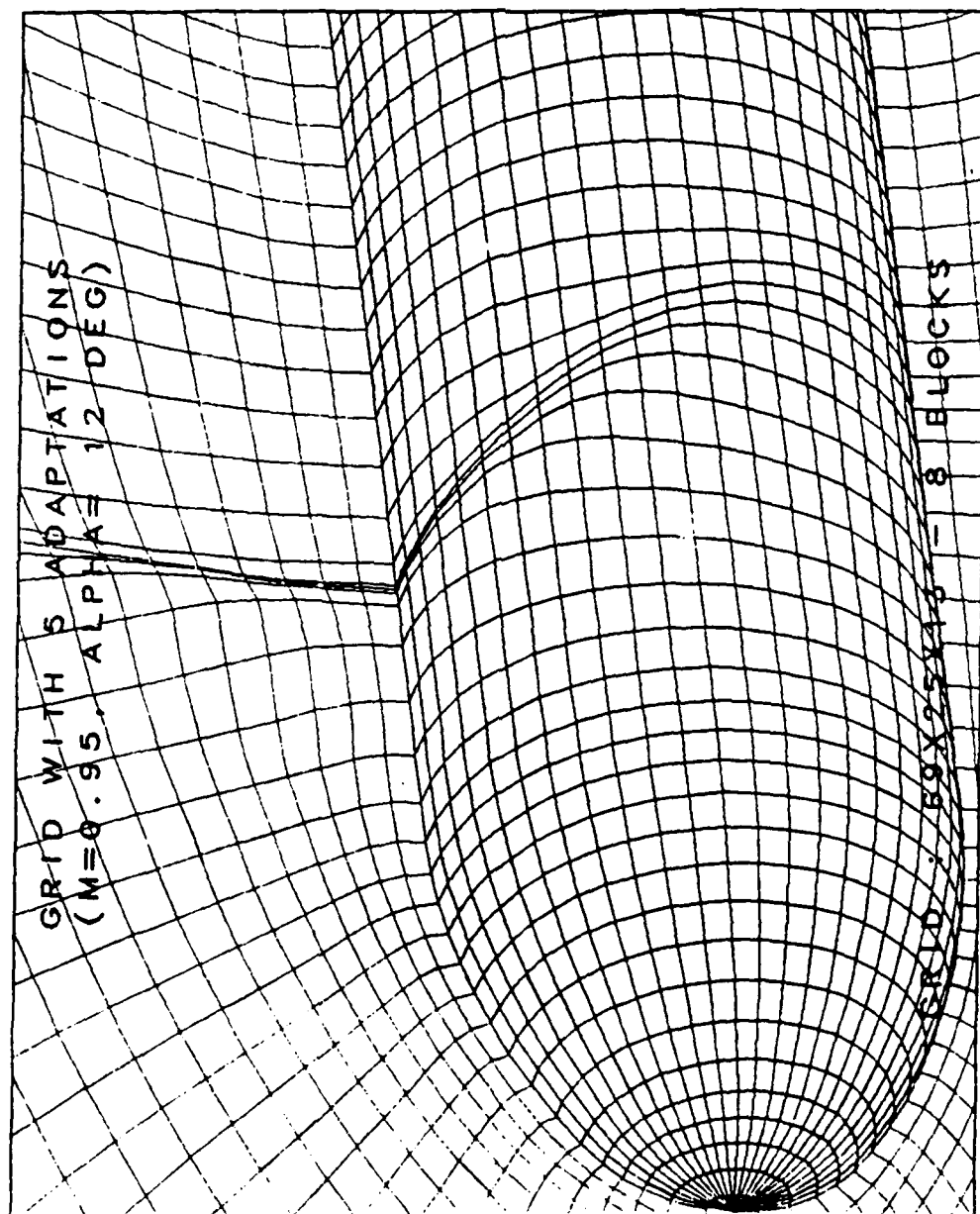


Figure 14. Adaptive Grid at Nose Section with Five Adaptations

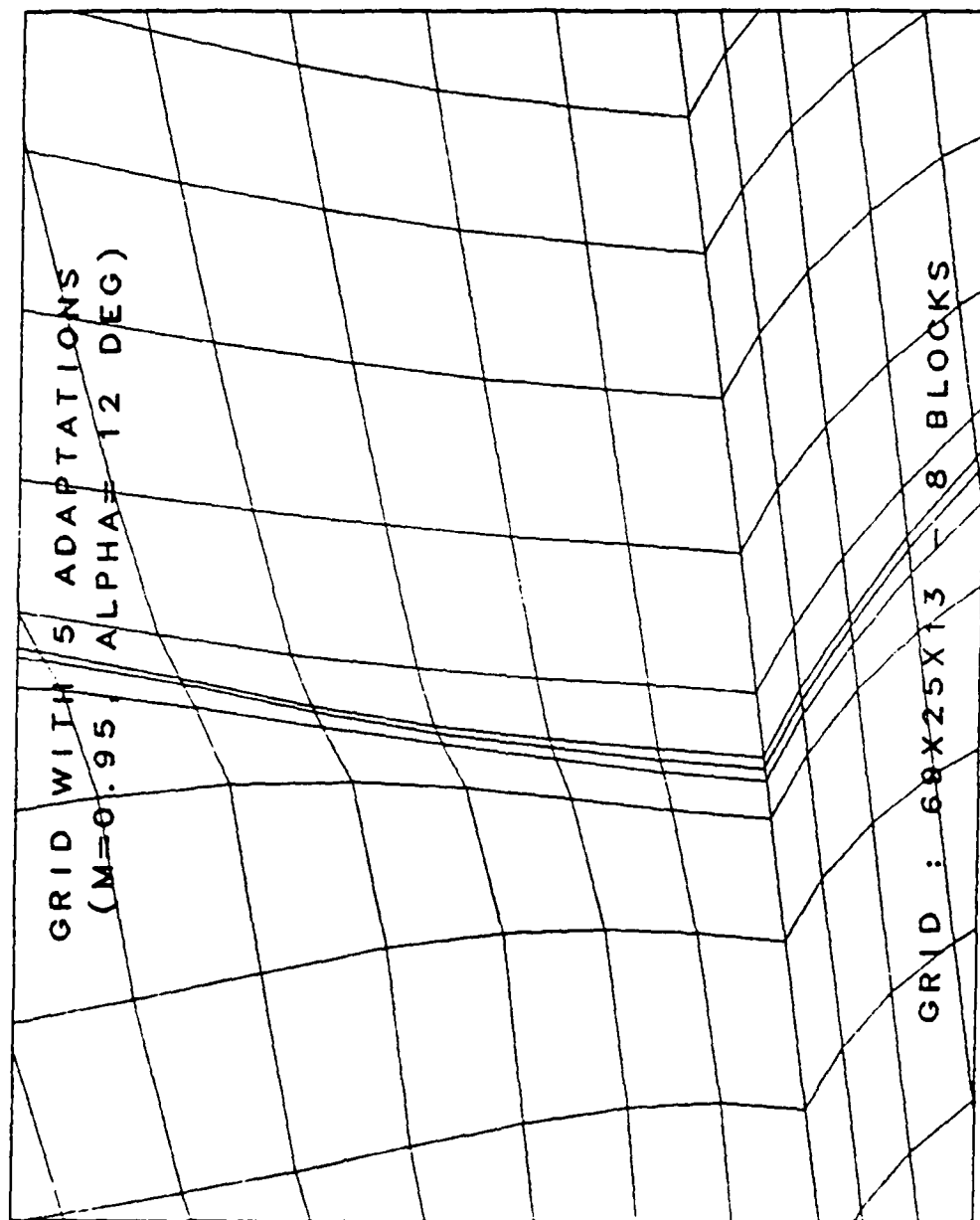


Figure 15. Adaptive Grid at the Shock - Nose Section

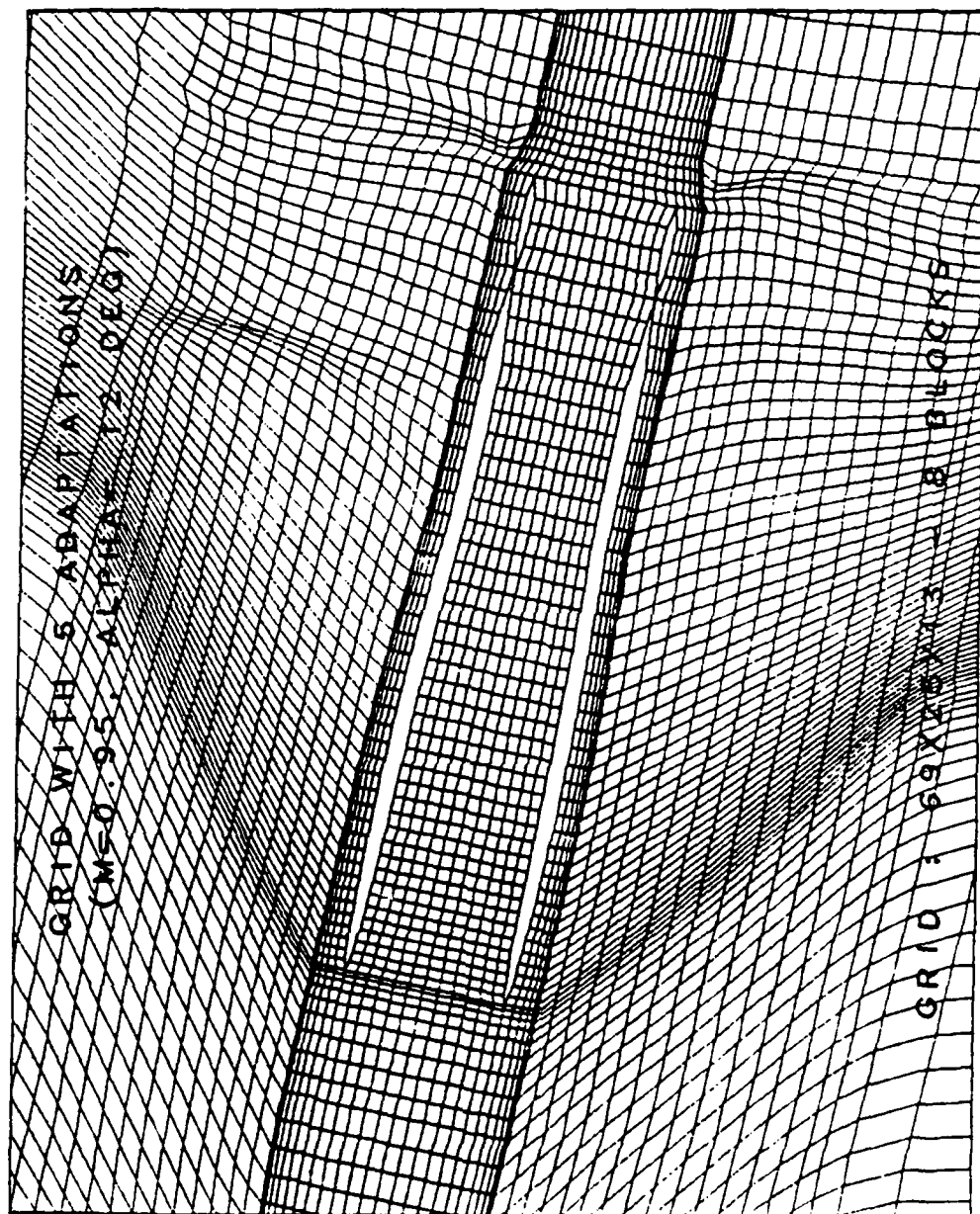


Figure 16. Adaptive Grid at Tail Section with Five Adaptations

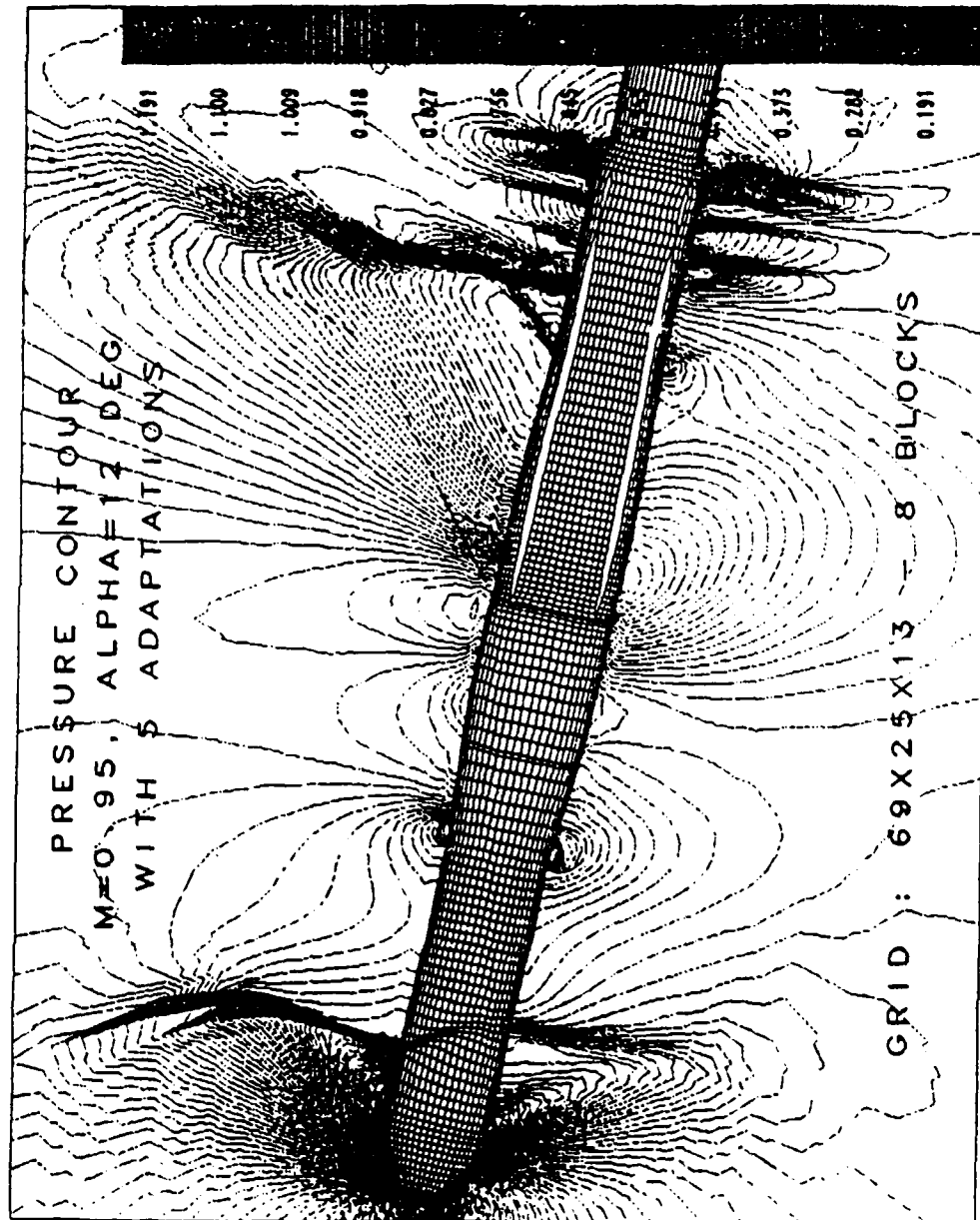


Figure 17. Pressure Contours with Five Adaptations

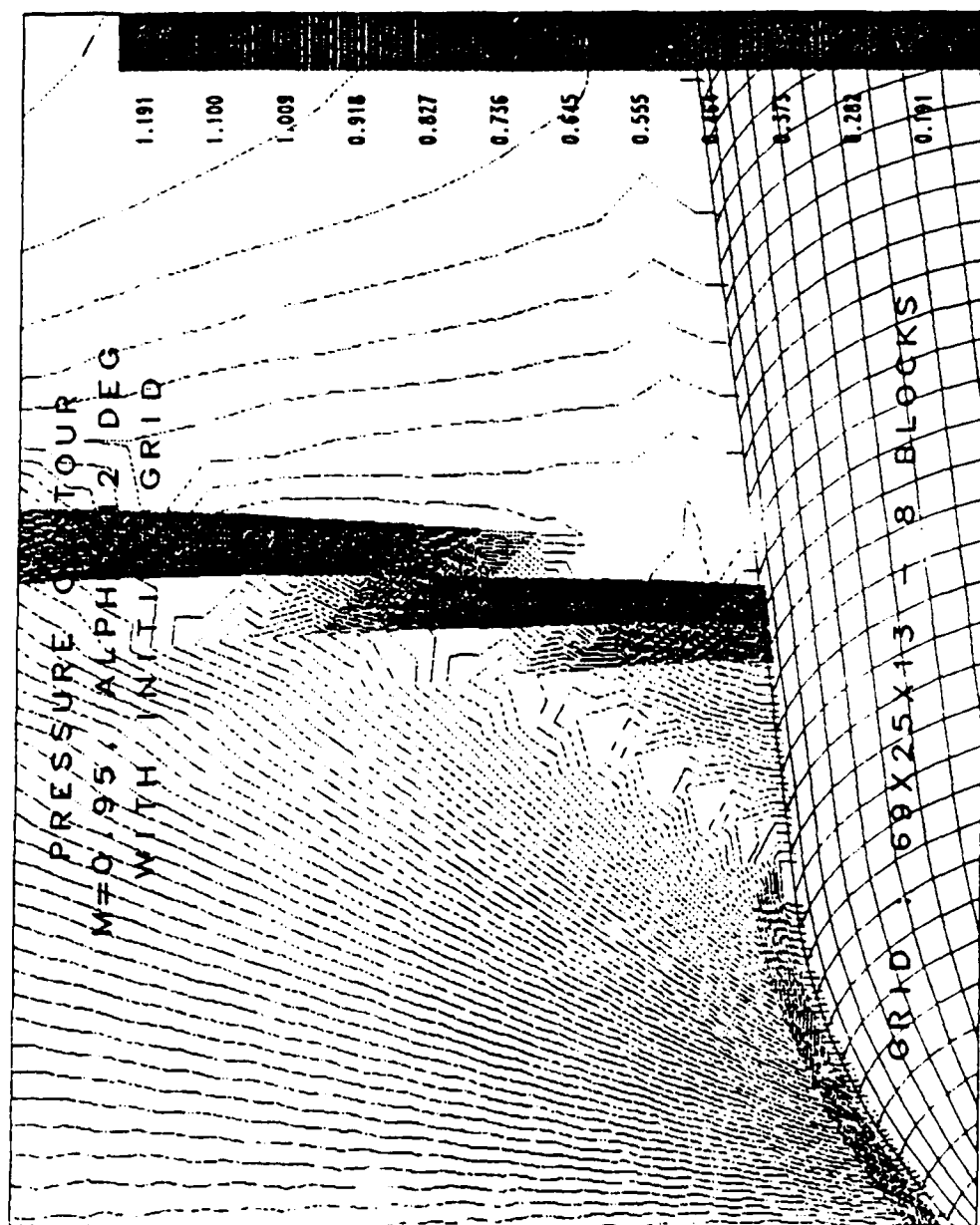


Figure 18. Shock with Initial Grid - Pressure Contour

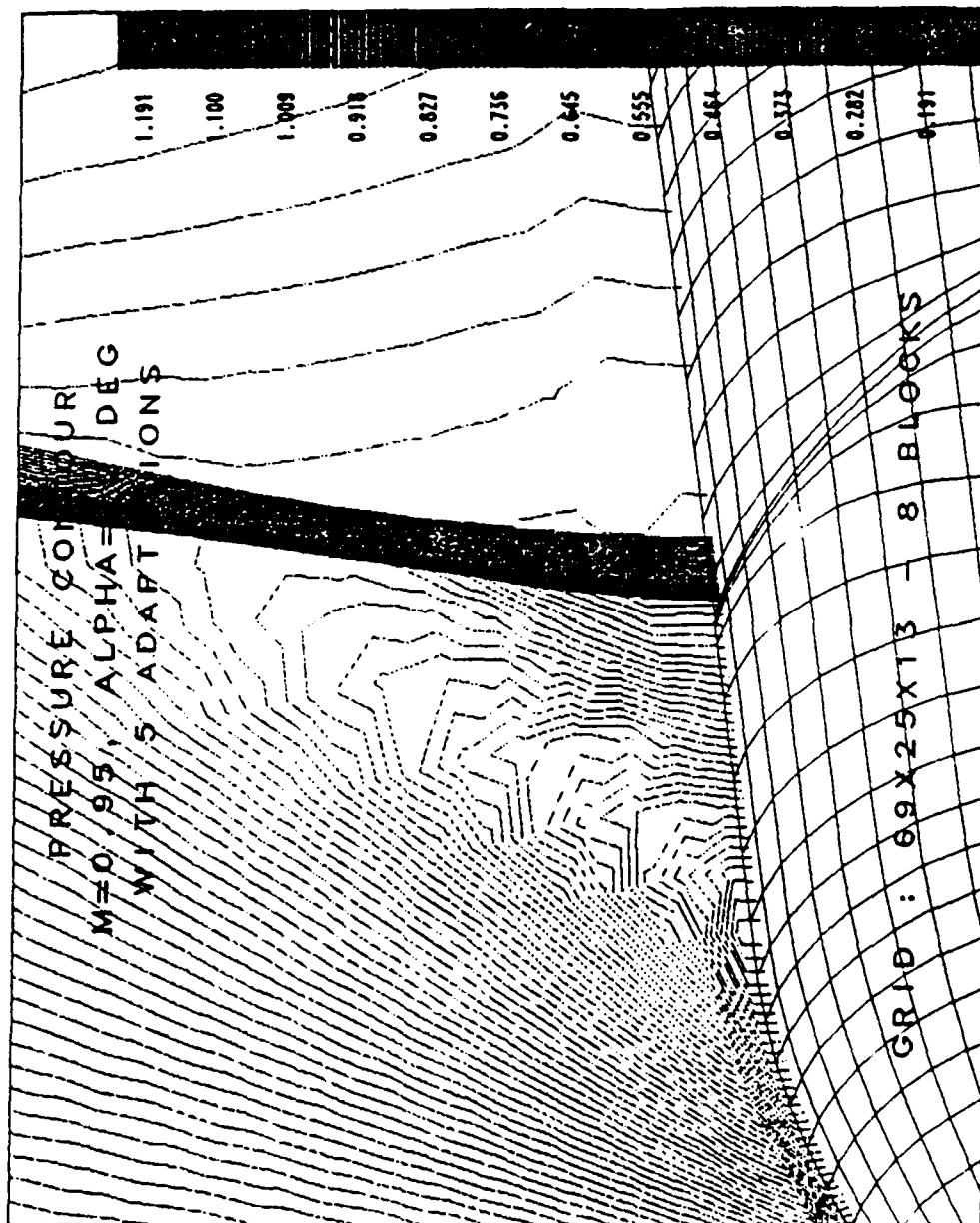


Figure 19. Shock with Five Adaptations - Pressure Contour

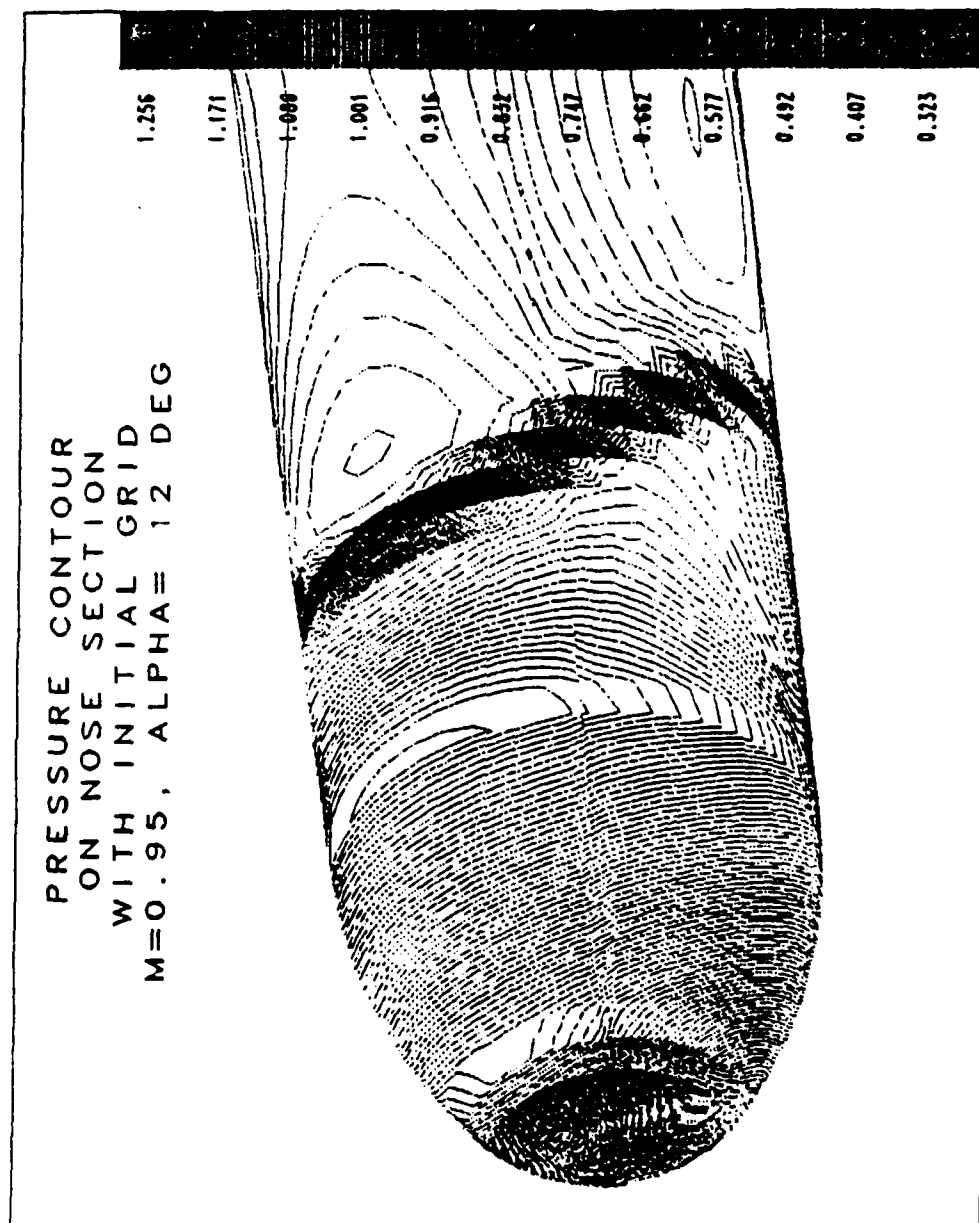


Figure 20. Pressure Contour on the Nose Surface with Initial Grid

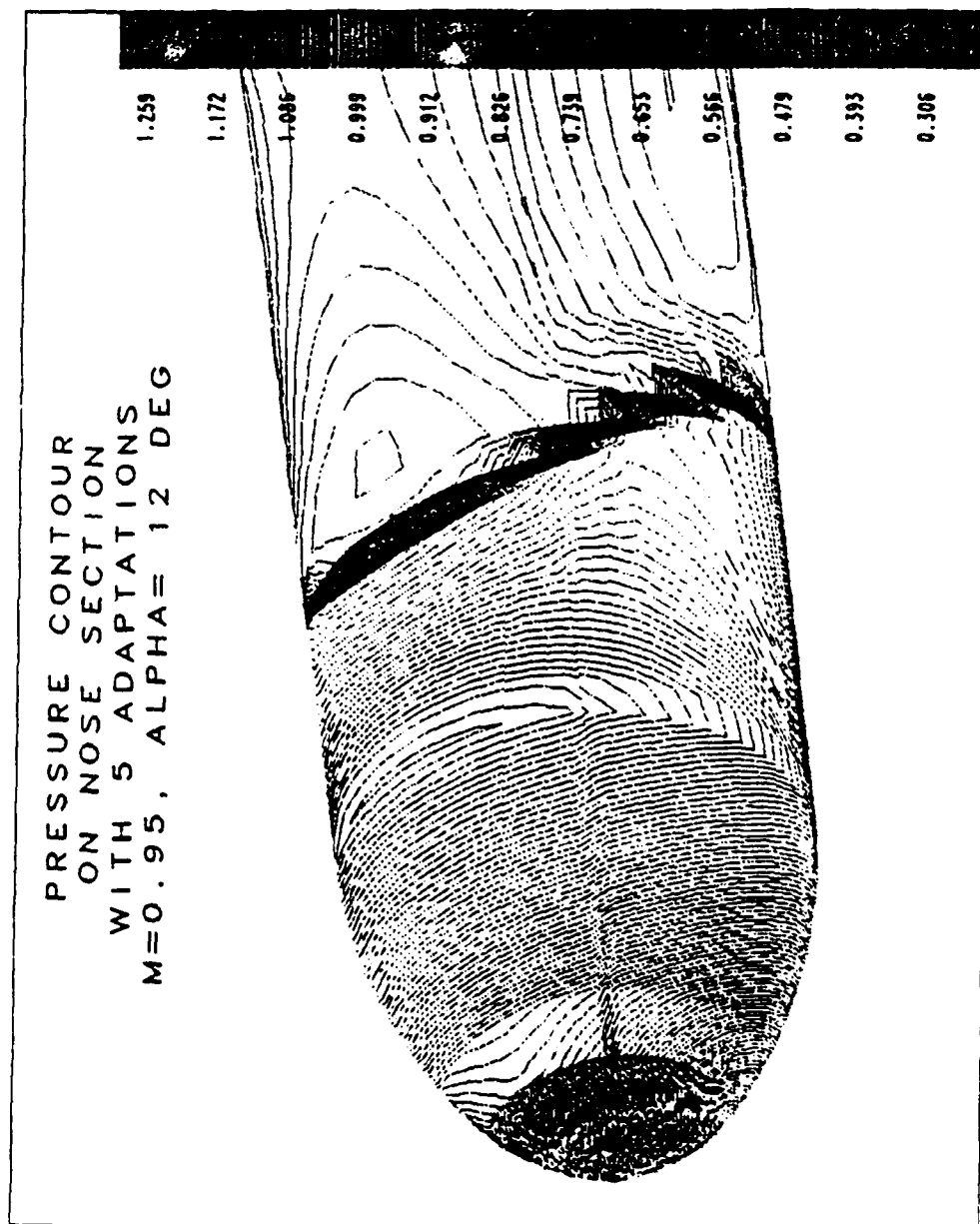


Figure 21. Pressure Contour on the Nose Surface with Five Adaptations

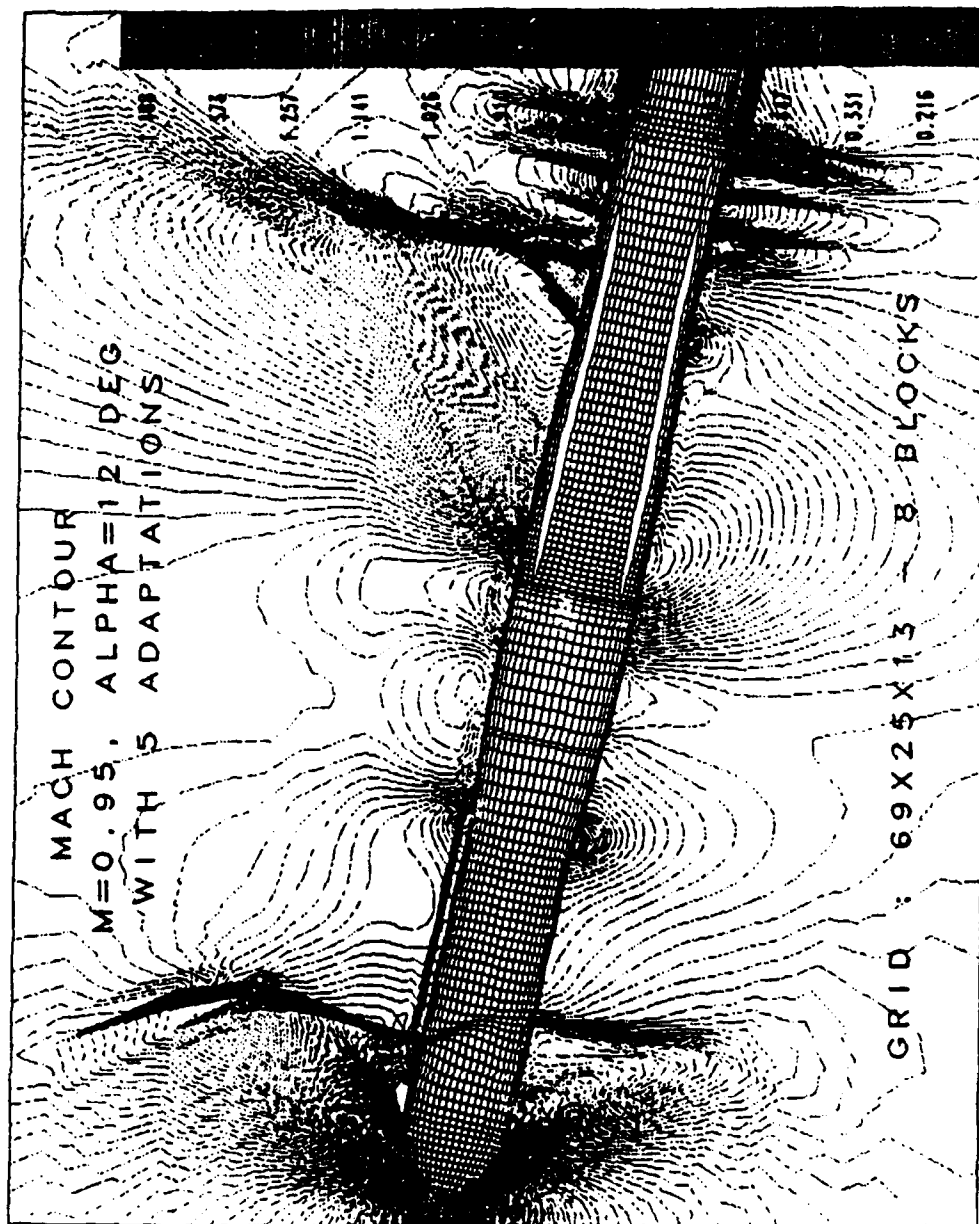


Figure 22. Mach Contours with Five Adaptations

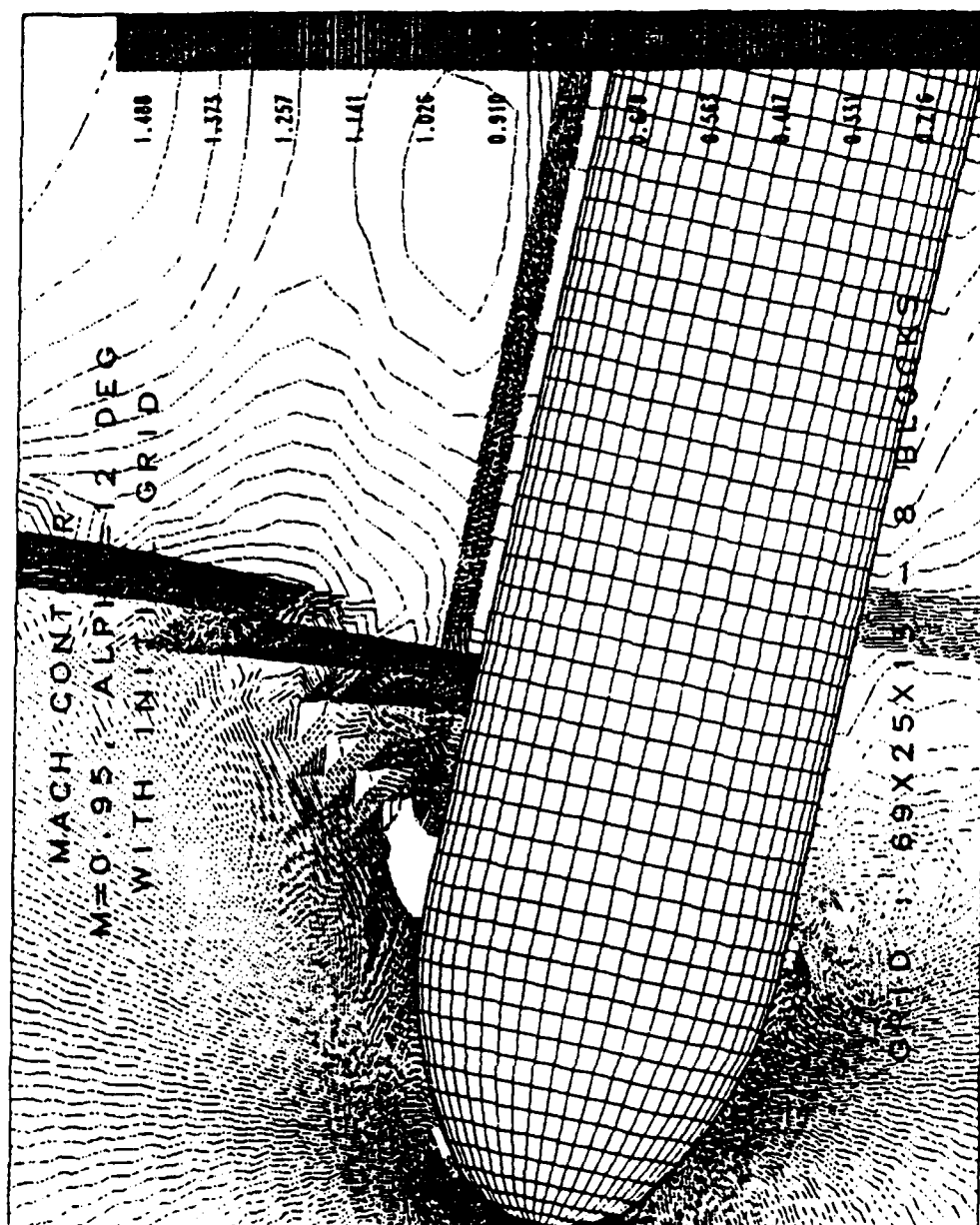


Figure 23. Shock with Initial Grid -- Mach Contour

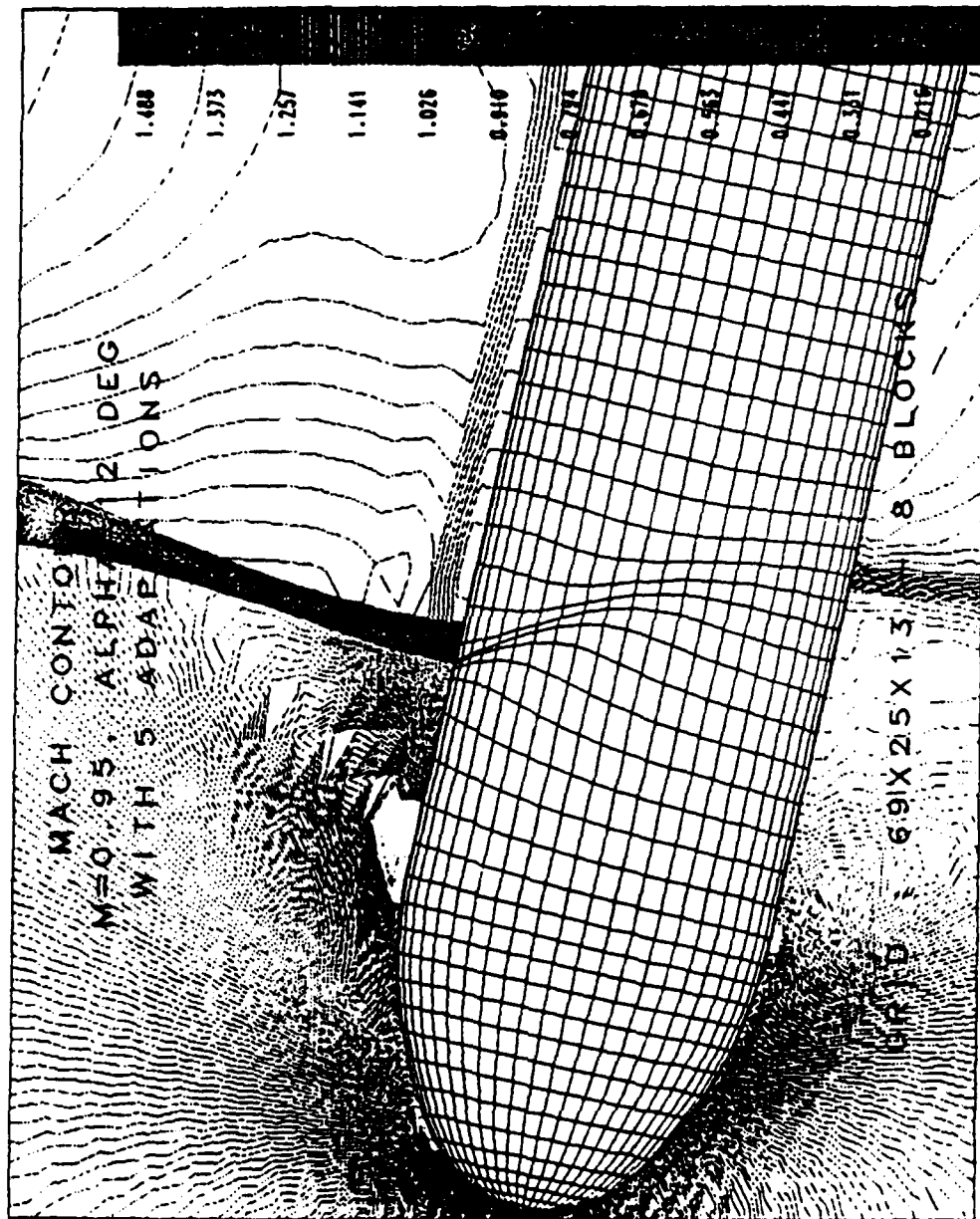


Figure 24. Shock with Five Adaptations - Mach Contour

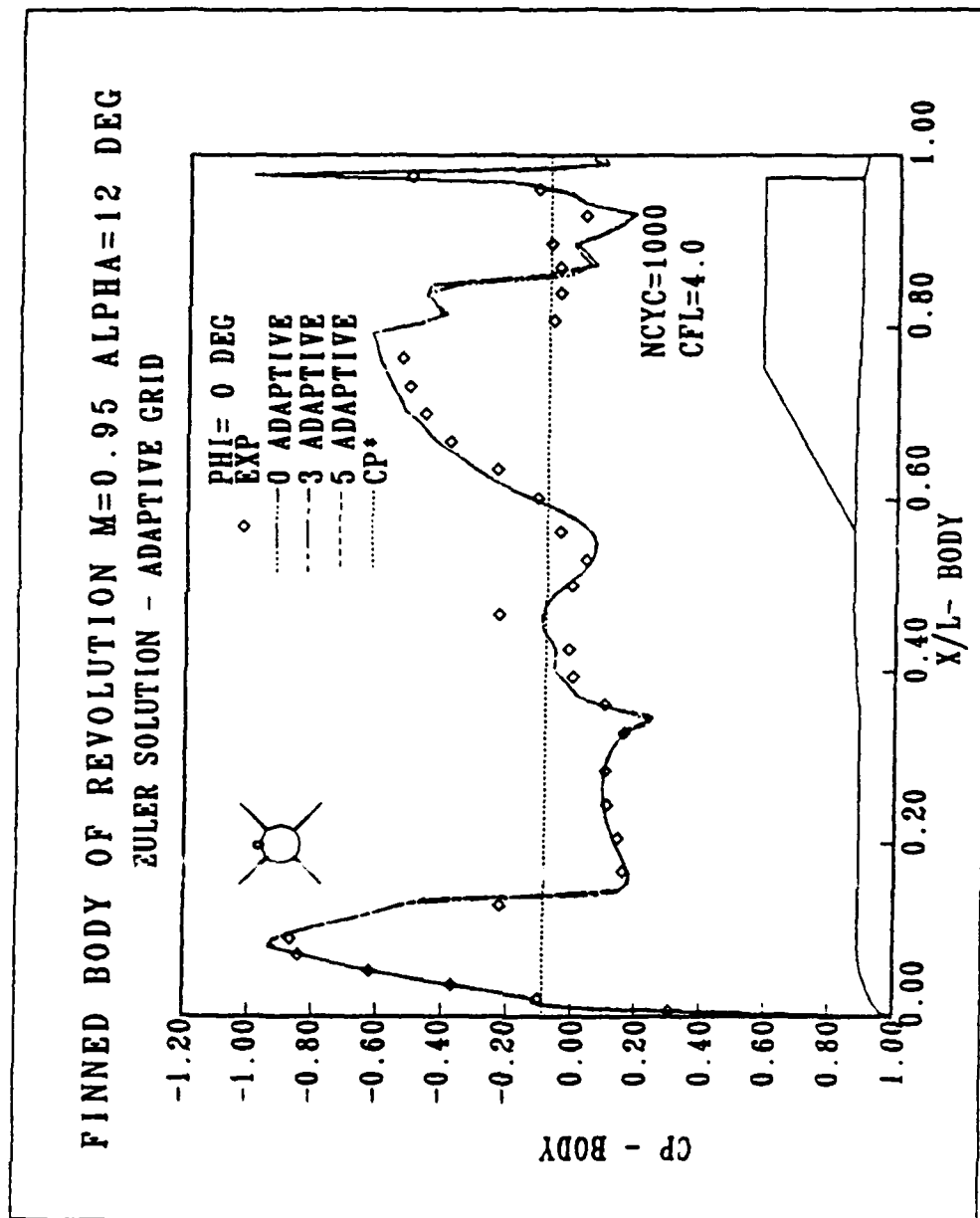


Figure 25. Pressure Distribution Along Body, $\Phi = 0^\circ$.

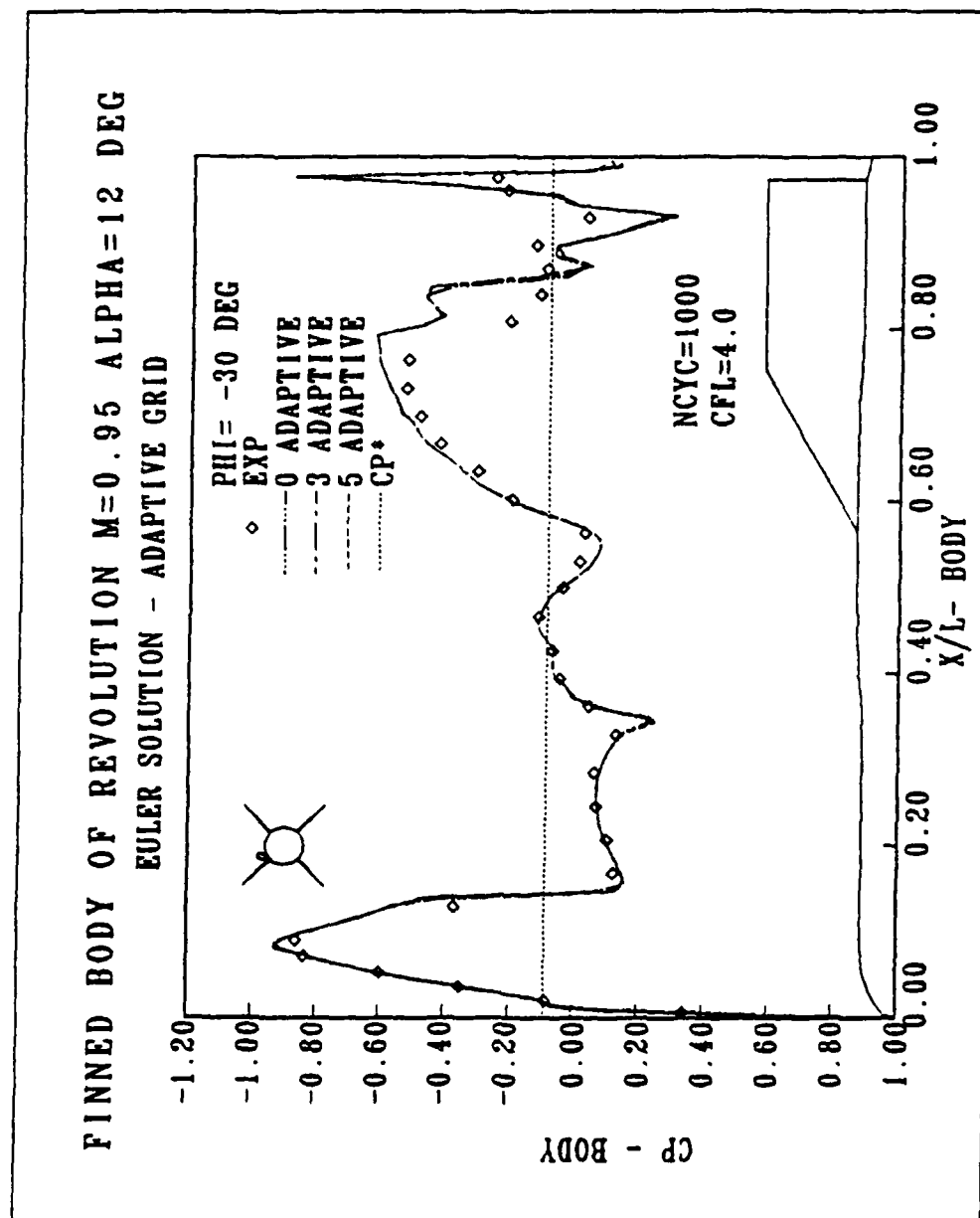


Figure 26. Pressure Distribution Along Body, $\Phi = -30$ Deg.

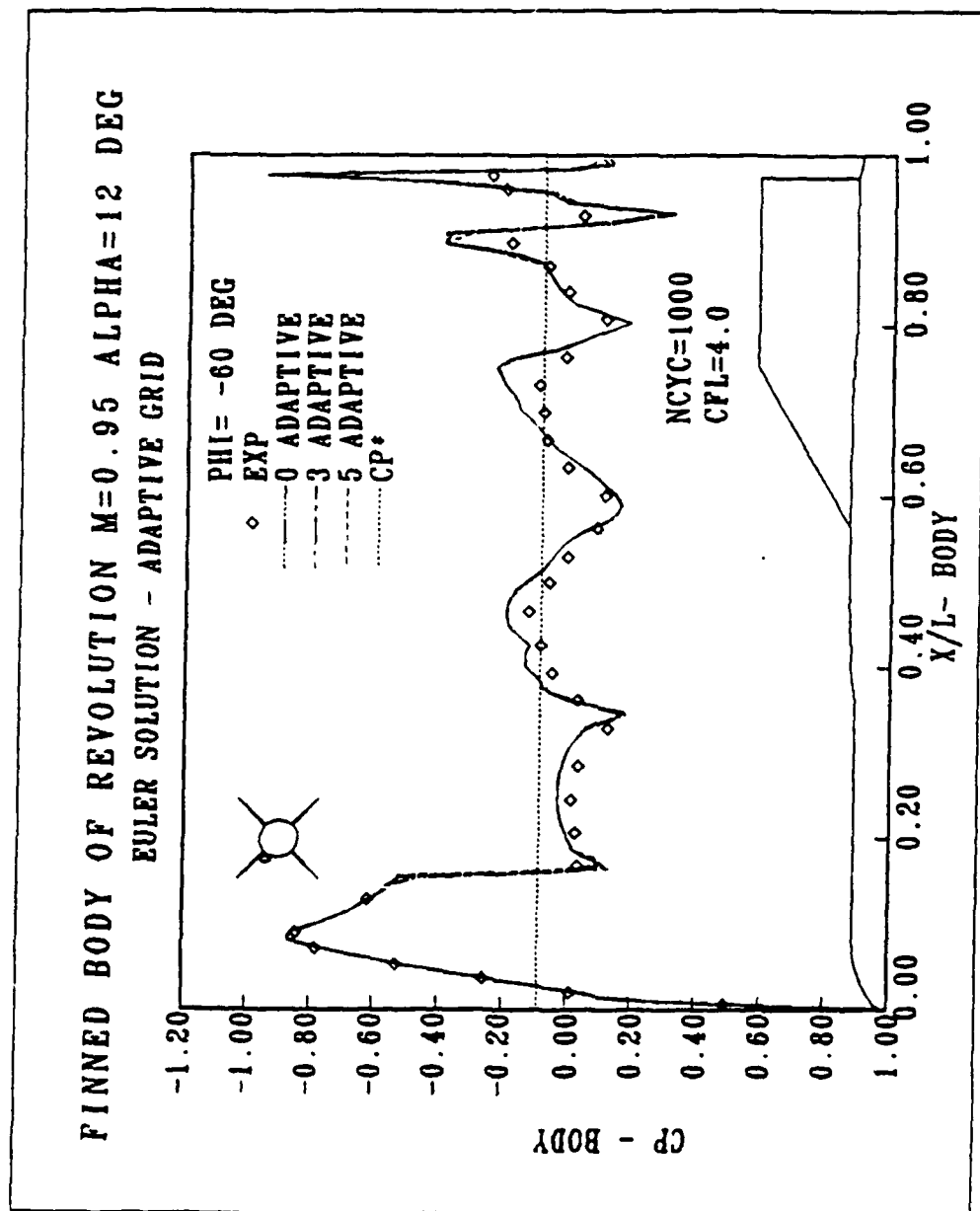


Figure 27. Pressure Distribution Along Body, $\phi = -60^\circ$.

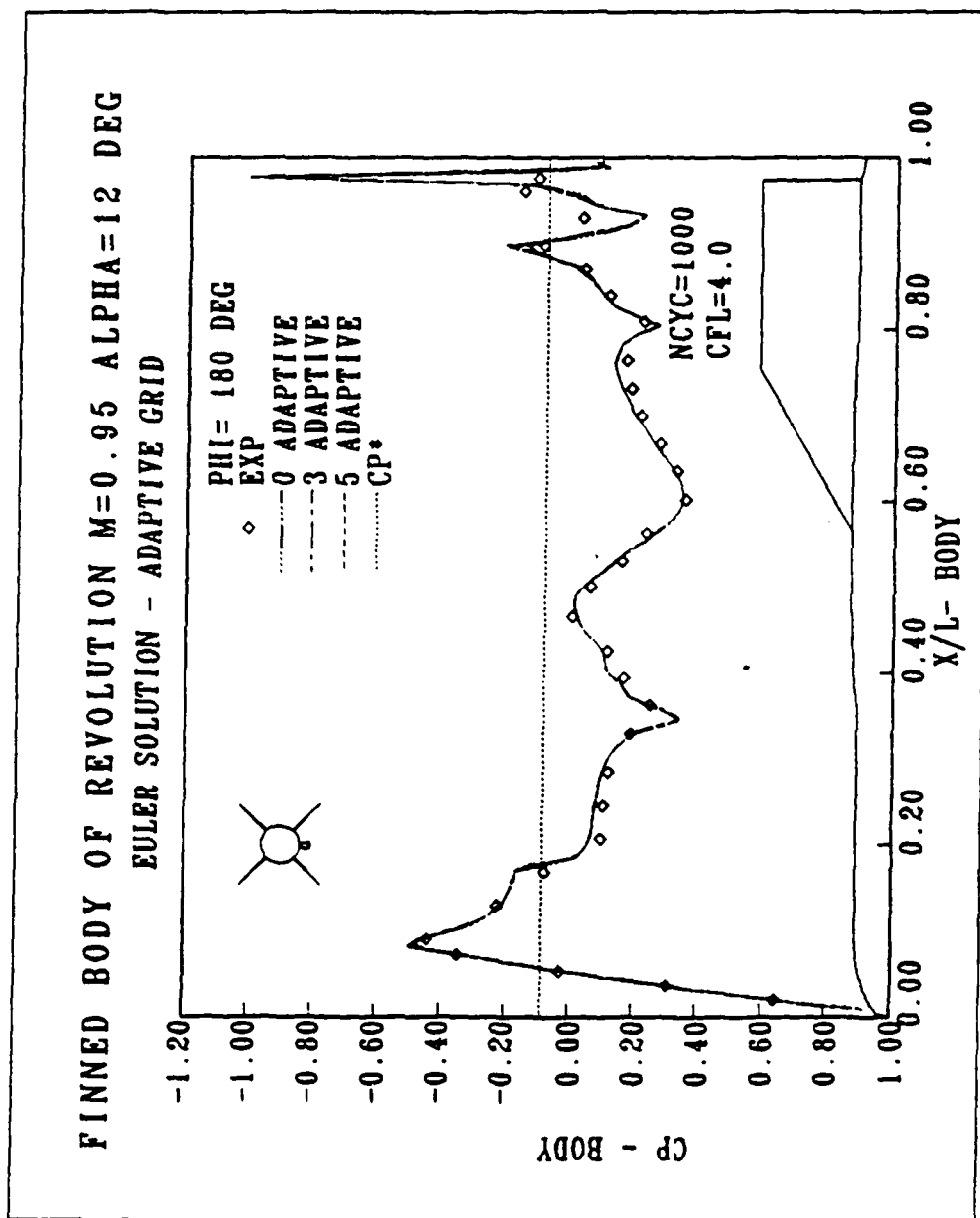


Figure 28. Pressure Distribution Along Body, $\Phi = 180^\circ$ Deg.

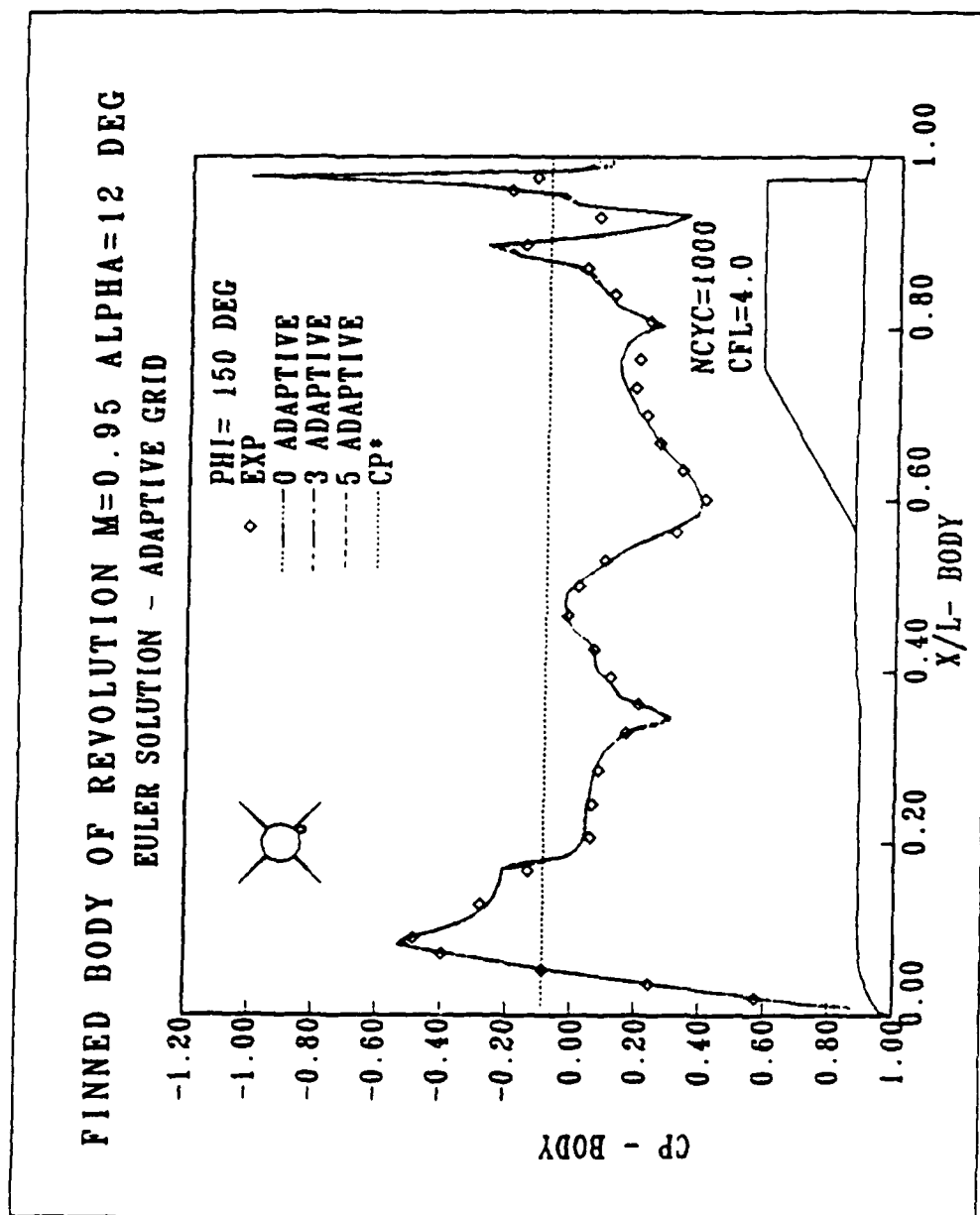


Figure 29. Pressure Distribution Along Body, $\Phi = 150$ Deg.

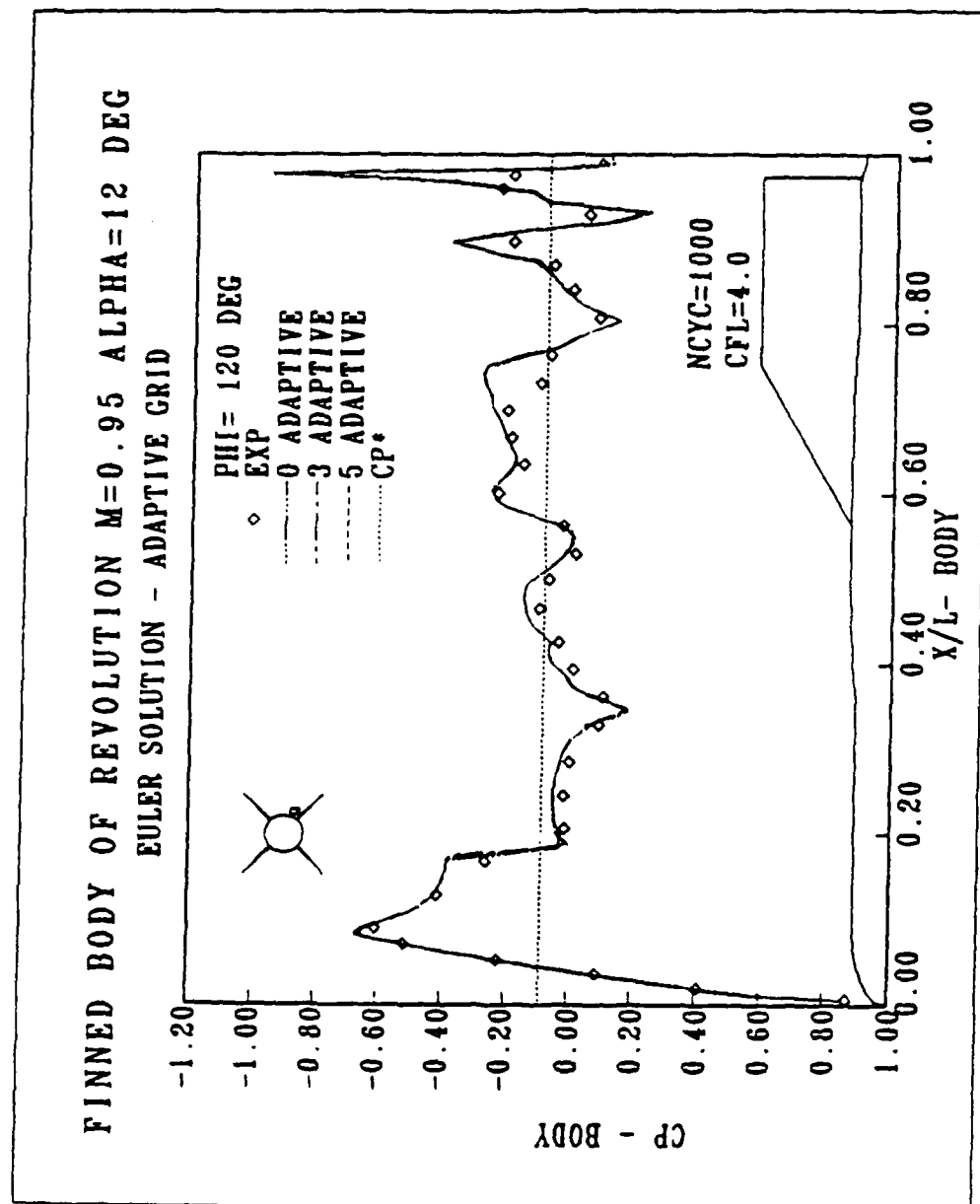


Figure 30. Pressure Distribution Along Body, $\Phi = 120$ Deg.

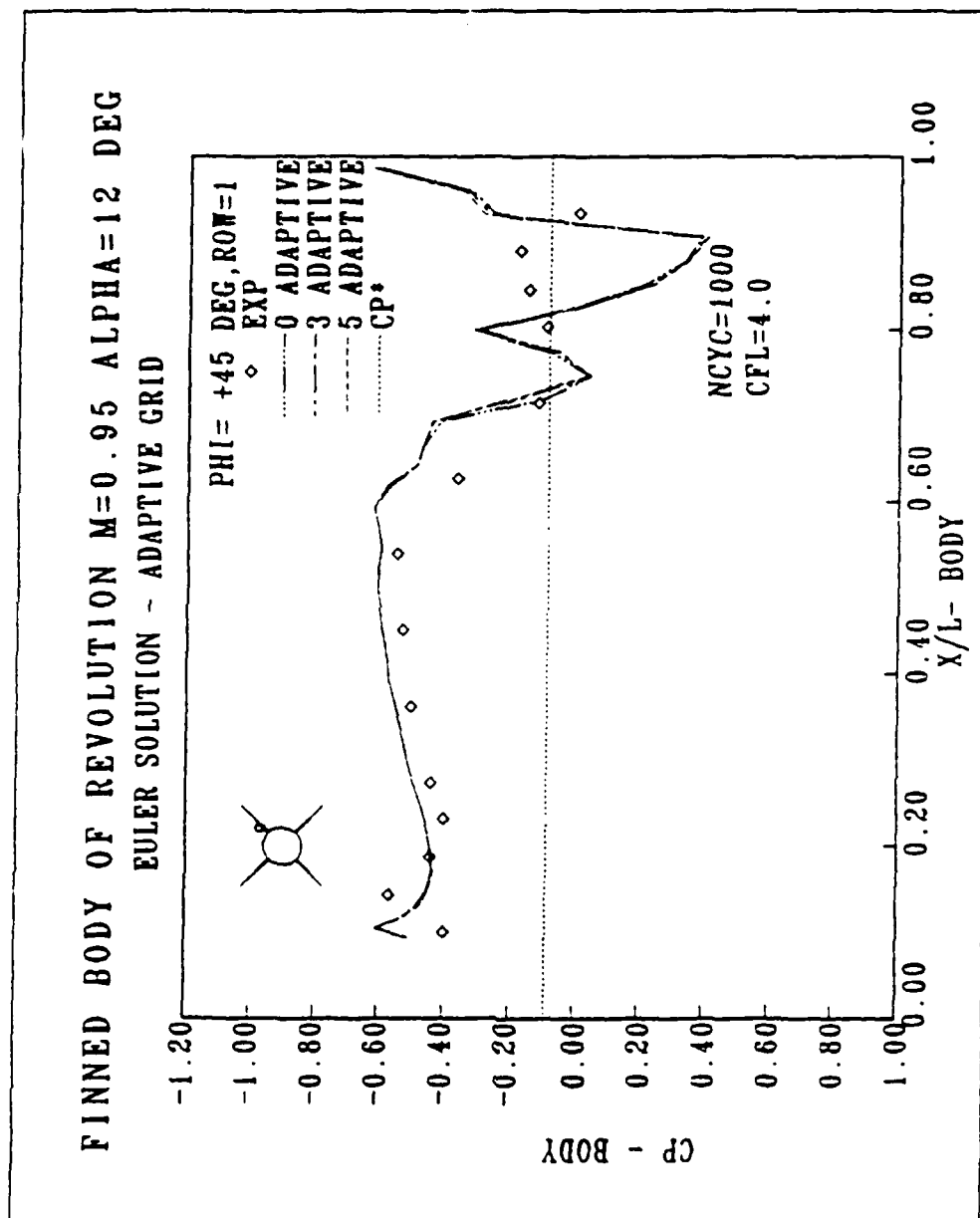


Figure 31. Pressure Distribution Along Fin, $\Phi = +45 \text{ Deg.}$, Row = 1

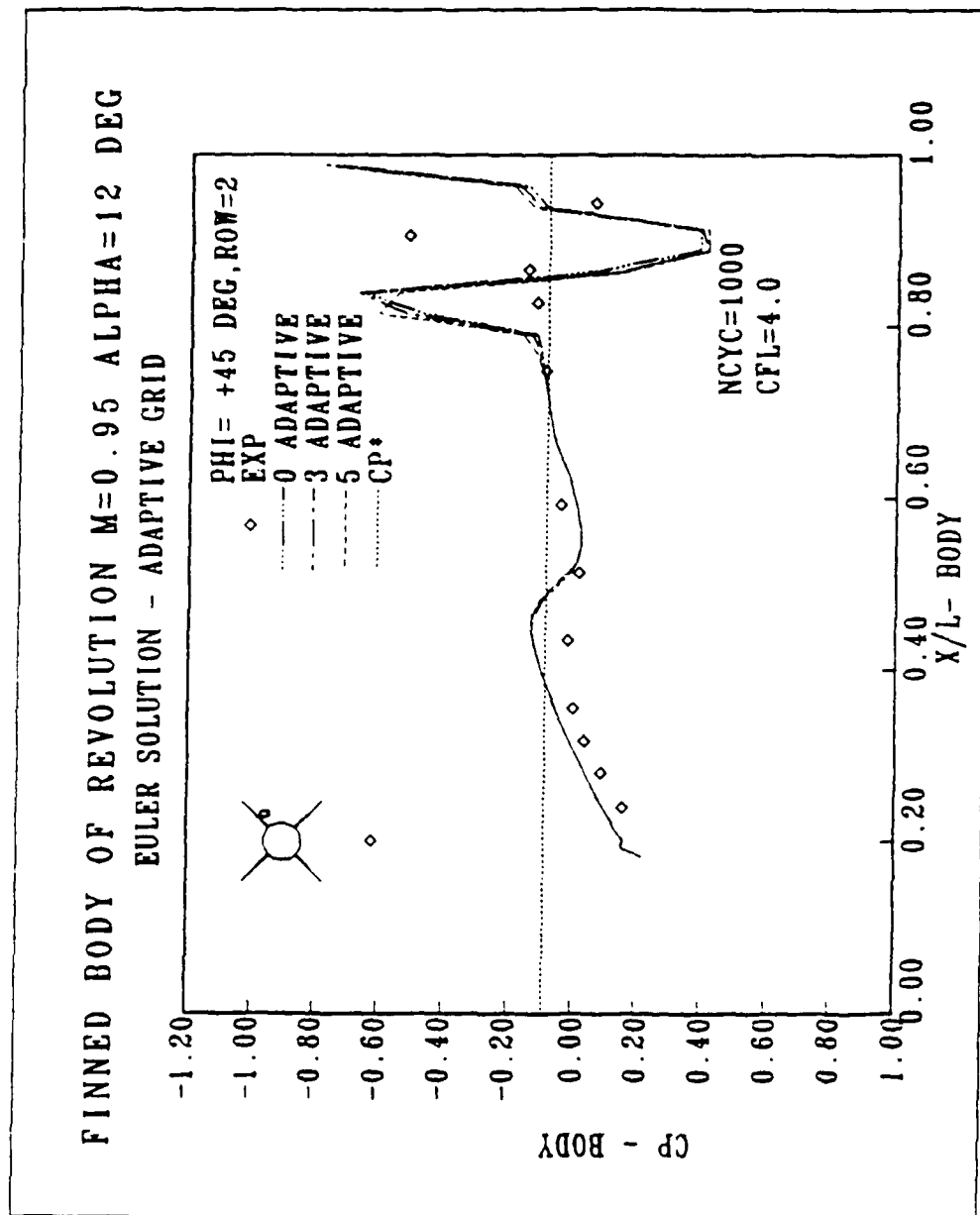


Figure 32. Pressure Distribution Along Fin, Phi = +45 Deg., Row = 2

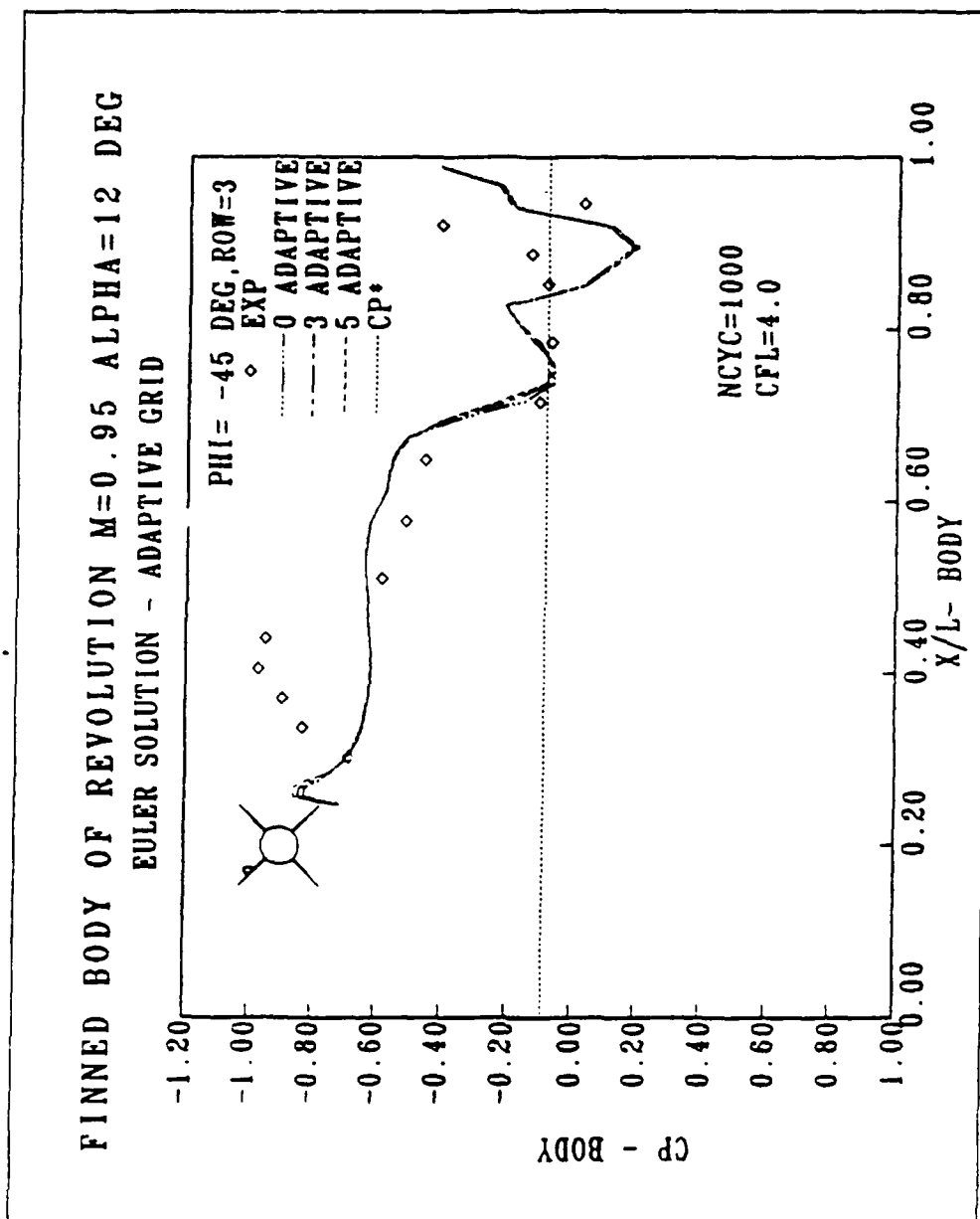


Figure 33. Pressure Distribution Along Fin, $\text{Phi} = -45$ Deg., Row = 3

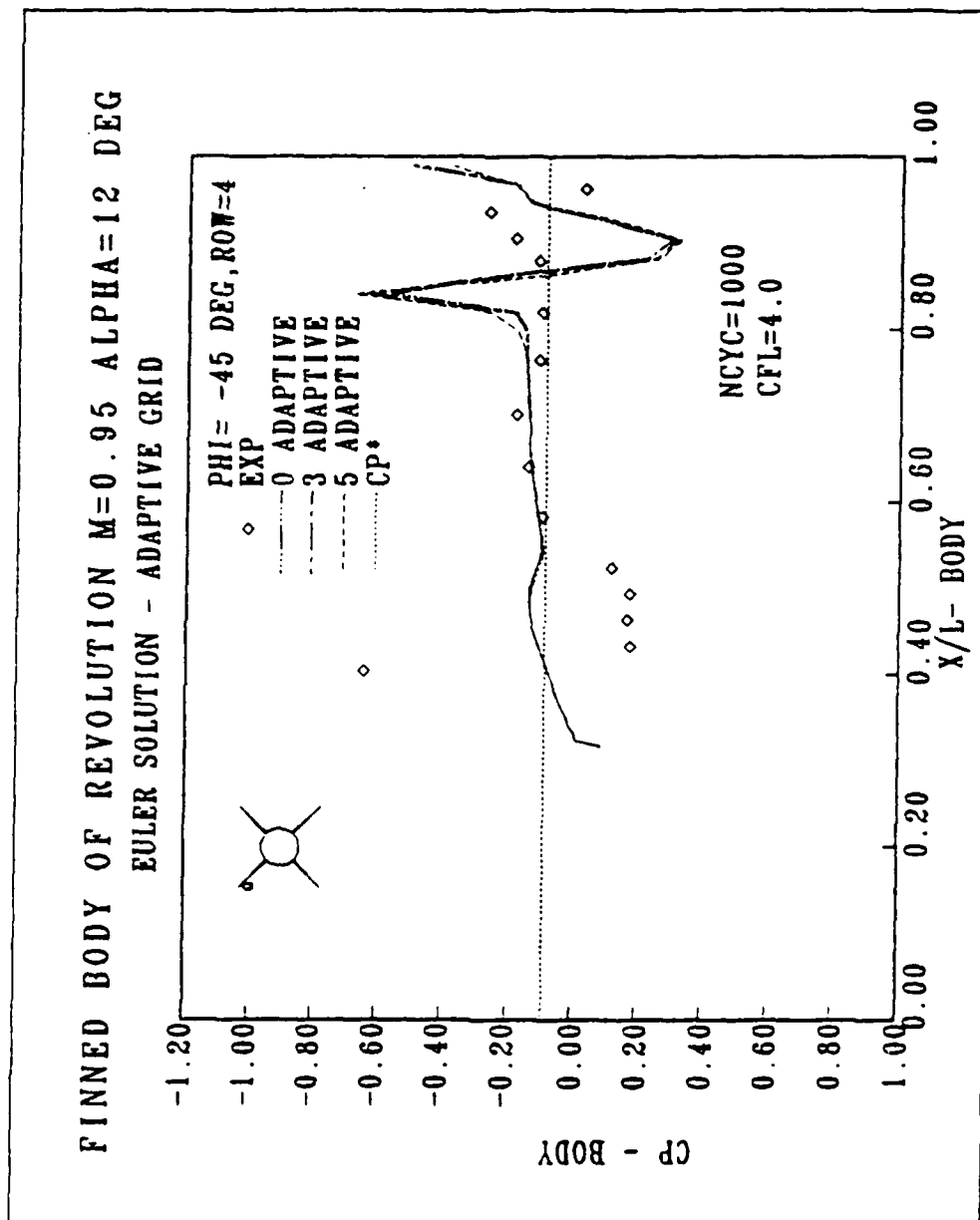


Figure 34. Pressure Distribution Along Fin, $\Phi = 45$ Deg., Row = 4

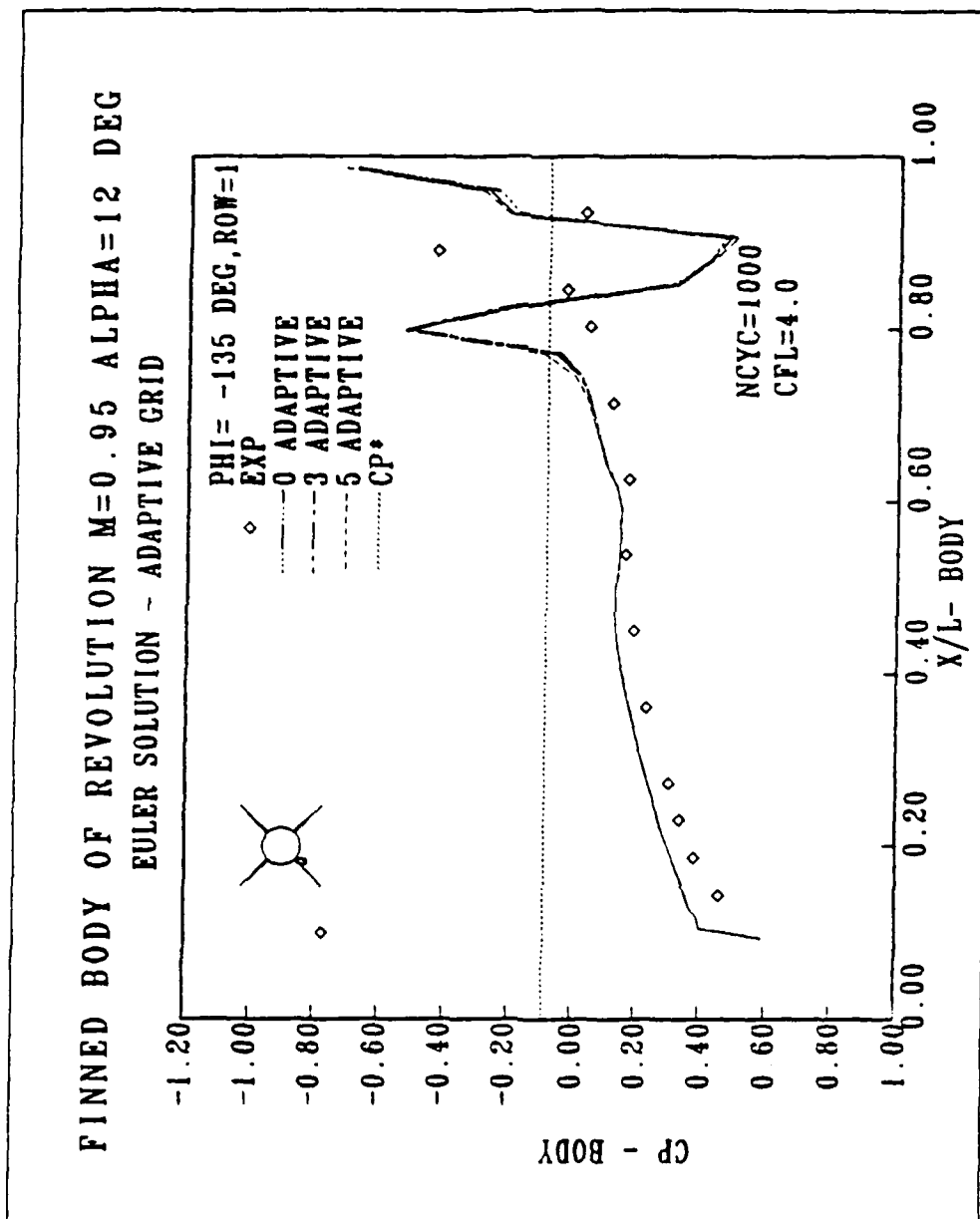


Figure 35. Pressure Distribution Along Fin, Phi = 135 Deg., Row = 1

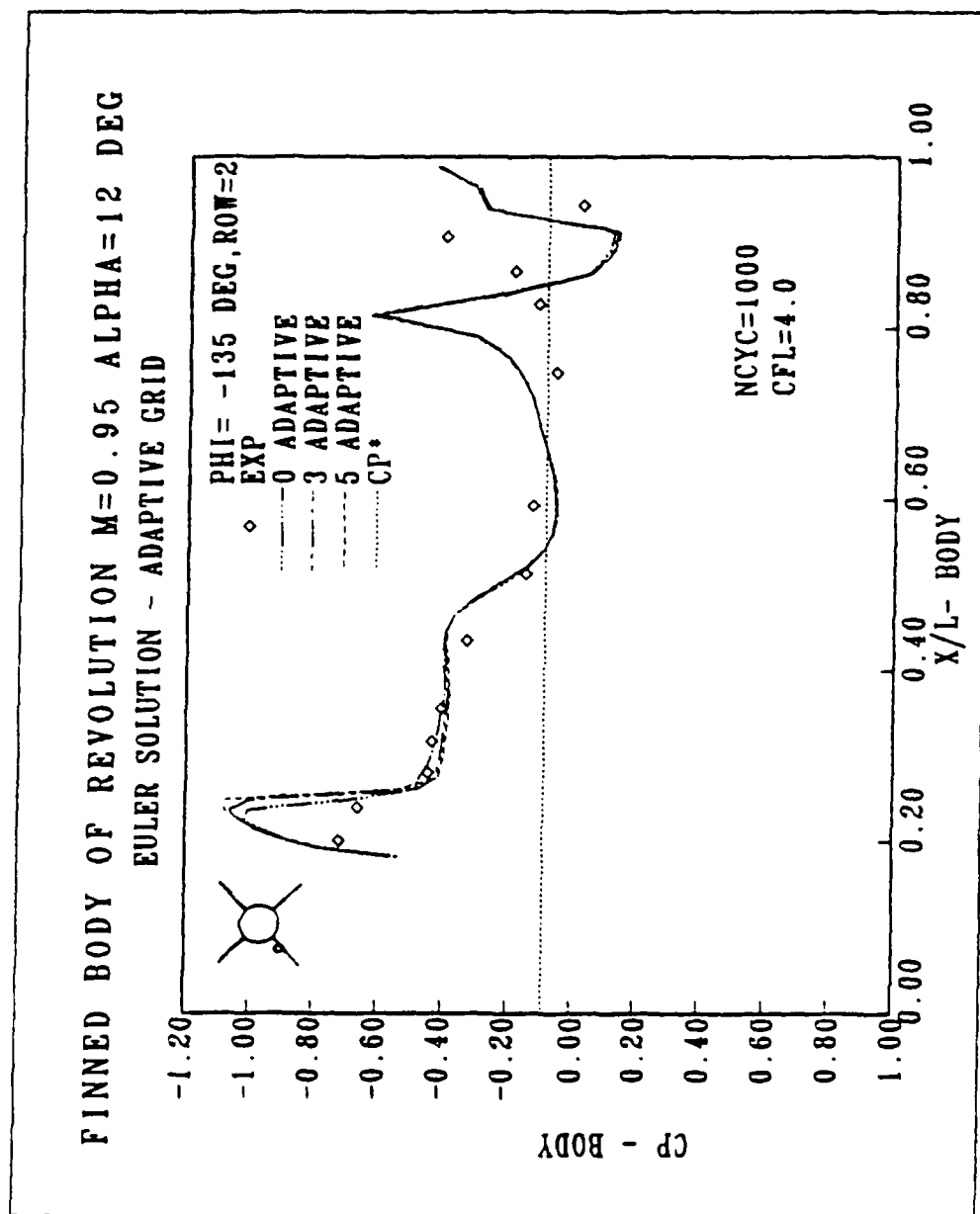


Figure 36. Pressure Distribution Along Fin, $\Phi = 135$ Deg., Row = 2

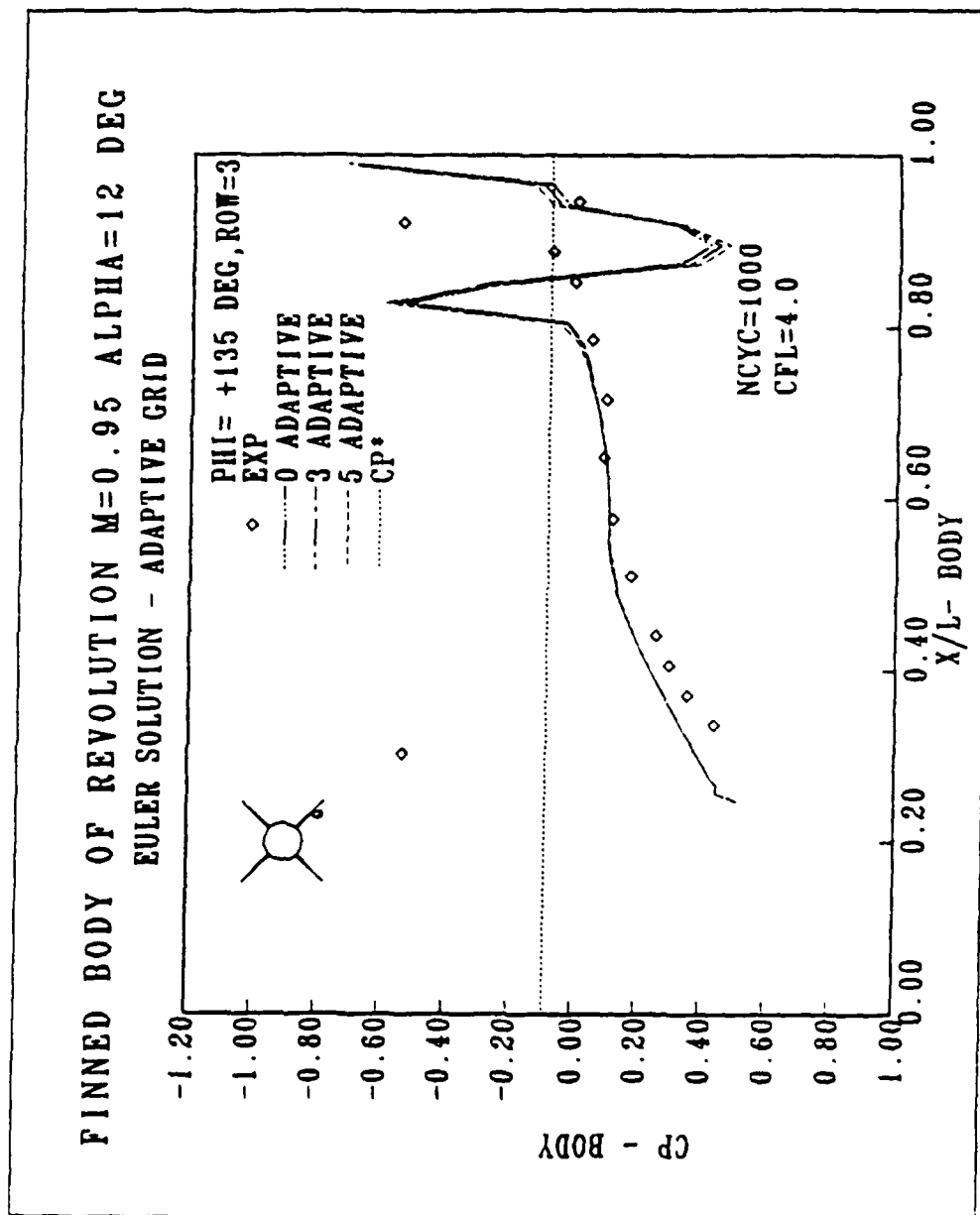


Figure 37. Pressure Distribution Along Fin, Phi = +135 Deg., Row = 3

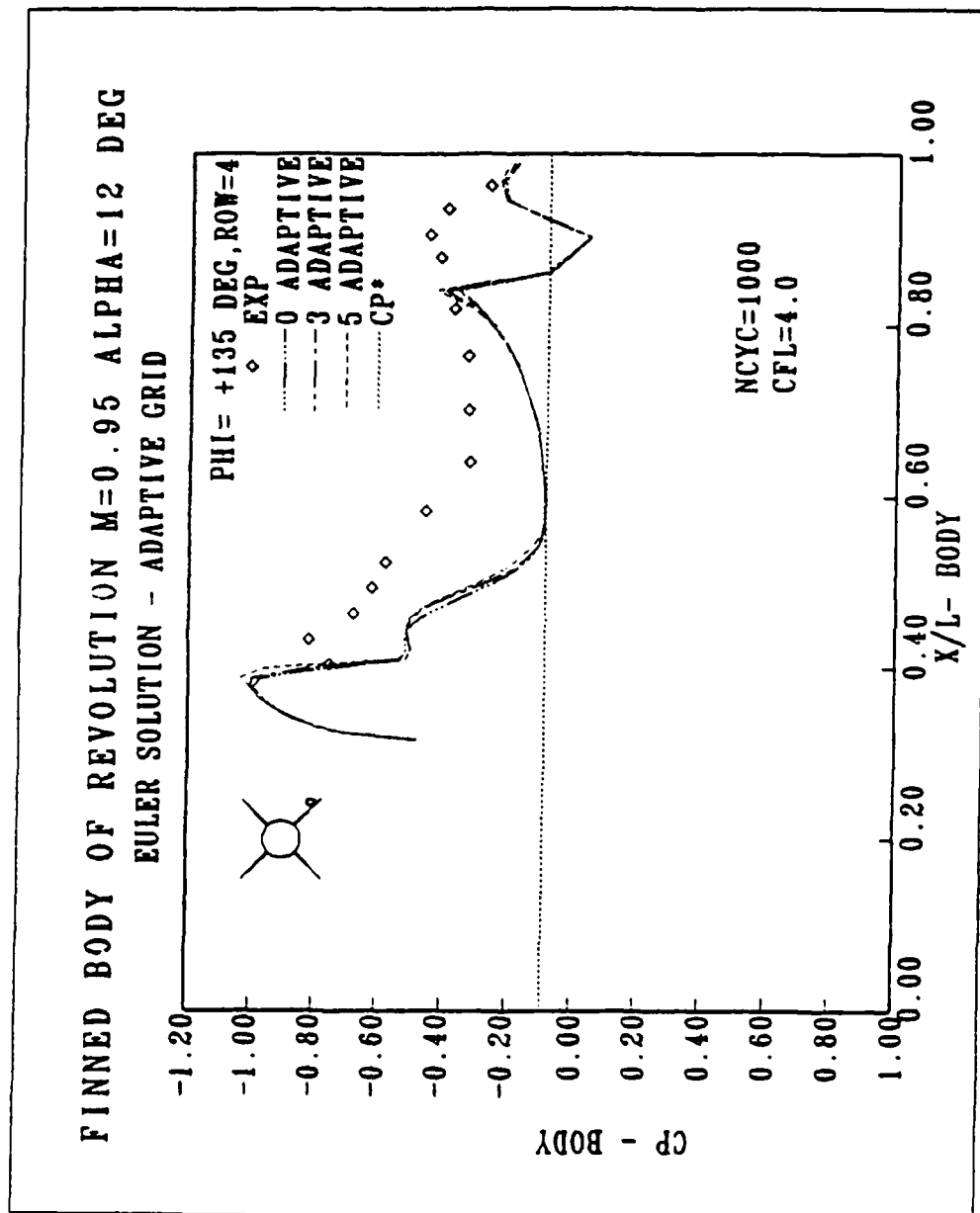


Figure 38. Pressure Distribution Along Fin, $\Phi = +135$ Deg., Row = 4

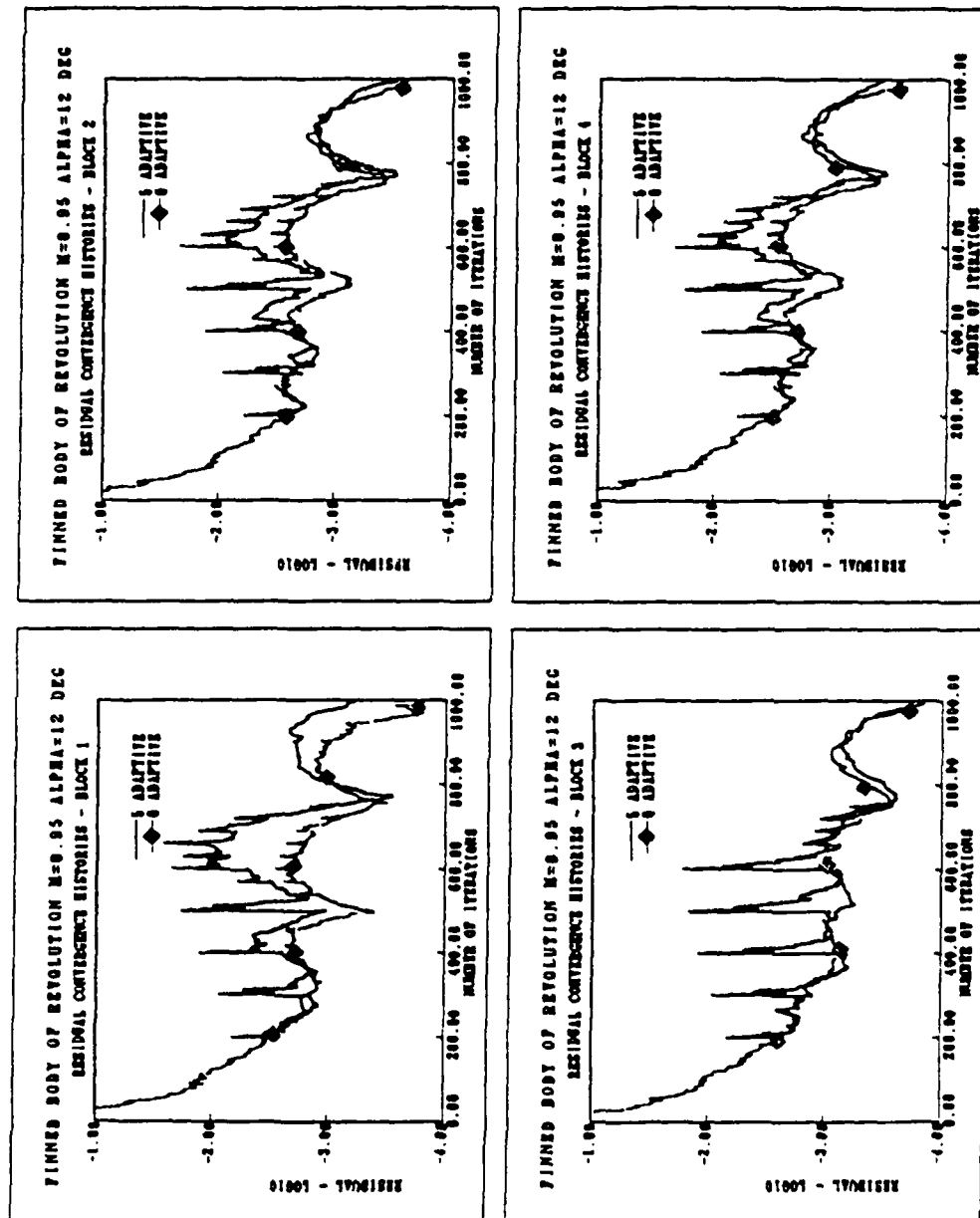


Figure 39. Residual Convergence Histories, Blocks One through Four

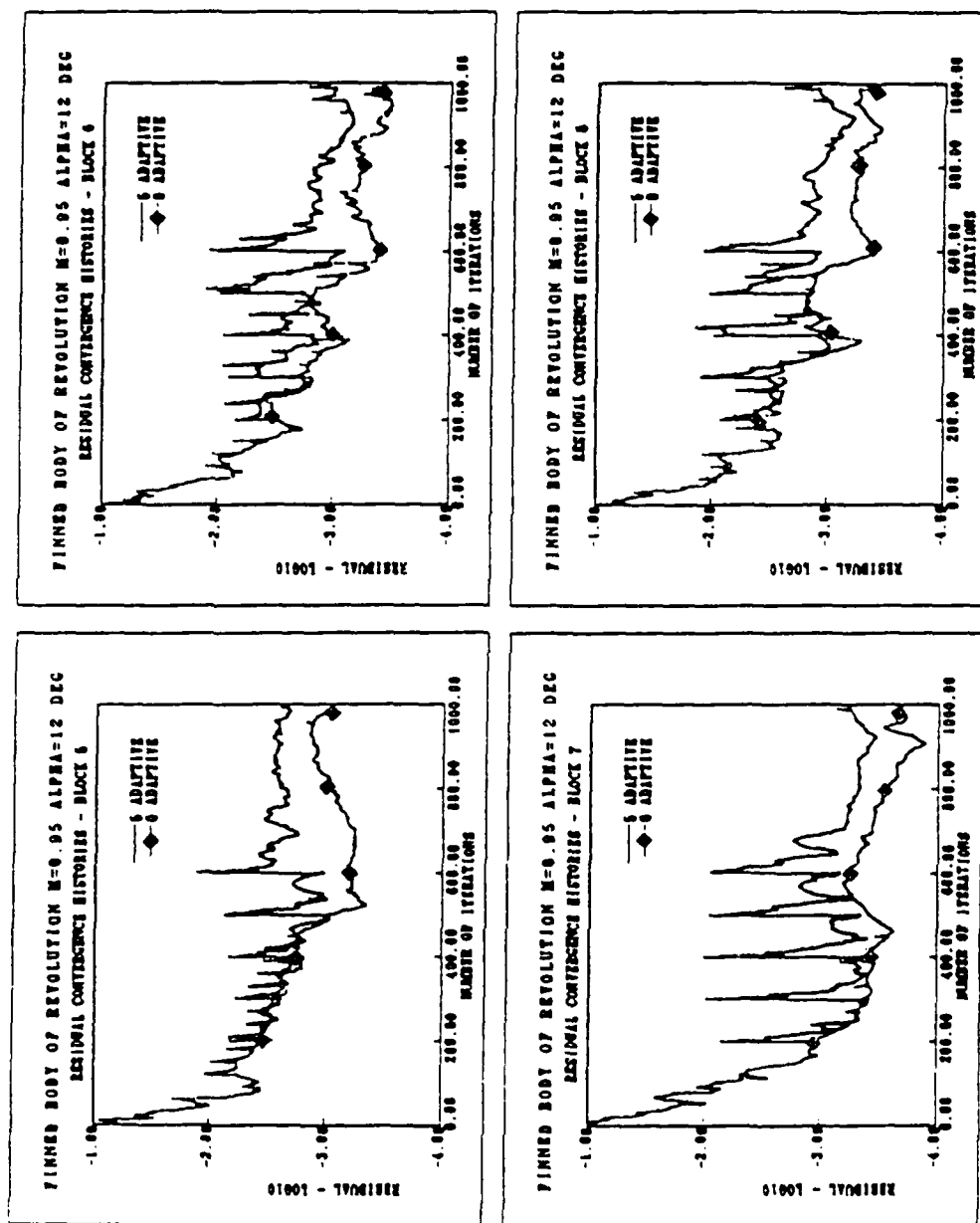


Figure 40. Residual Convergence Histories, Blocks Five through Eight

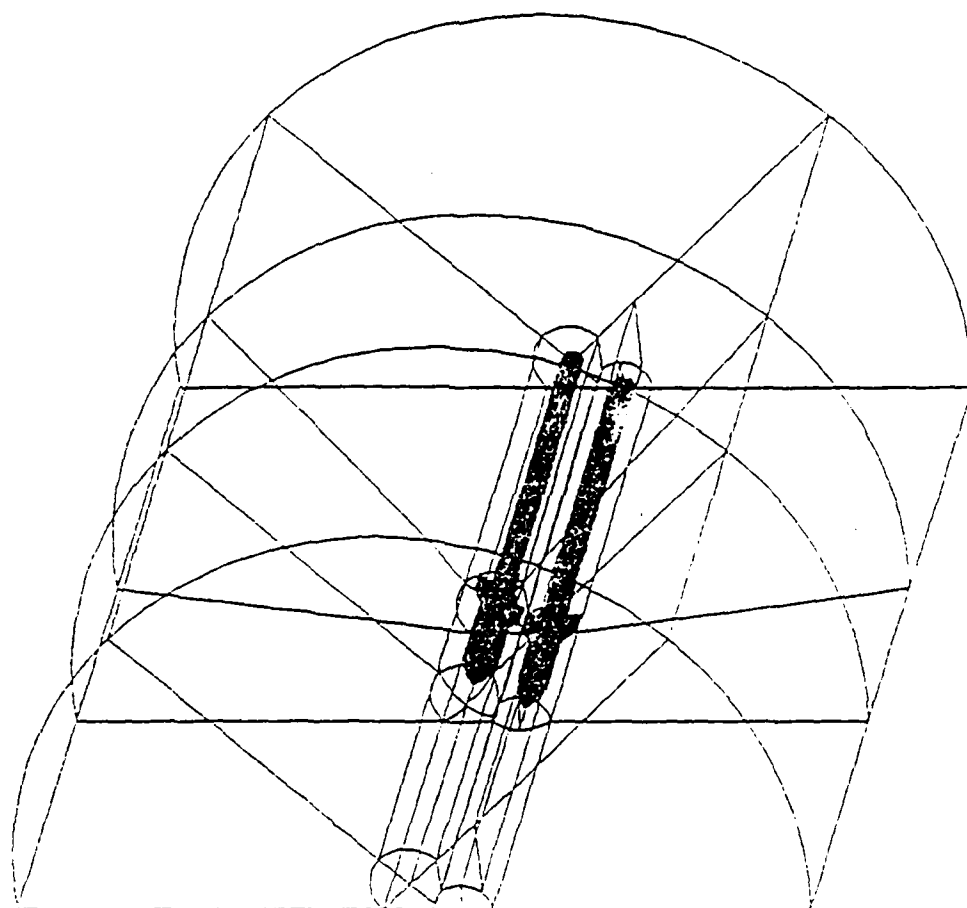


Figure 41. Perspective View of the Structure of Thirty Blocks

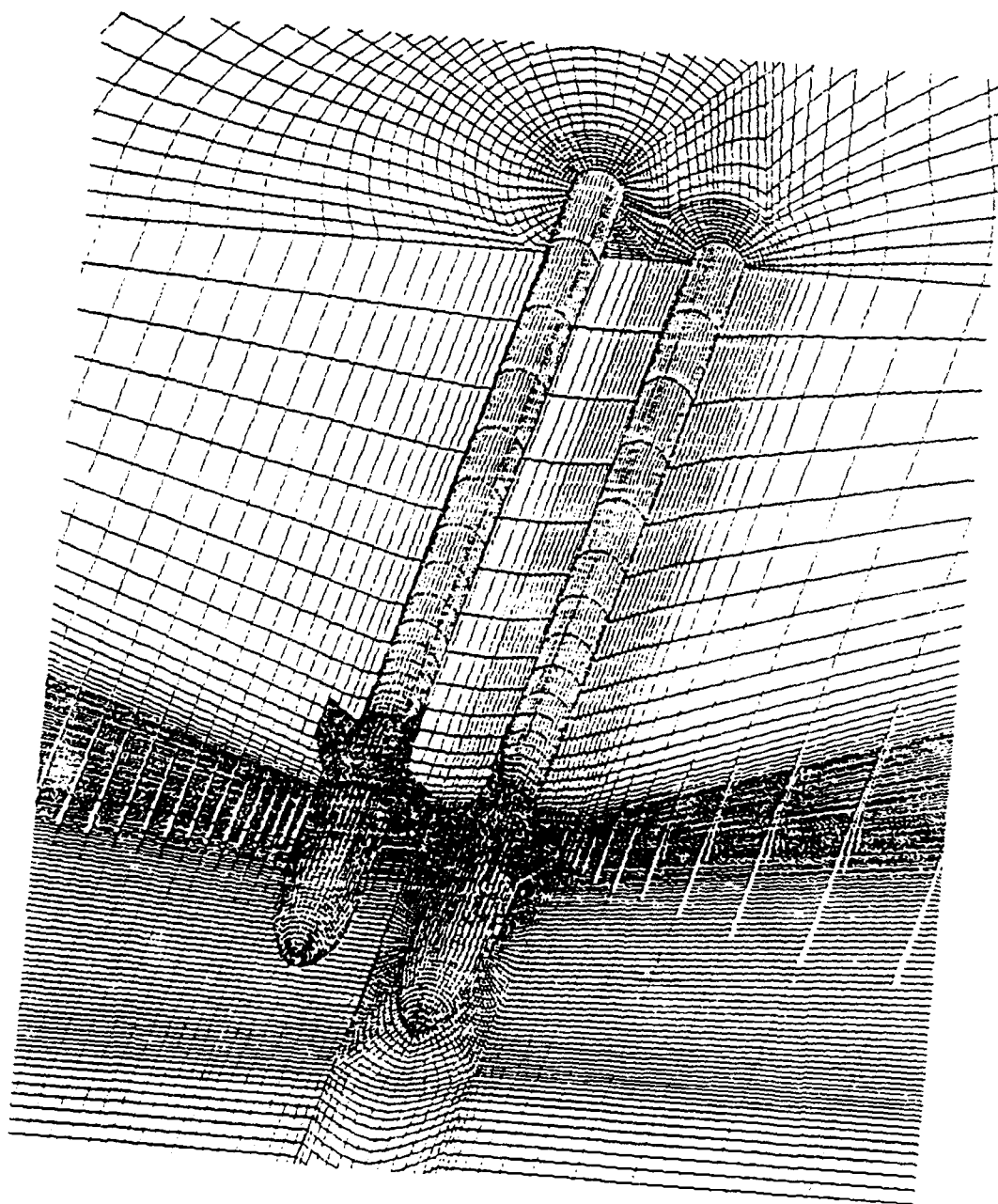


Figure 42. Perspective View of Thirty-Block Grid System

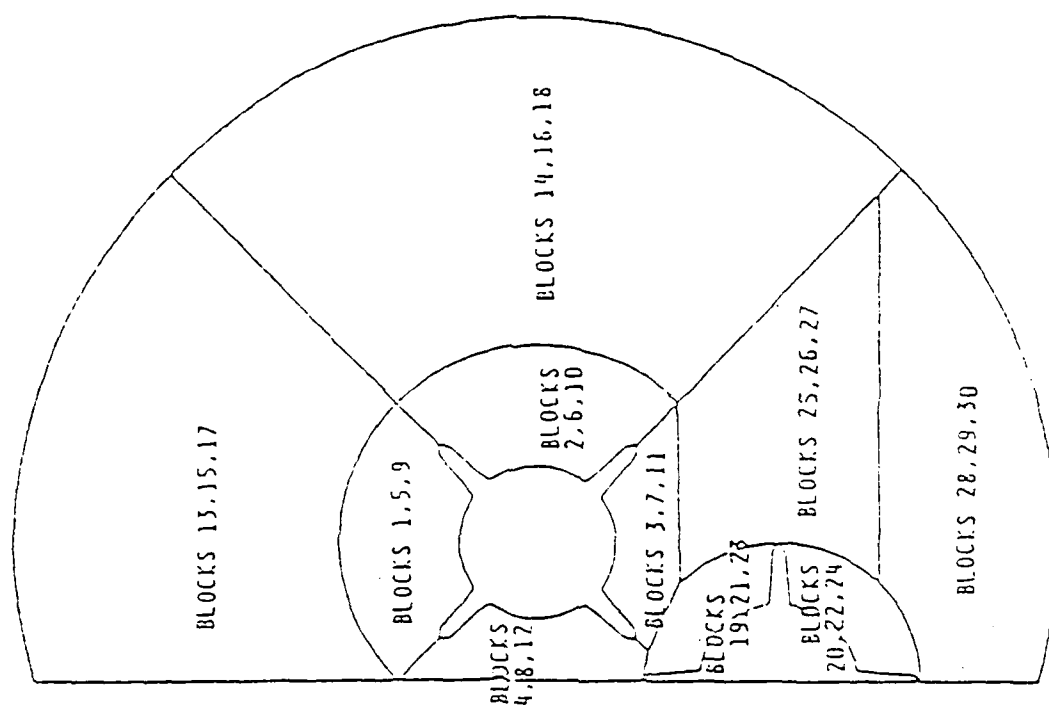


Figure 43. Cross Sectional View of the Structure of Thirty Blocks

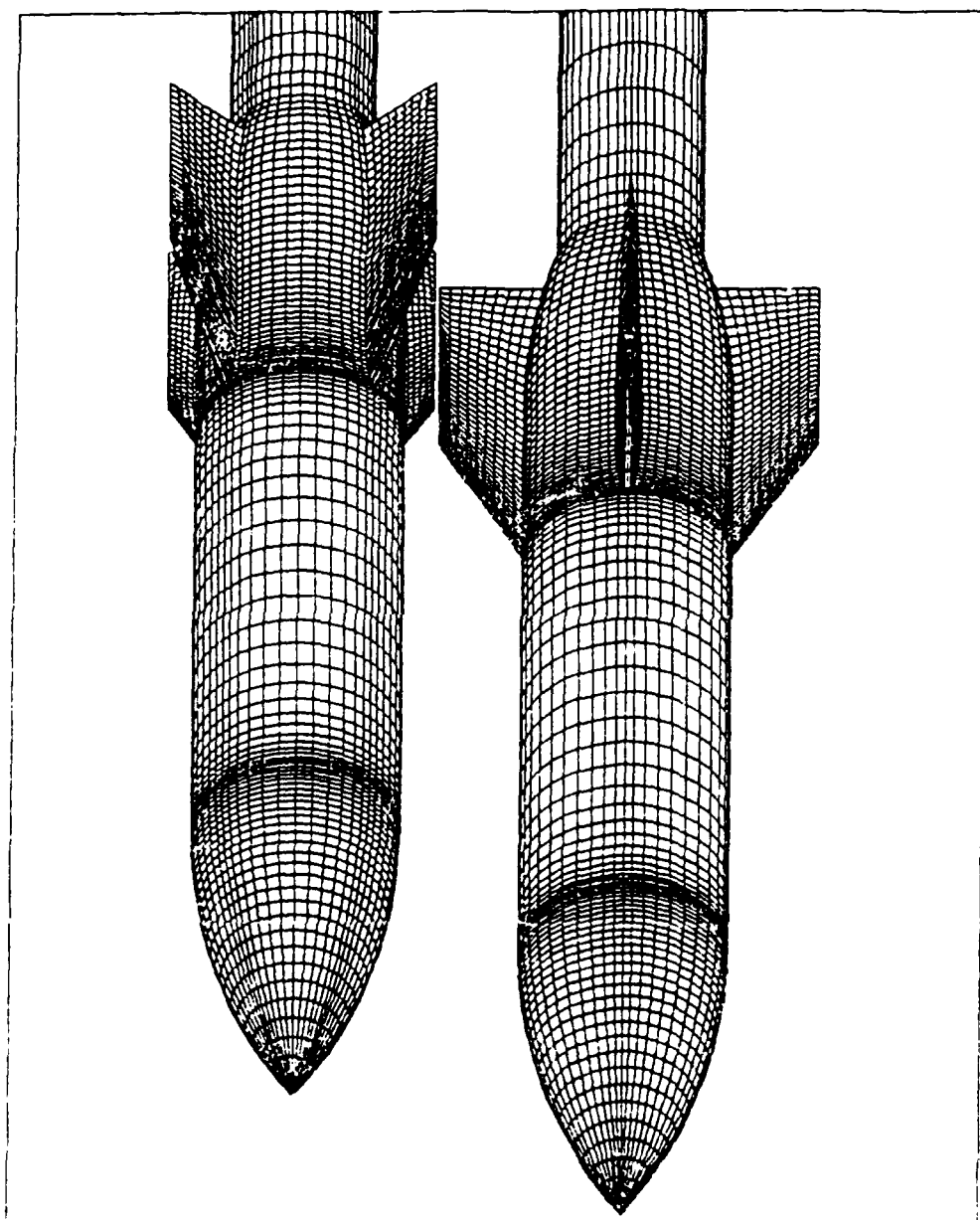


Figure 44. Multiple Store Configuration

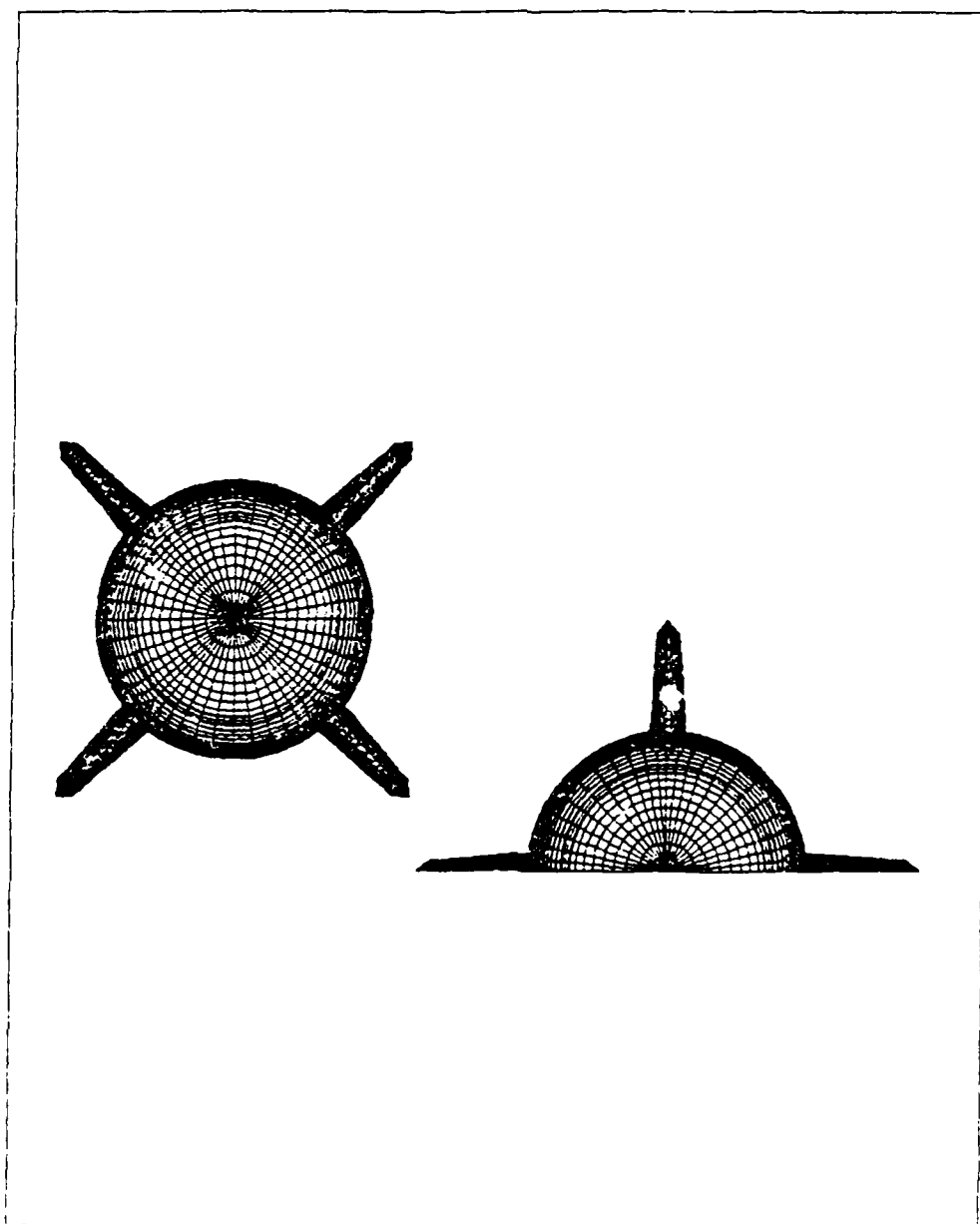


Figure 45. Frontal View of Multiple Store Configuration

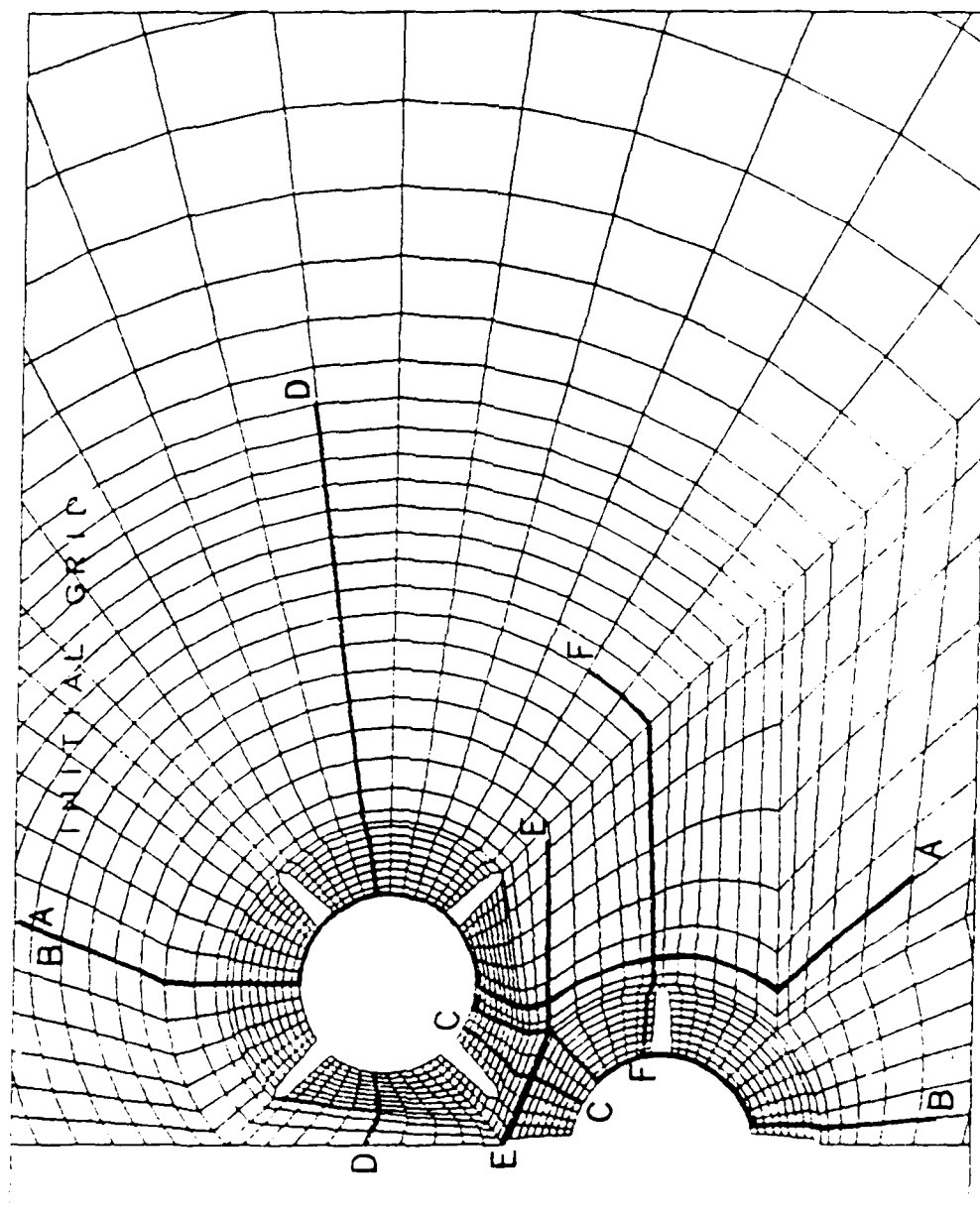


Figure 46. Cross Sectional View of Multiple Store Configuration

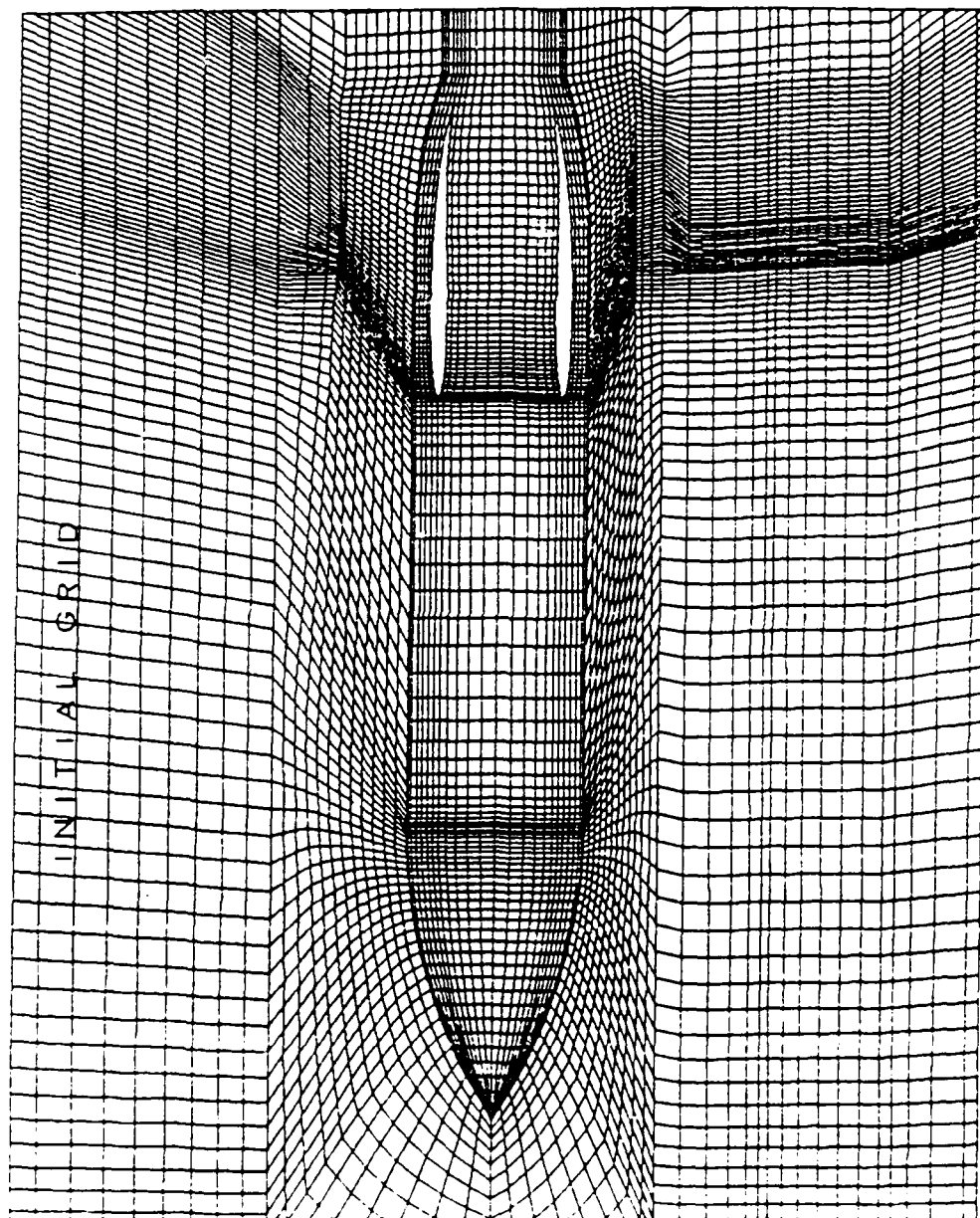
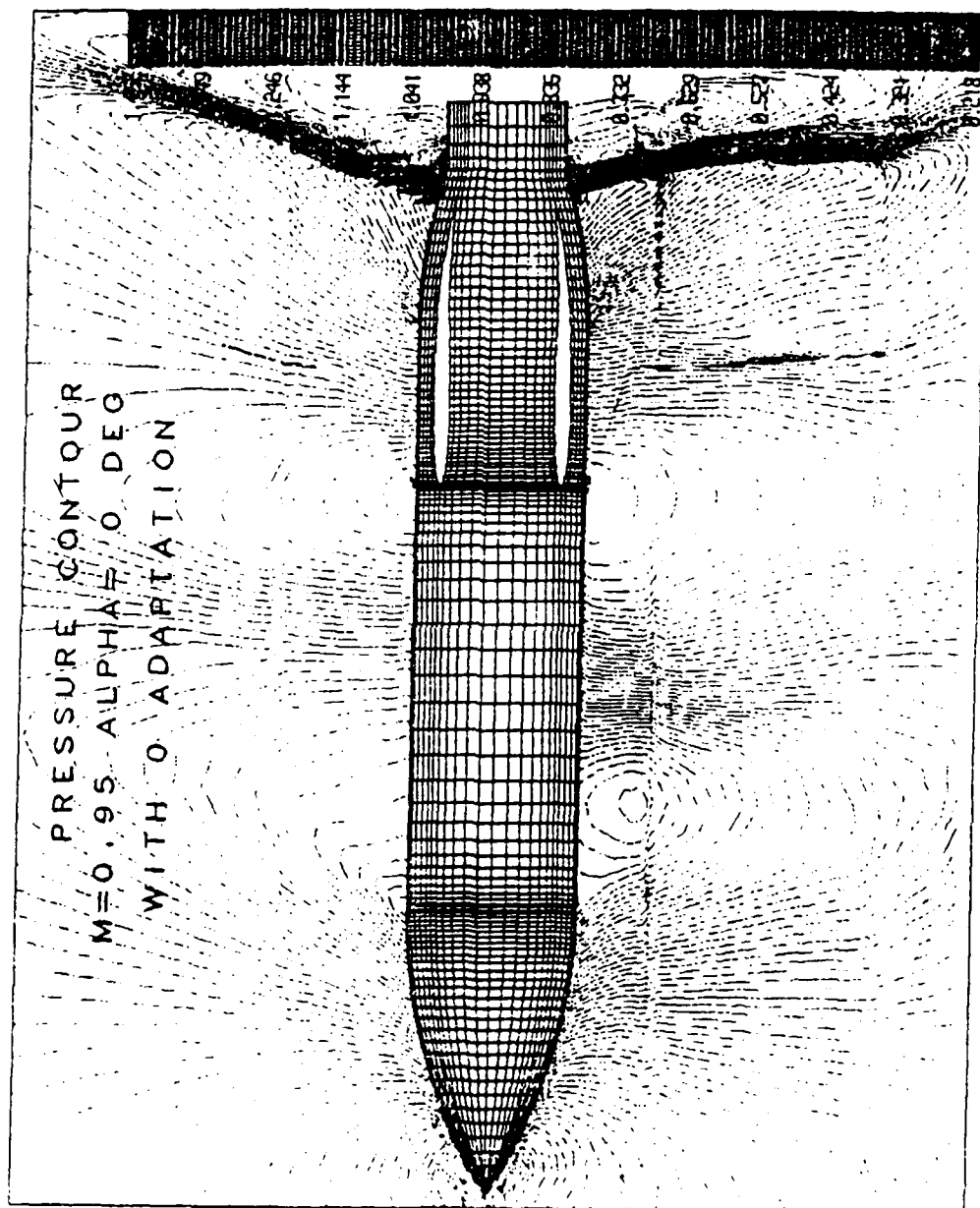


Figure 47. Initial Grid, Section A-A



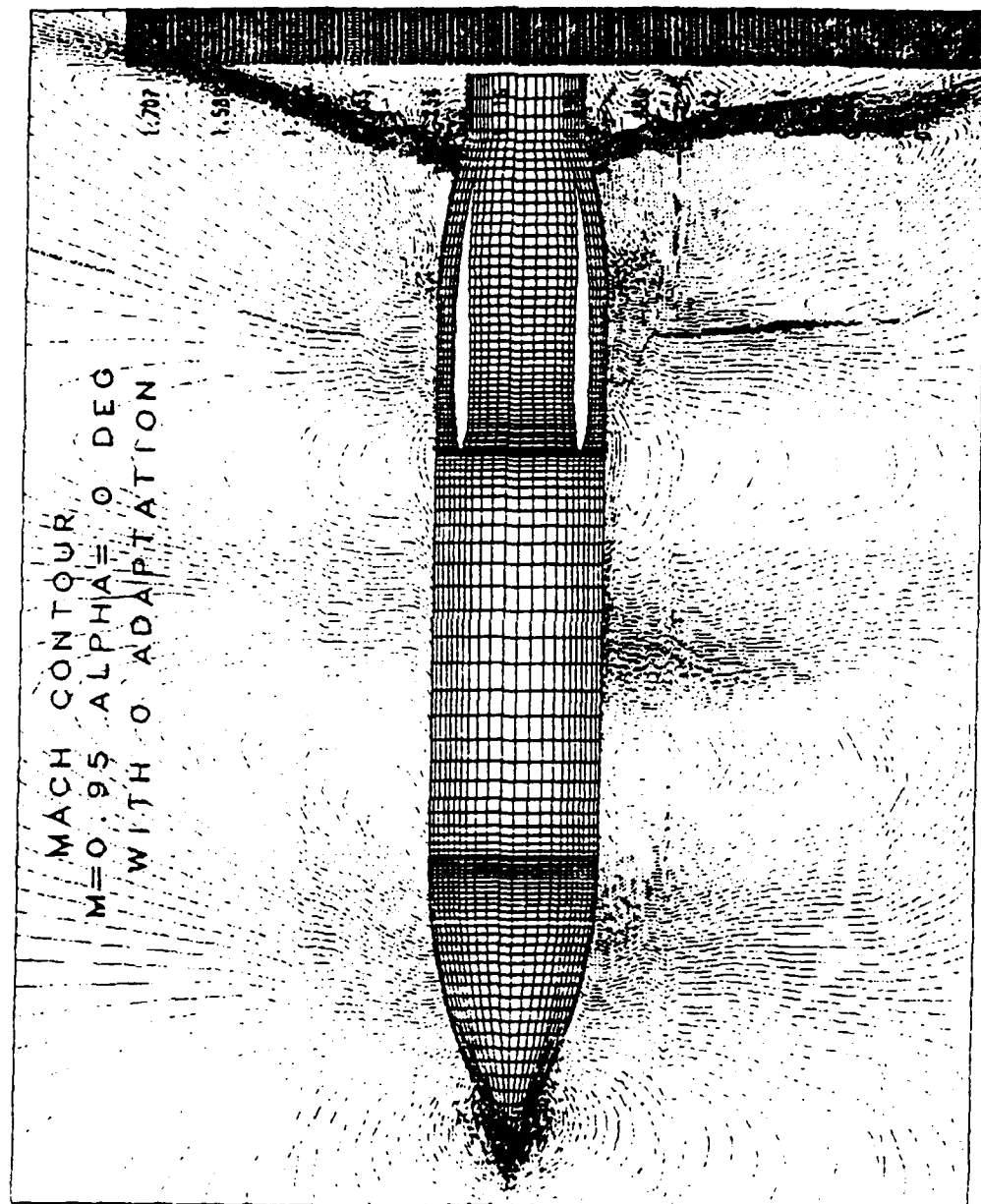


Figure 49. Mach Contours with Initial Grid, Section A-A

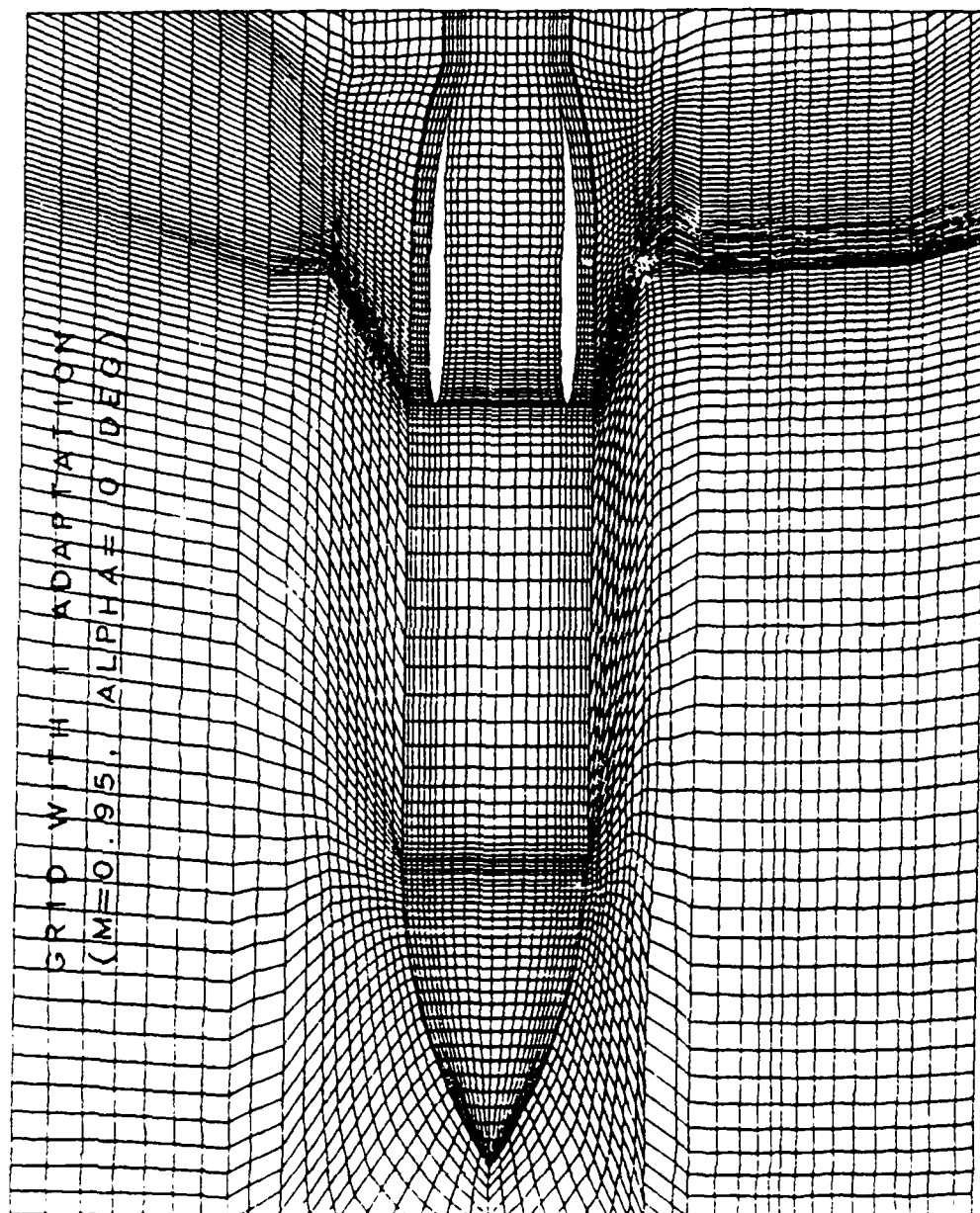


Figure 50. Grid with One Adaptation, Section A-A

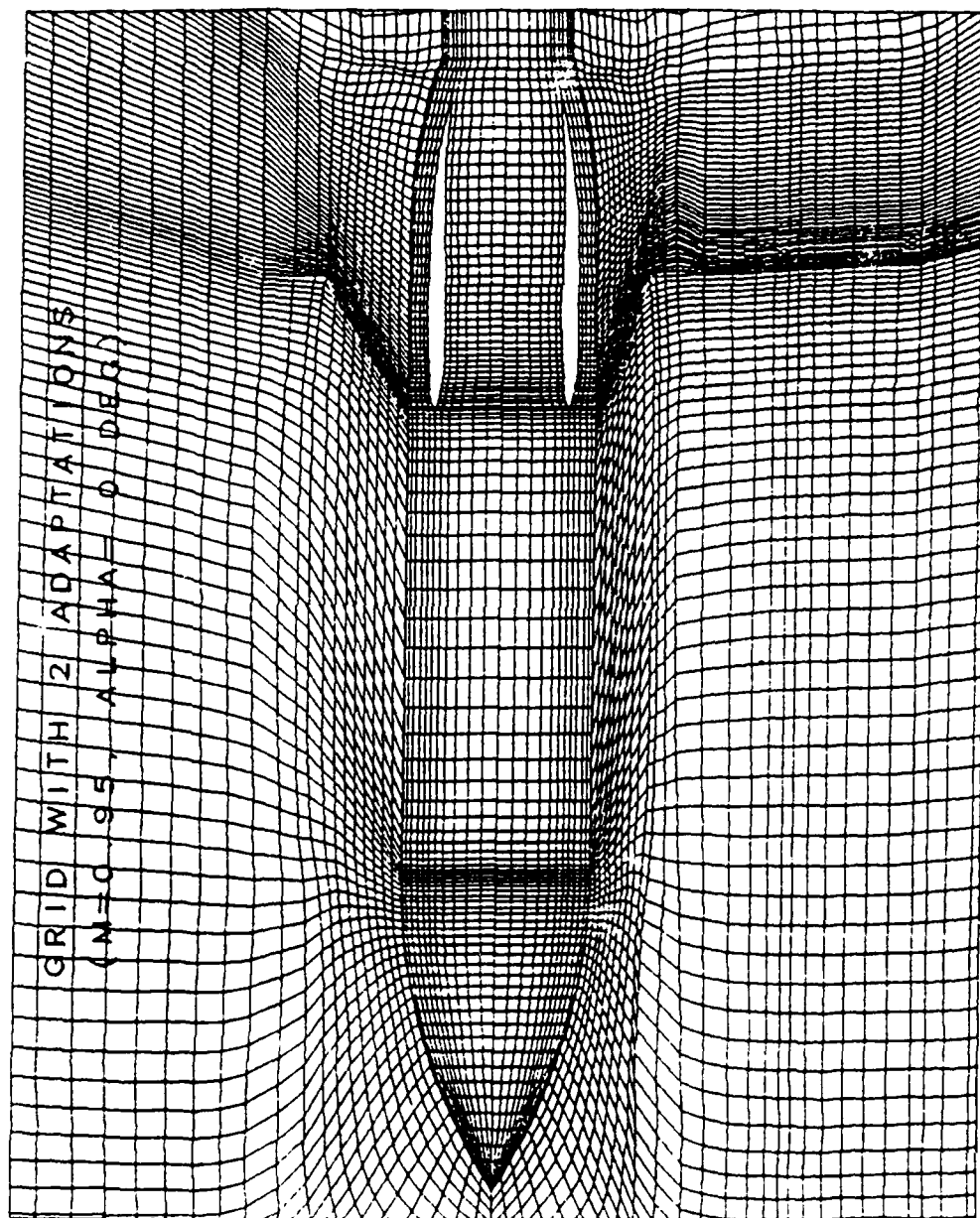


Figure 51. Grid with Two Adaptations, Section A-A

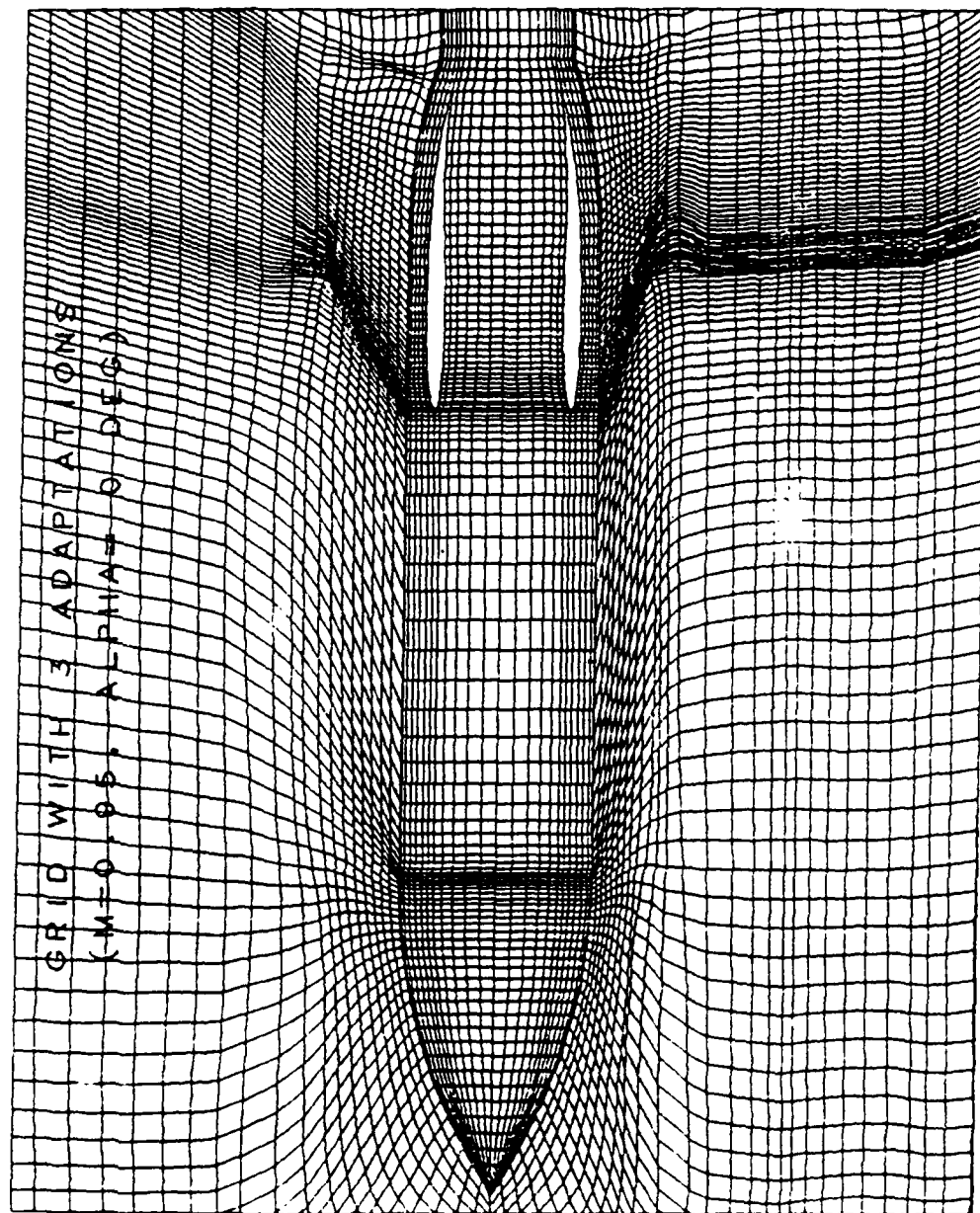
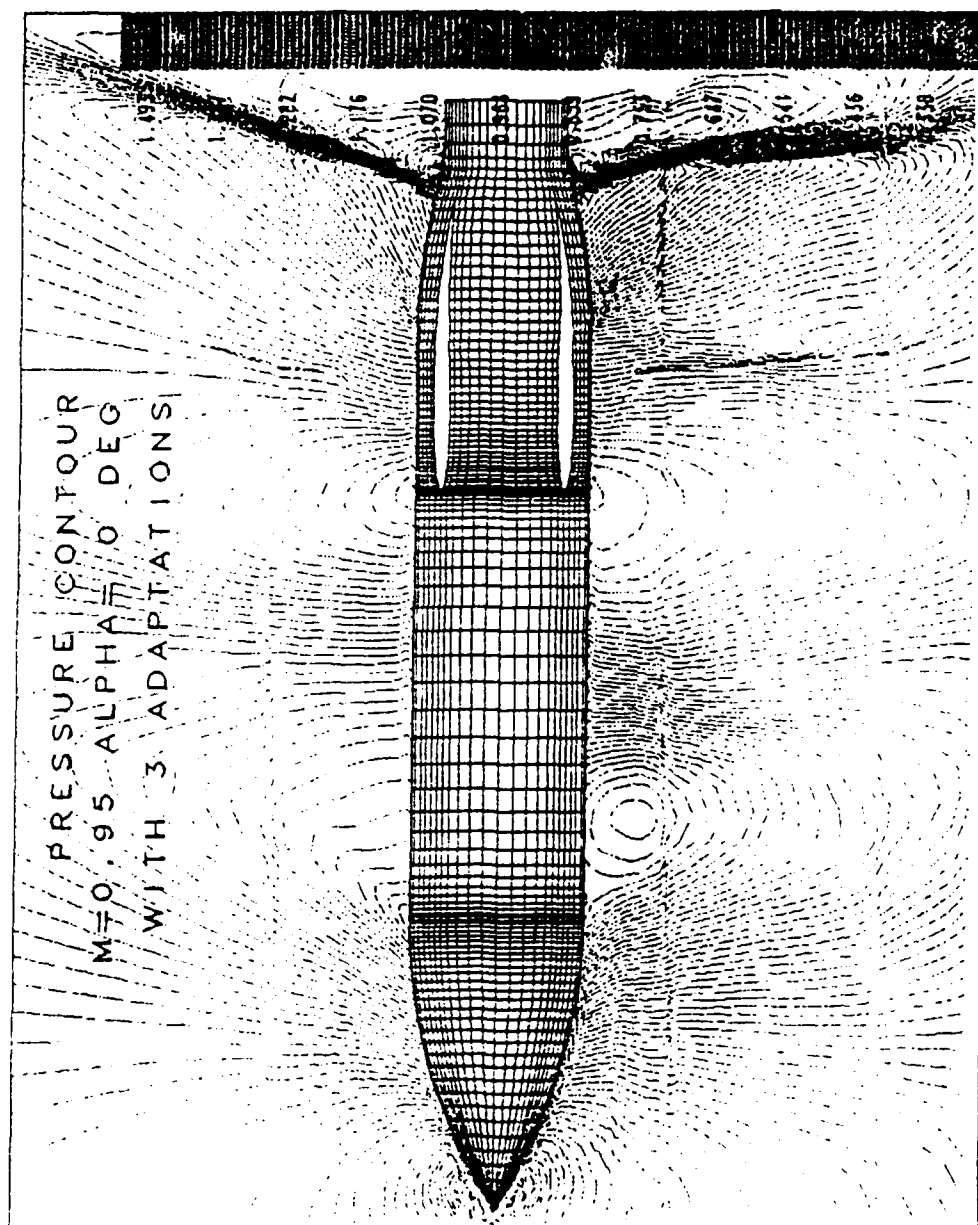


Figure 52. Grid with Three Adaptations, Section A-A



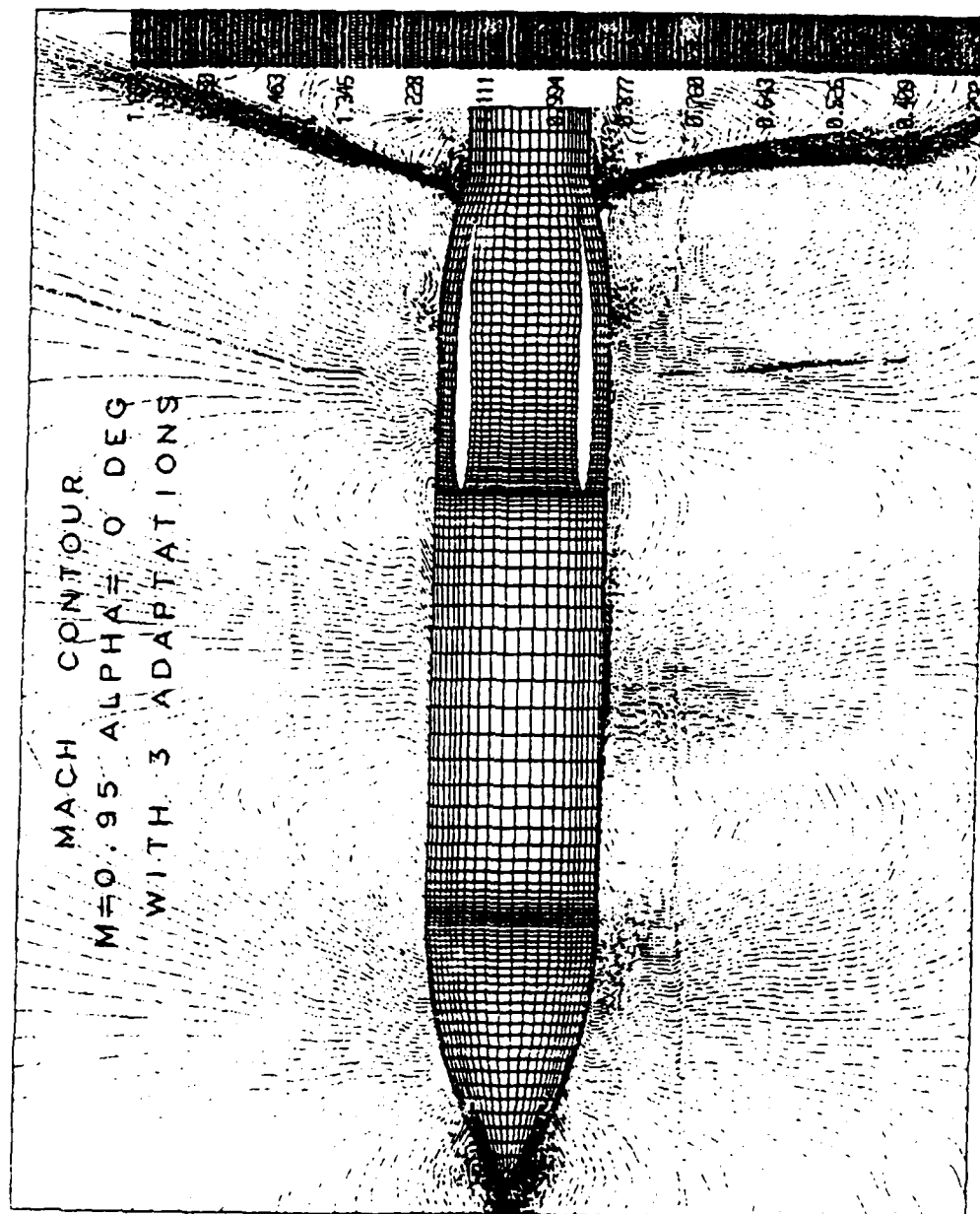


Figure 54. Mach Contours with Three Adaptations, Section A-A

30 BLOCK 3 STORE M=0.95 ALPHA=0 DEG
EULER SOLUTION - ADAPTIVE GRID

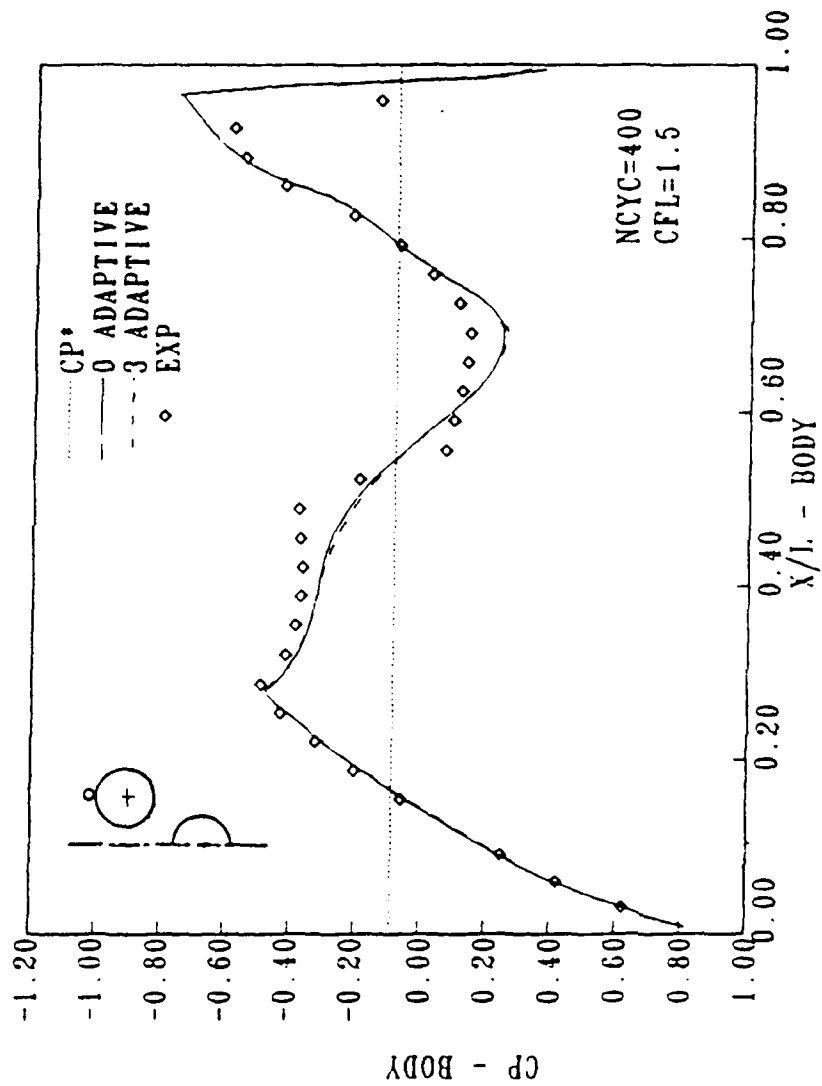


Figure 55. Pressure Distribution Along Store 1, $\Phi = 0$ Deg.

30 BLOCK 3 STORE M=0.95 ALPHA=0 DEG
EULER SOLUTION - ADAPTIVE GRID

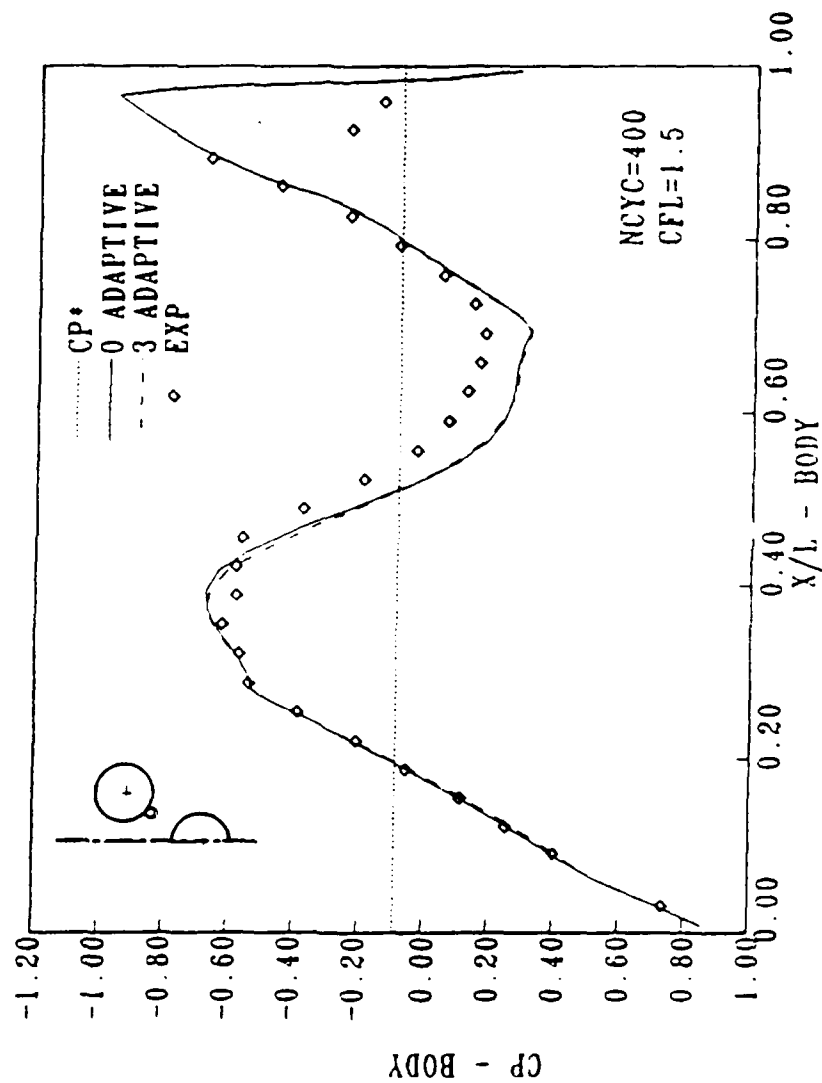


Figure 56. Pressure Distribution Along Store 1, Phi = 220 Deg.

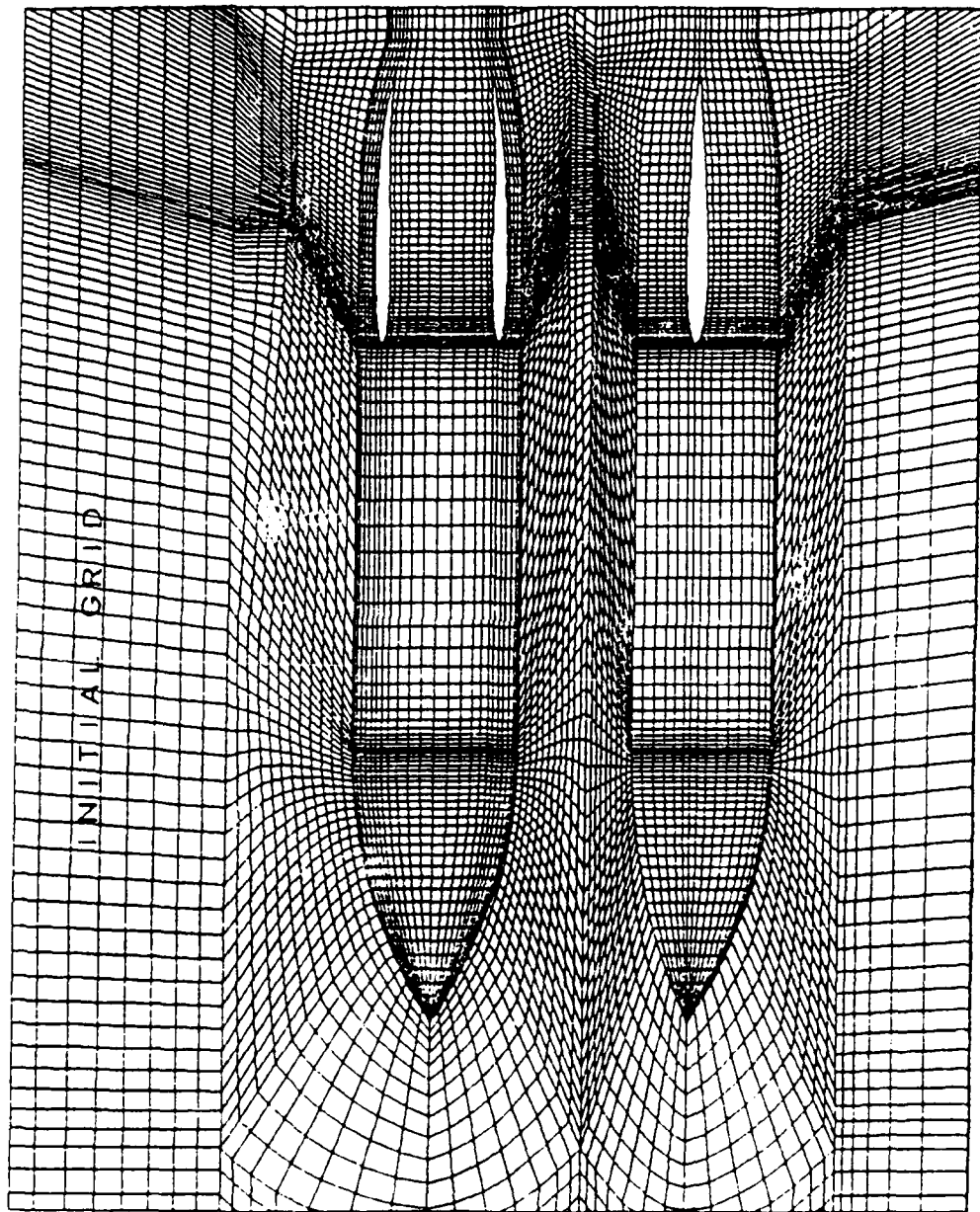


Figure 57. Initial Grid, Section B-B

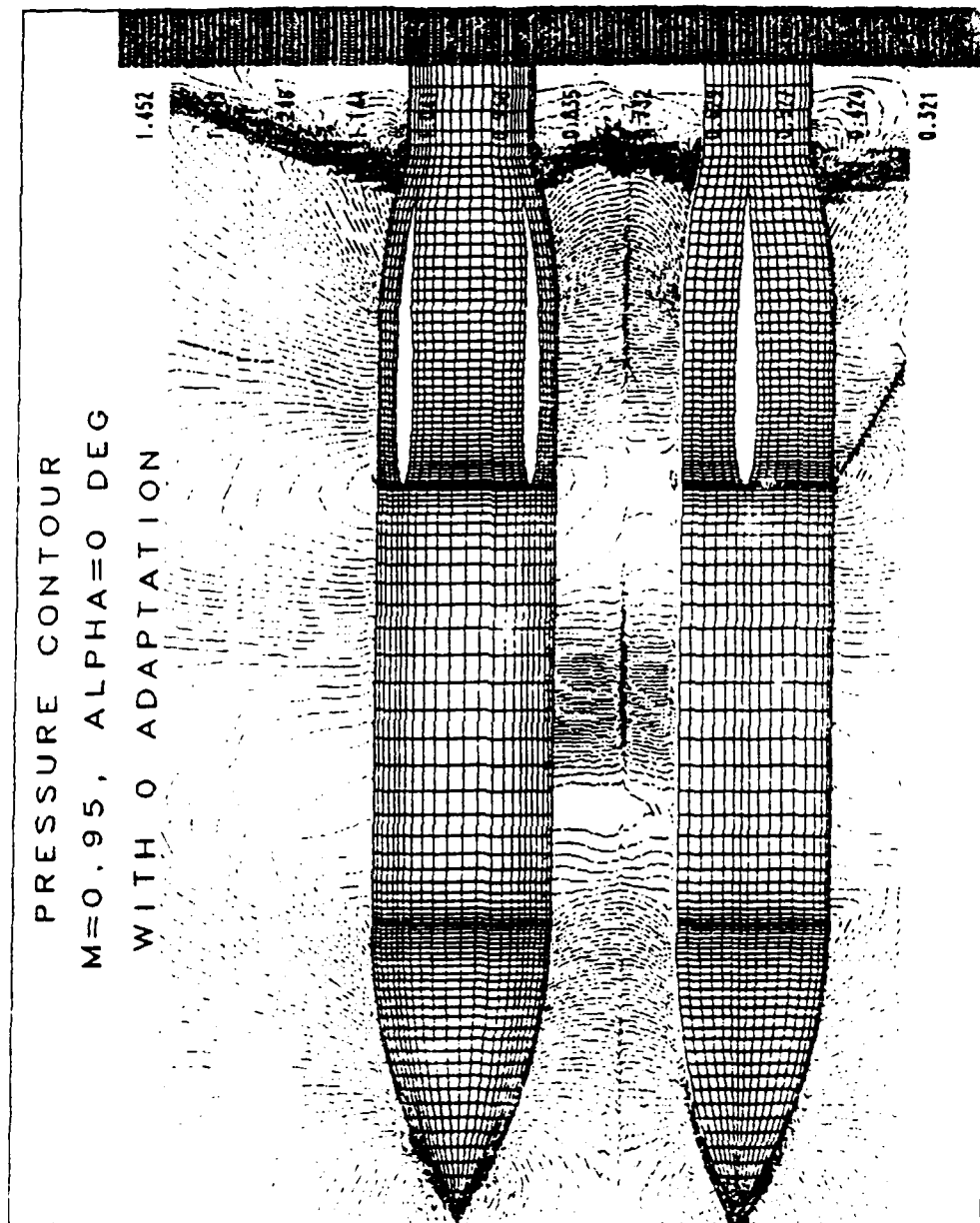


Figure 58. Pressure Contours with Initial Grid, Section B-B

MACH CONTOUR
 $M=0.95$, $\text{ALPHA}=0^\circ$ DEG
 WITH 0 ADAPTATION

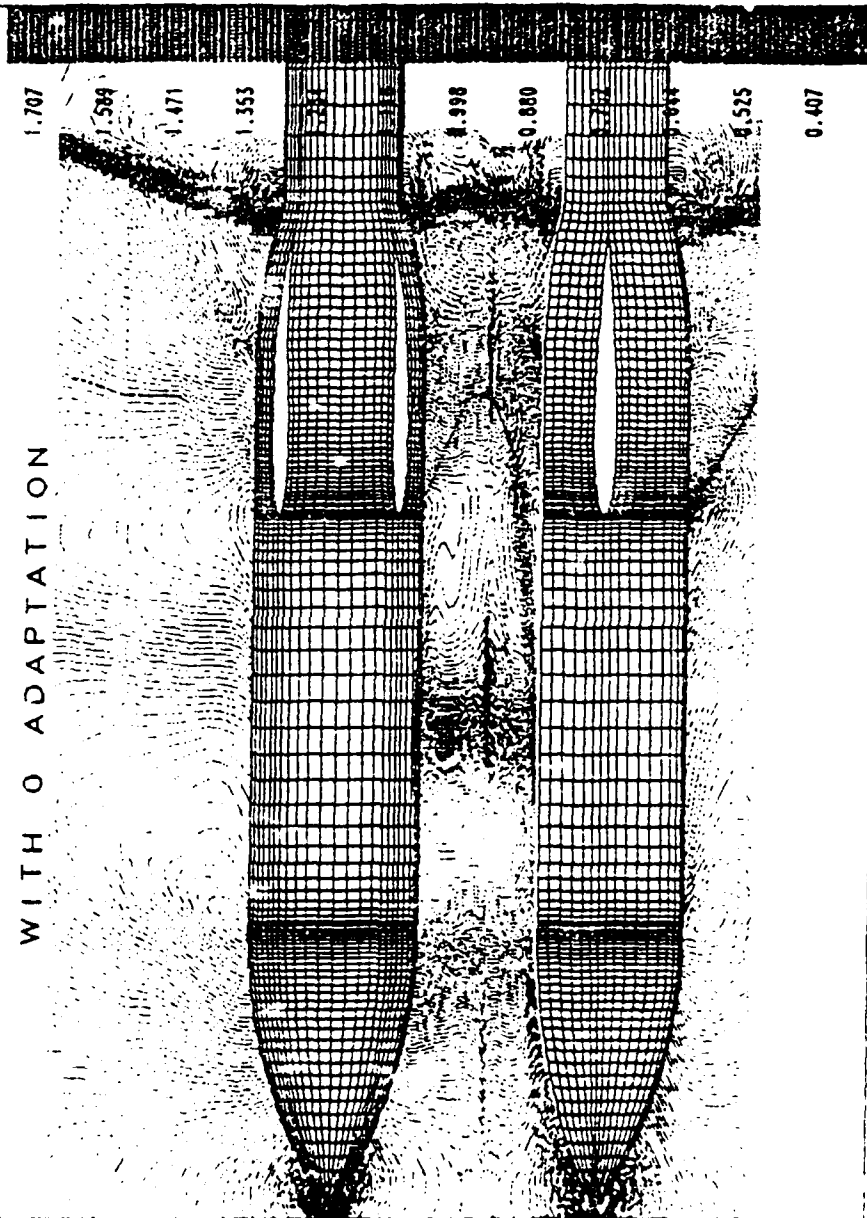


Figure 59. Mach Contours with Initial Grid, Section B-B

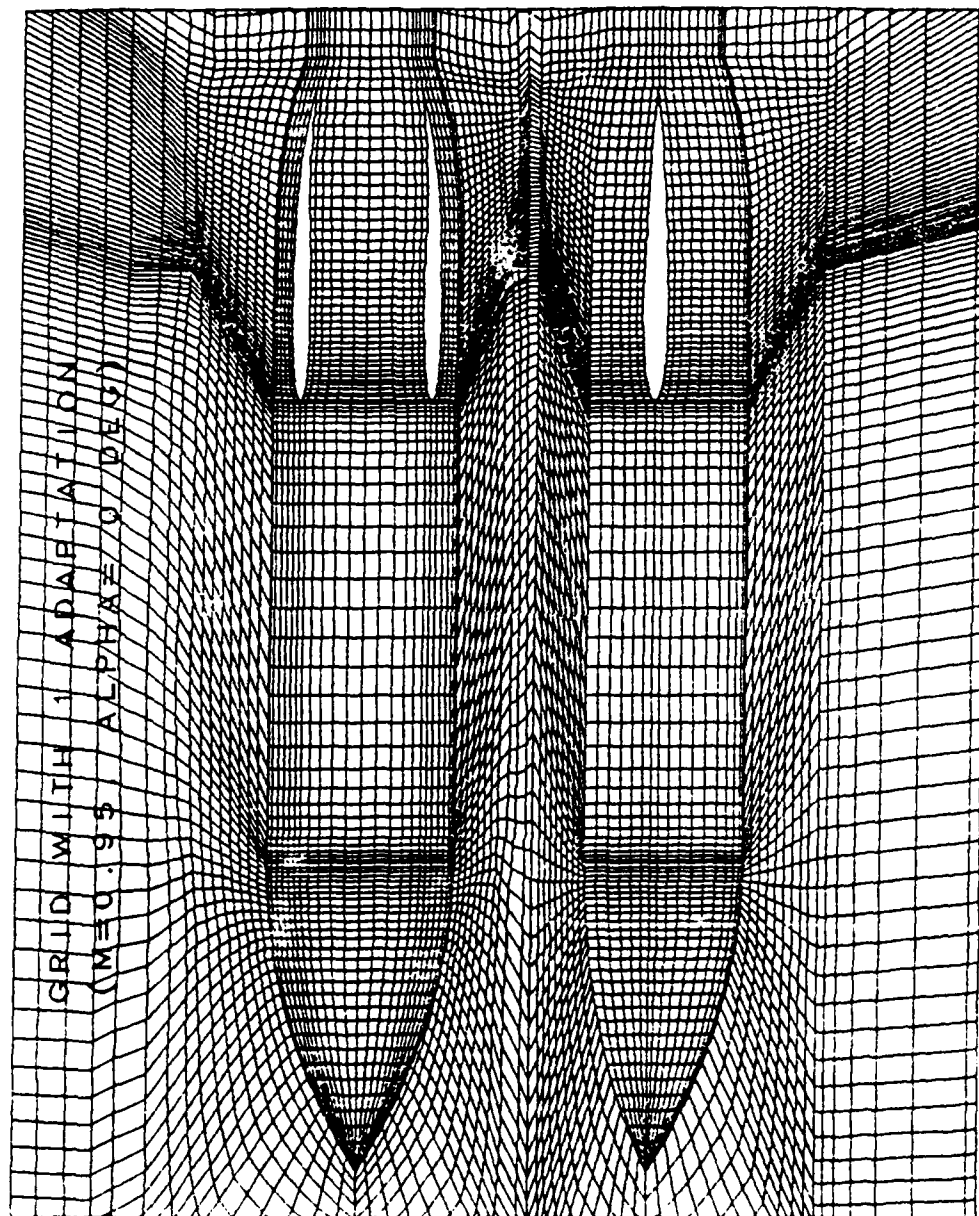


Figure 60. Grid with One Adaptation, Section B-B

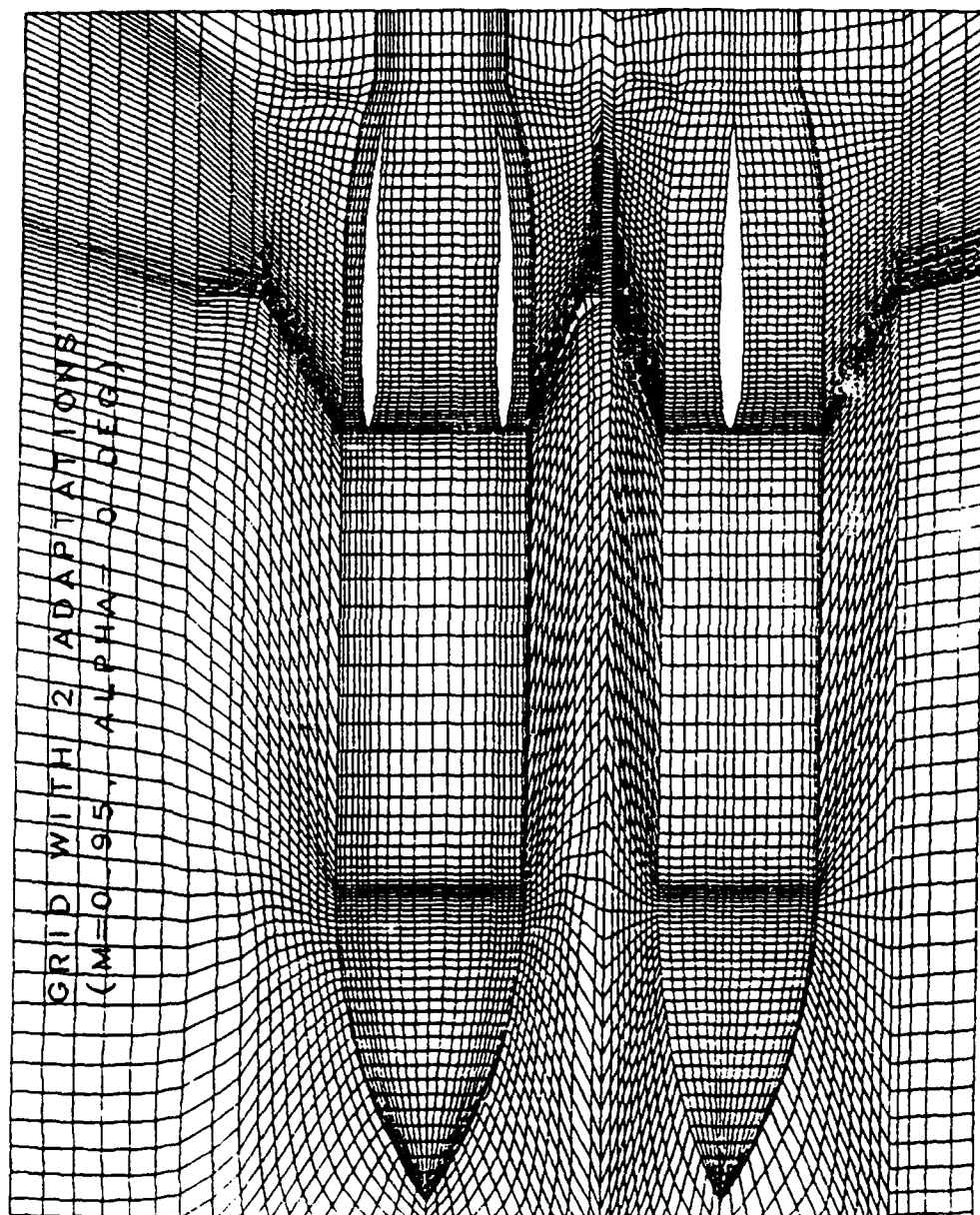


Figure 61. Grid with Two Adaptations, Section B-B

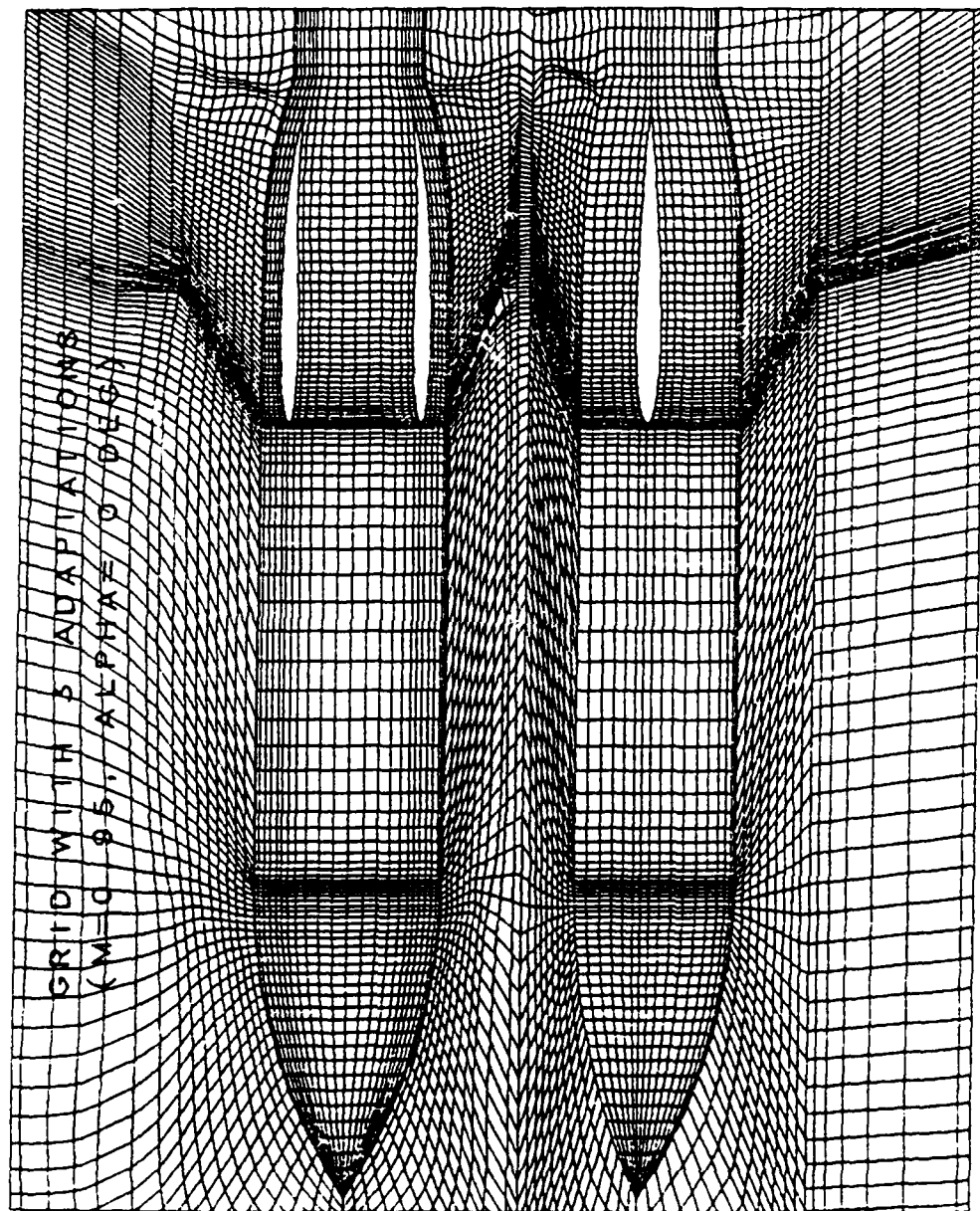


Figure 62. Grid with Three Adaptations, Section B-B

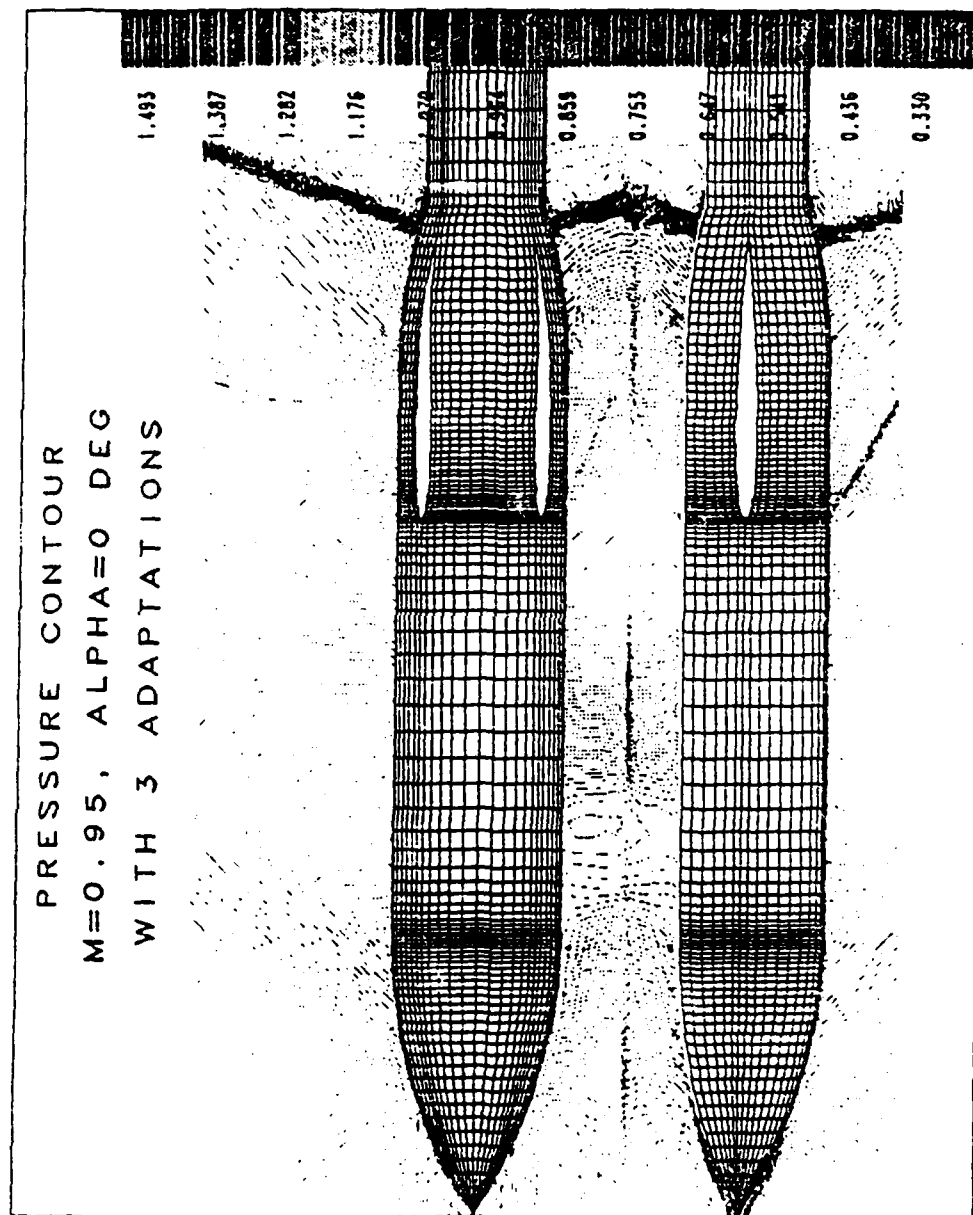


Figure 63. Pressure Contours with Three Adaptations, Section B-B

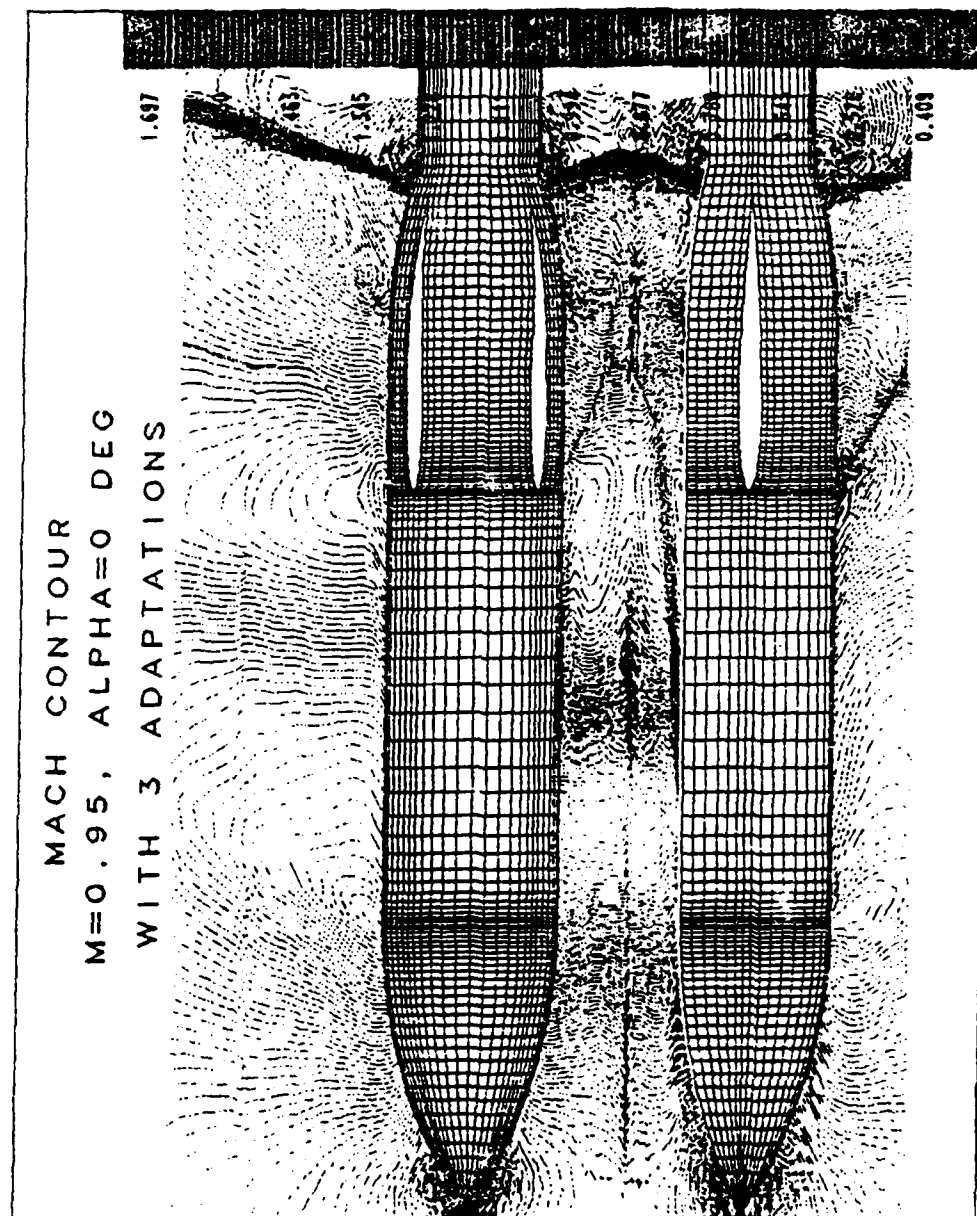


Figure 64. Mach Contours with Three Adaptations, Section B-B

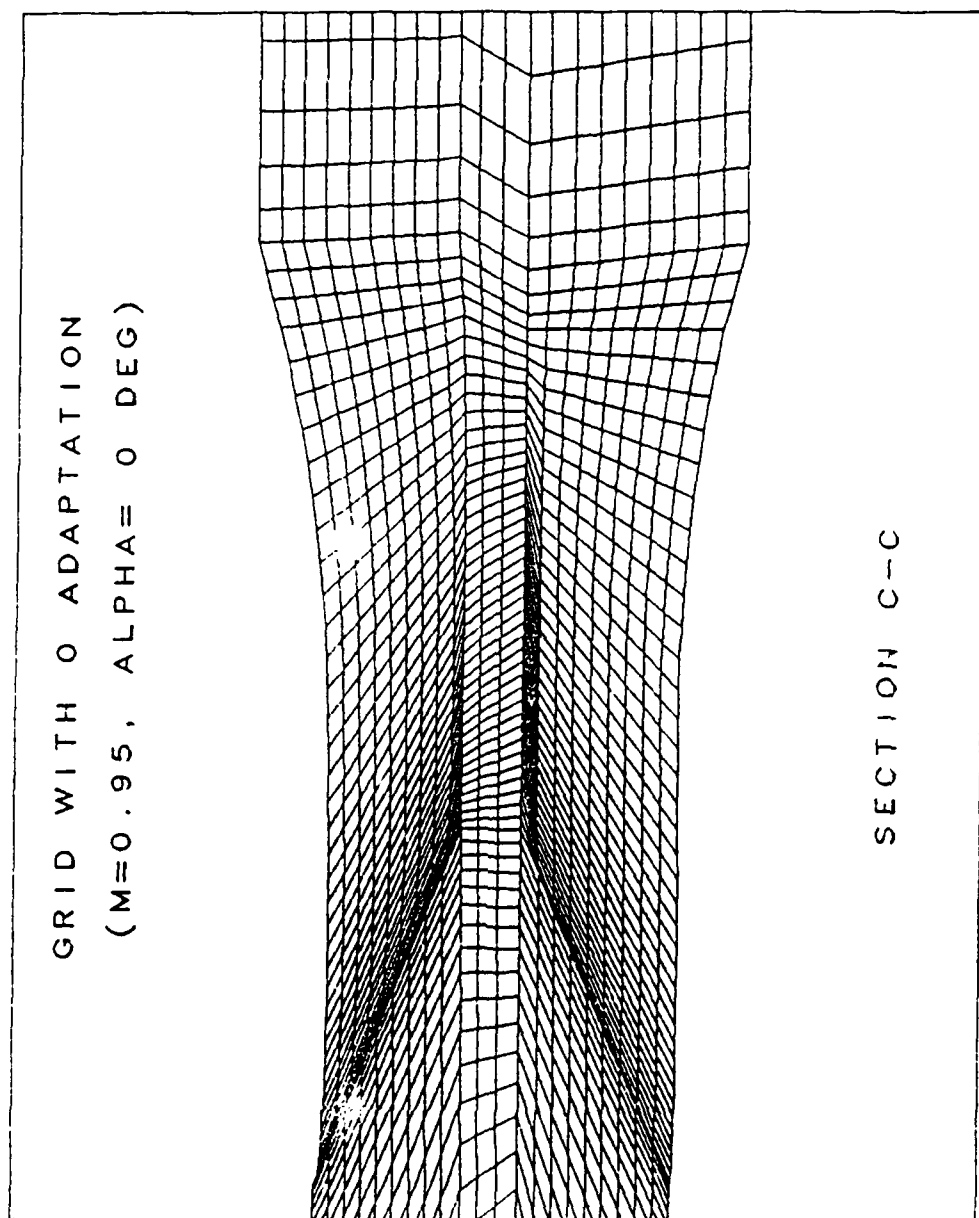


Figure 65. Initial Grid, Section C-C

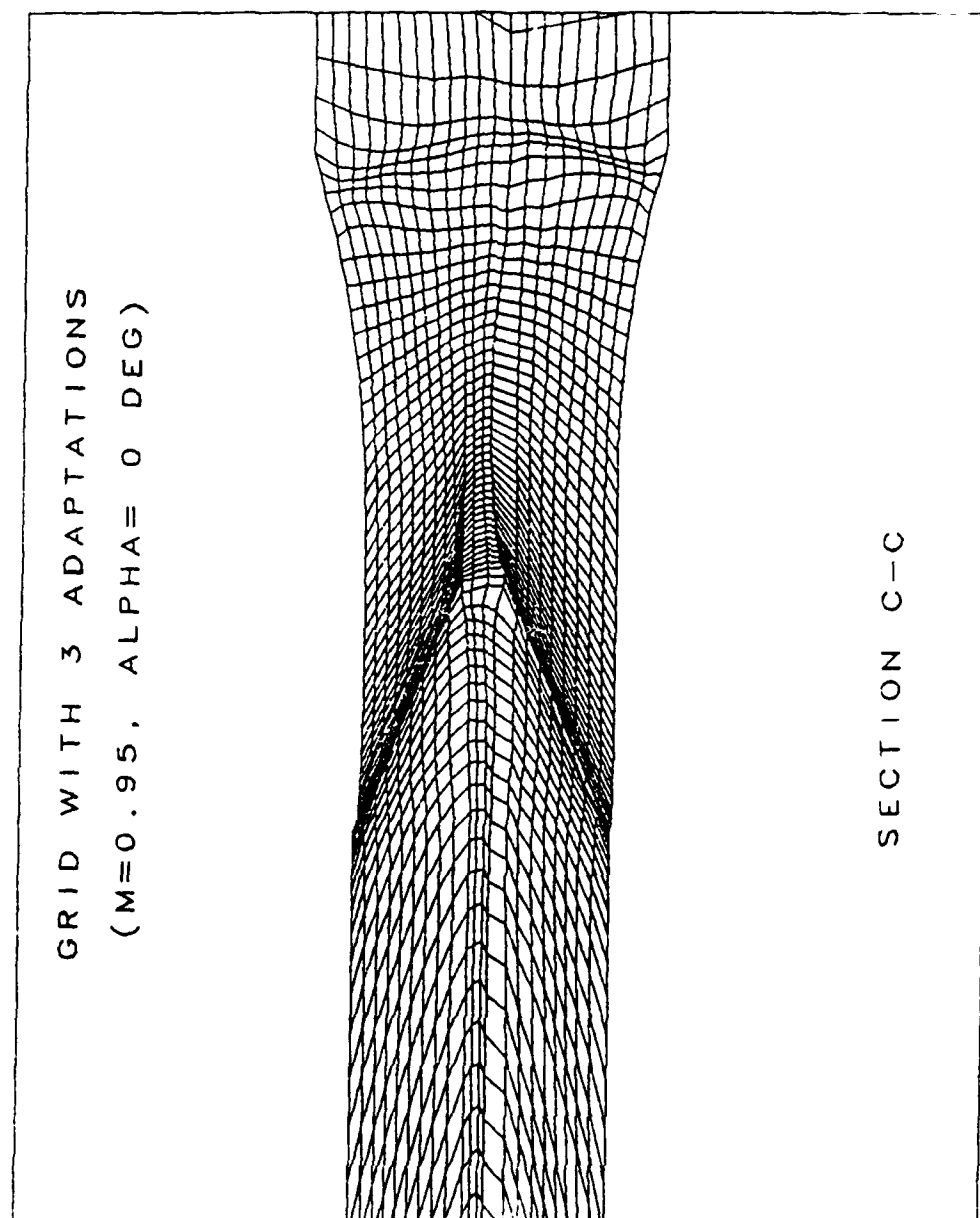


Figure 66. Grid with Three Adaptations, Section C-C

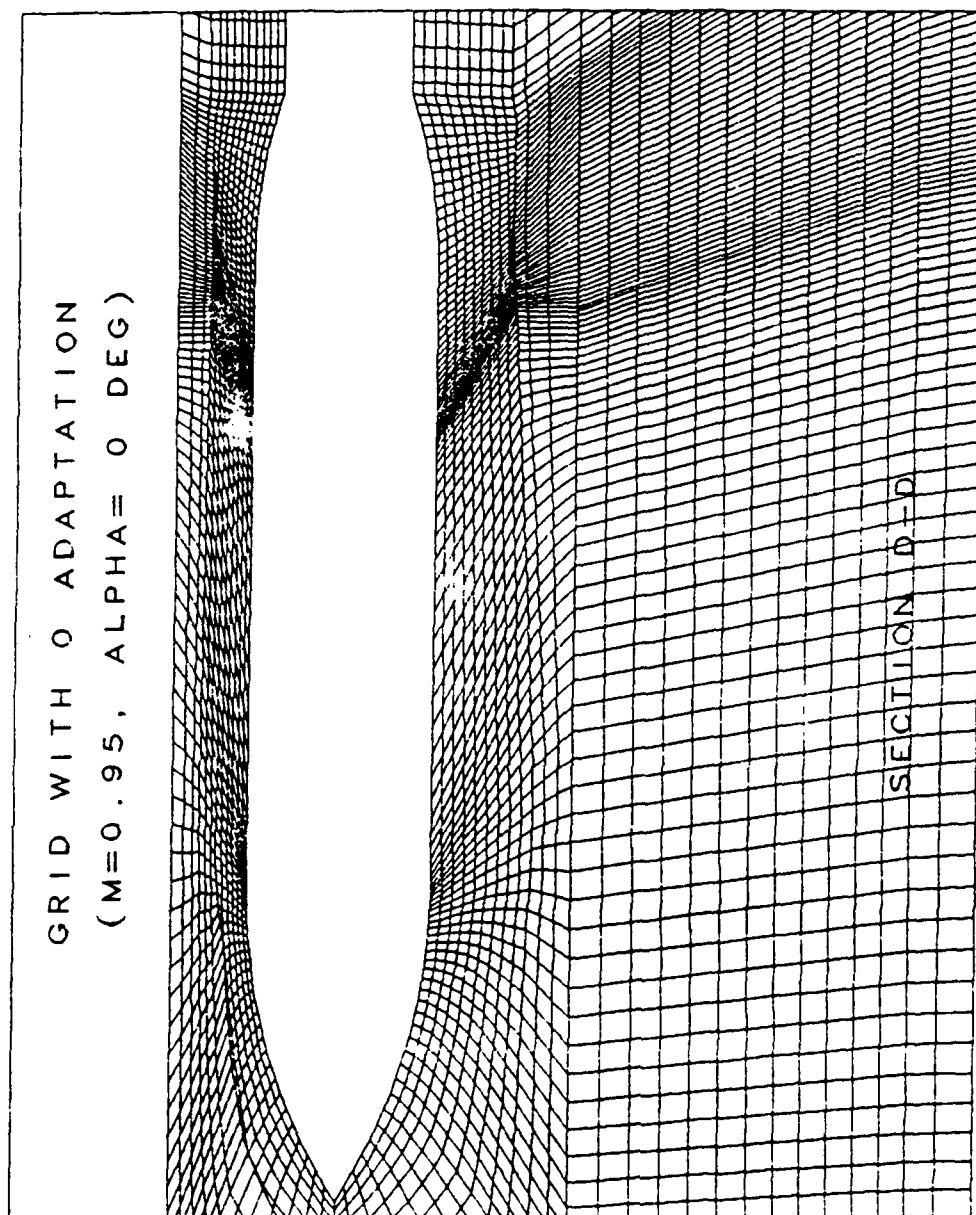


Figure 67. Initial Grid, Section D-D

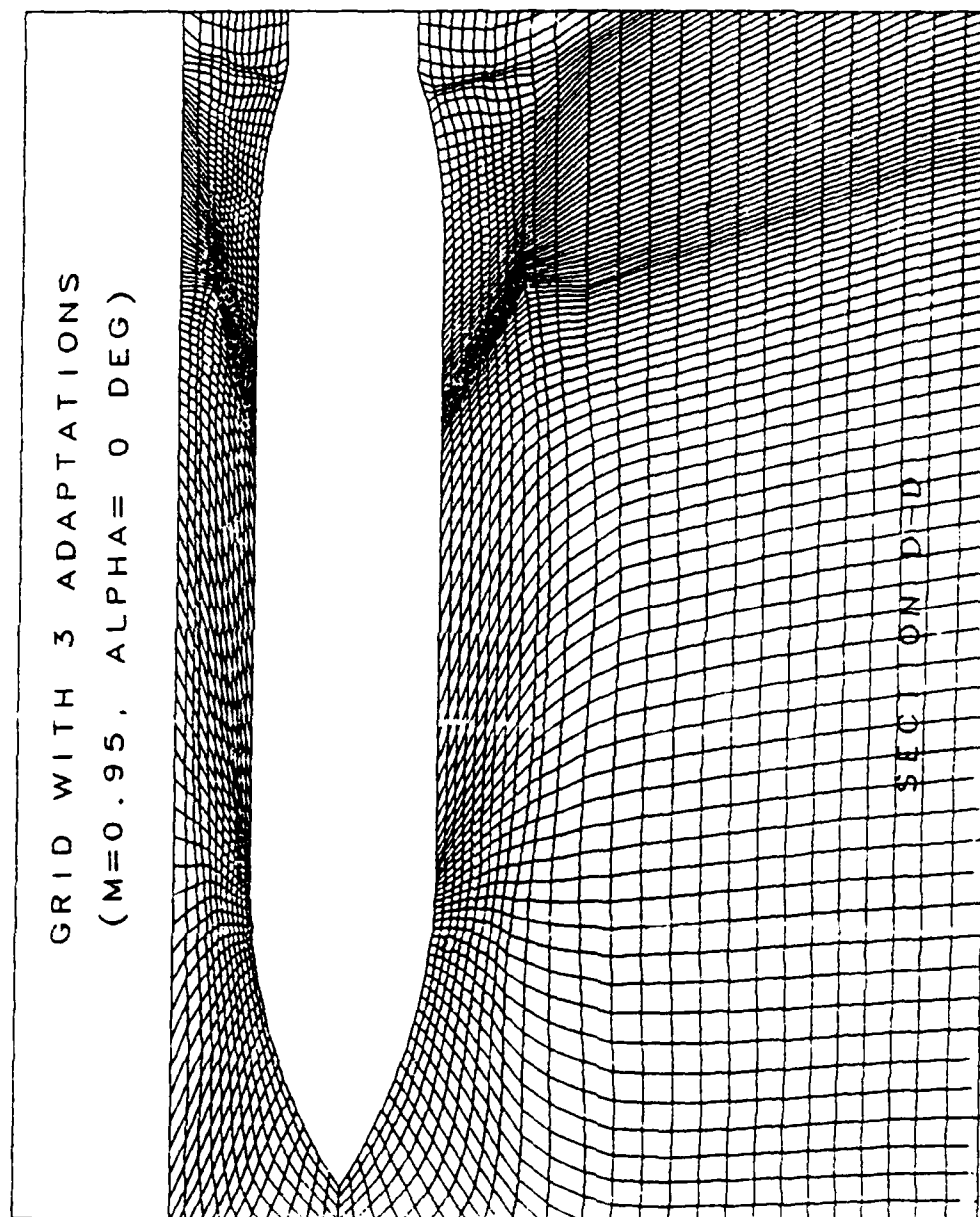


Figure 68. Grid with Three Adaptations, Section D-D

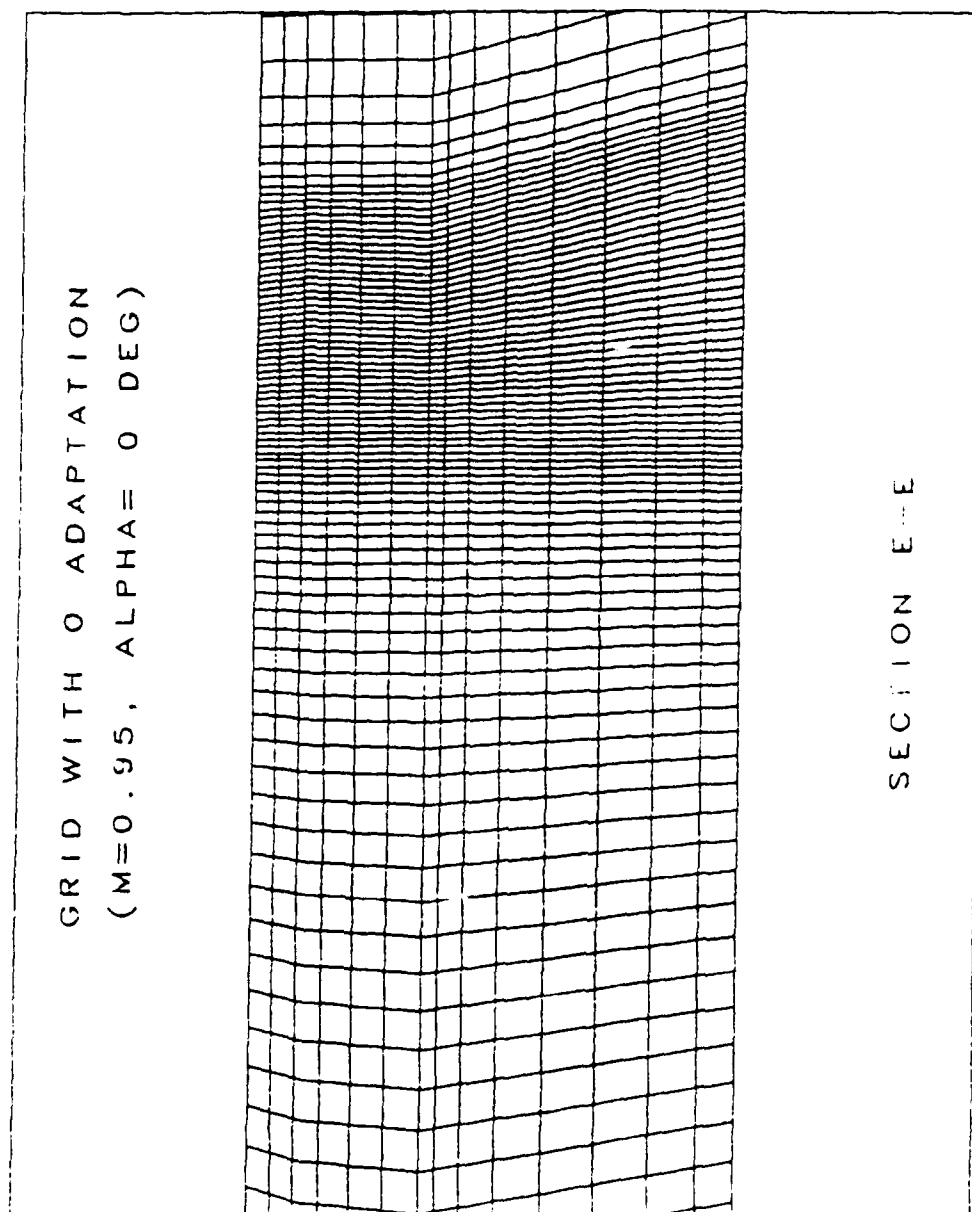


Figure 69. Initial Grid, Section E-E

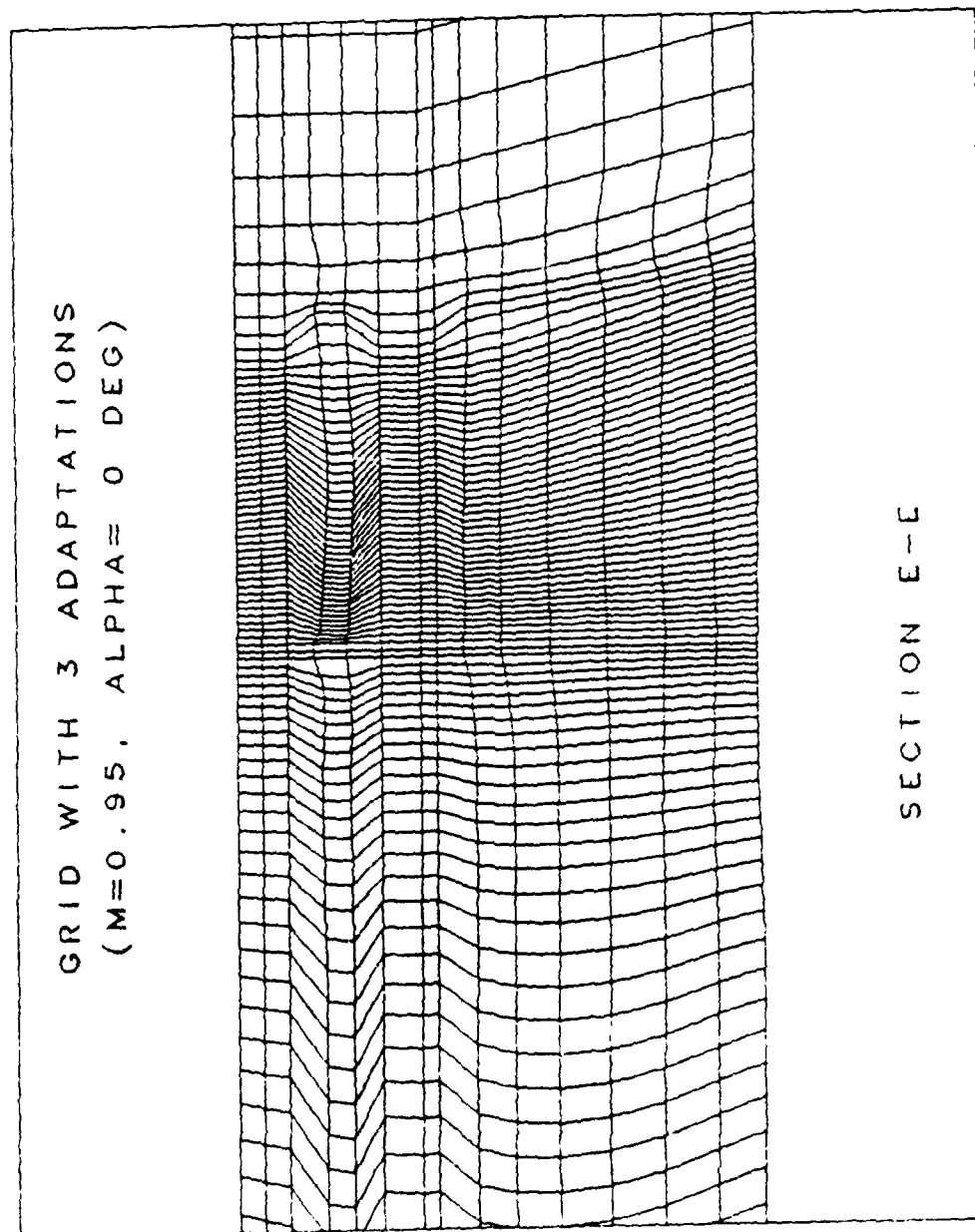


Figure 70. Grid with Three Adaptations, Section E-E

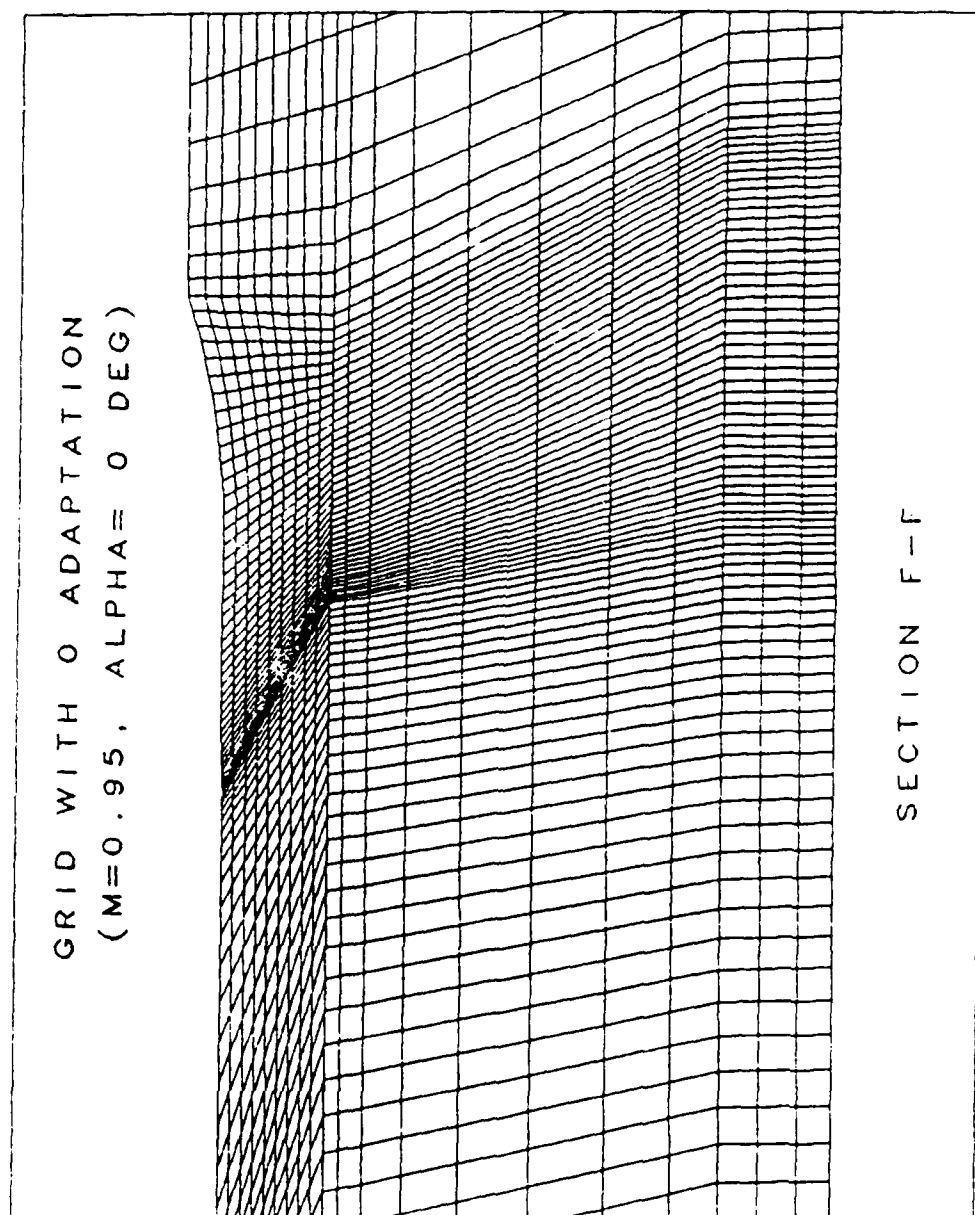


Figure 71. Initial Grid, Section F-F

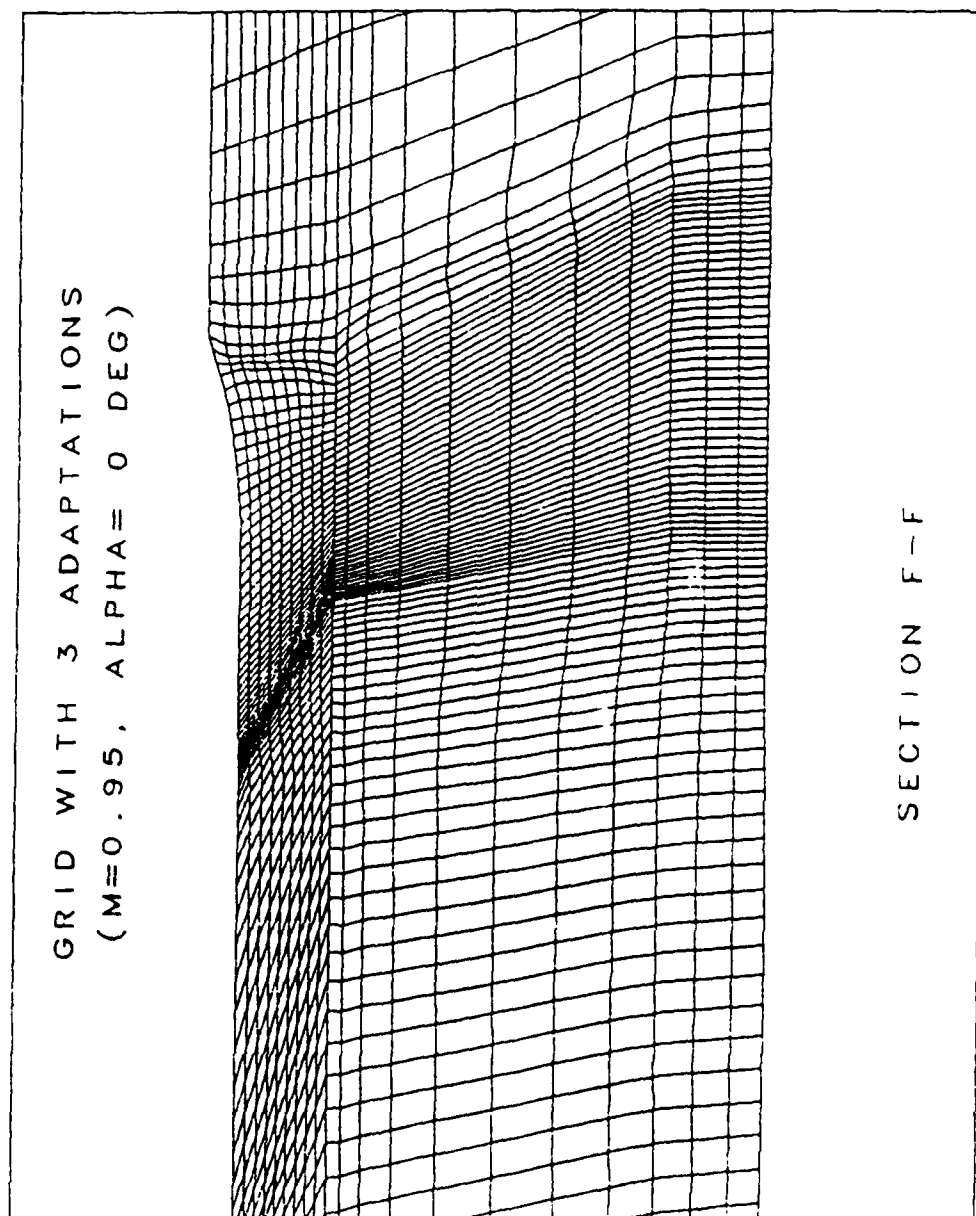


Figure 72. Grid with Three Adaptations, Section F-F

REFERENCES

1. Thompson, J.F., Warsi, Z.U.A., and Mastin, C.W., Numerical Grid Generation: Foundations and Applications, North-Holland, 1985.
2. Thompson, J.F., (Ed.) Numerical Grid Generation, North-Holland, 1982.
3. Belk, D.M. and Whitfield, D.L., "3-D Euler Solution on Blocked Grid Using an Implicit Two-Pass Algorithm", AIAA-87-Blocked Grid Using an Implicit Two-Pass Algorithm", AIAA-87-0450, AIAA 25th Aerospace Sciences Meeting, Reno, 1987.
4. Kim, H.J., "Three Dimensional Adaptive Grid Generation on a Composite Structure", PhD Dissertation, Mississippi State University, 1987.
5. Kim, H.J. and Thompson, J.F., "Three Dimensional Adaptive Grid Generation on a Composite Block Grid", AIAA-88-0311, AIAA 26th Aerospace Sciences Meeting, Reno, 1988.
6. Brackbill, J.U. and Saltzman, J.S., "Adaptive Zoning for Singular Problems in Two Dimensions", Journal of Computational Physics, 46, 342, 1982.
7. Anderson, D.A. and Rai, M.M., "The Use of Solution Adaptive Grids in Solving Partial Differential Equations", Numerical Grid Generation, Ed. J.F. Thompson, North-Holland, 317, 1982.
8. Dwyer, H.A., Kee, R.J., and Sanders, B.R., "An Adaptive Grid Method for Problems in Fluid Mechanics and Heat Transfer", AIAA Paper 79-1464, Williamsburg, Virginia, 1979.
9. Klopfer, G.H. and McRae, D.S., "Nonlinear Analysis of the Truncation Errors in Finite Difference Schemes for the Full System of Euler Equations", AIAA Paper 81-0193, St. Louis, Missouri.
10. Whitfield, D.L., Belk, D.M., and Mounts, J.S., Program EAGLE User's Manual, Vol. 4: Multiblock Implicit, Steady-State Euler Code, USAF Armament Laboratory Technical Report, AFATL-TR-88-117, Eglin AFB, Fl., 1988, Distribution Unlimited.
11. Thompson, J.F., "A Composite Grid Generation Code for General 3-D Regions", AIAA-87-0275, AIAA 25th Aerospace Sciences Meeting, Reno, 1988.
12. Warsi, Z.U.A., Basic Differential Models for Coordinate Generation, Numerical Grid Generation, Ed. J.F. Thompson, North-Holland, 41, 1982.

13. Warsi, Z.U.A., "Tensors and Differential Geometry Applied to Analytic and Numerical Coordinate Generation", MSSU-EIRS-81-1, Mississippi State University, 1981.
14. Mastin, C.W., "Boundary-Fitted Coordinate Systems for Numerical Solution of Partial Differential Equations - A Review", Journal of Computational Physics, Vol. 47, pp. 1-108, 1982.
15. Baldwin, B.S. and Lomax, H., "Thin Layer Approximation and Algebraic Model for Separated Turbulent Flows", AIAA-78-257, Algebraic Model for Separated Turbulent Flows", AIAA-78-257, AIAA 16th Aerospace Science Meeting, Huntsville, Al., 1978.
16. Thompson, J.F. and Gatlin, B., Program EAGLE - User's Manual, Vol. 3: Grid Generation, USAF Armament Laboratory Technical Report, AFATL-TR-88-117, Eglin AFB, Fl., 1988, Distribution Unlimited.
17. Thompson, J.F., "Grid Generation Techniques in Computational Fluid Dynamics", AIAA Journal, Vol. 22, No. 11, Nov. 1984, pp. 1505-1523.
18. Eiseman, P.R., "Adaptive Grid Generation", Computer Methods in Applied Mechanics and Engineering, Vol. 64, 321, 1987.
19. Anderson, D.A., "Equidistribution Schemes, Poisson Generators, and Adaptive Grids", Applied Mathematics and Computation, Vol. 24, 211, 1987.
20. Anderson, D.A., "Generating Adaptive Grids with a Conventional Grid Scheme", AIAA-86-0427, AIAA 24th Aerospace Sciences Meeting, Reno, 1986.
21. Thompson, J.F. and Gatlin, B., Program EAGLE - User's Manual, Vol. 2: Surface Generation Code, USAF Armament Laboratory Technical Report, AFATL-TR-88-117, Eglin AFB, Fl., 1988, Distribution Unlimited.
22. Lijewski, L.E., "Transonic Flow Solutions on a Blunt, Body-Wing-Canard Configuration Using the Euler Equations", AIAA-87-2273, AIAA 5th Applied Aerodynamics Conference, Monterey, CA, 1987.
23. Lijewski, L.E., "Transonic Euler Solution on Mutually Interfering Finned Bodies", AIAA-89-264, AIAA 27th Aerospace Sciences Meeting, Reno, 1989.